Planar Laser Induced Fluorescence Imaging and Analysis with Ethanol Blended Fuels in a Direct Injection Spark Ignition Engine

A thesis submitted for the degree of Doctor of Philosophy

by

Quan Liu

Department of Mechanical, Aerospace and Civil Engineering

College of Engineering, Design and Physical Sciences

Brunel University London

January 2017

Abstract

The currently reported thesis was concerned with visualisation of the charge homogeneity and cyclic variations within the planar fuel field near the spark plug in an optical spark ignition engine fitted with an outwardly opening central direct fuel injector. Specifically, the project examined the effects of fuel type and injection settings, with the overall view to understanding some of the key mechanisms previously identified as leading to particulate formation in such engines. The three fuels studied included a baseline iso-octane, which was directly compared to two gasoline fuels containing 10% (E10) and 85% (E85) volume of ethanol respectively. The engine was a bespoke single cylinder with Bowditch style optical access through a flat piston crown. Charge stratification was studied over a wide spectrum of injection timings using the Planar Laser Induced Fluorescence (PLIF) technique, with additional variation in charge temperature due to injection also estimated when viable using a two-line PLIF approach. Overall, both gasoline-ethanol fuels generally exhibited a higher degree of stratification, albeit at least partly alleviated with elevated rail pressures. Under both warm and cold liner conditions the E10 fuel showed clear evidence of fuel droplets persisting up until ignition. Interestingly, with late injection timing the repeatability of the injection was superior (statistically) with higher ethanol content in the fuel, which may have been associated with the higher charge temperatures aiding control of the evaporation of the main mass of alcohol. The findings were corroborated by undertaking a comprehensive study of the influence of varying fuel type and injection settings on thermodynamic performance and engine-out emissions during firing operation, with additional gas exchange effects also influencing the optimum fuel injection timings.

Acknowledgements

First and foremost, I would like to express my sincere gratitude to my supervisor, Prof Alasdair Cairns, for his unlimited support and invaluable guidance throughout the work, I just could not have asked for a better supervisor. I would also like to thank Prof Hua Zhao for his help when sought.

I would like to thank Mr Hugh Blaxill, Mr Mike Bunce, Mr Luke Cruff (previously) and everyone at MAHLE Powertrain LLC, for their support both financially and technically throughout my PhD study.

Also, I would like to express my deepest thanks to my fellow colleagues Dr Jun Ma, Dr Yan Zhang and Dr Kangwoo Seo for their help during my time at Brunel University.

Thank you everyone at the Brunel Centre for Advanced Powertrain and Fuels Research (CAPF). Special thanks to Mr Andrew Selway, Mr Kenneth Anistiss and Mr Clive Barratt for their guidance and support throughout the laboratory work.

Last but not least, I would like to thank my parents and my girlfriend Ko-Hsuan Chen for their unconditional support over the past few years.

Finally, the financial support of both MAHLE Powertrain LLC and Brunel University is gratefully acknowledged.

Publications

The following paper was orally presented at SAE 2014 World Congress & Exhibition. It was selected into one of the SAE International Journals with exceptional scores across all criteria, averaging 9 out of 10 from three different reviewers.

Liu, Q., Cairns, A., Zhao, H., Anbari Attar, M. et al., "The Effects of Charge Homogeneity and Repeatability on Particulates Using the PLIF Technique in an Optical DISI Engine," *SAE Int. J. Engines* 7(1):500-518, 2014, doi:10.4271/2014-01-1207.

Table of Contents

List of Figures

List of Tables

Abbreviations and Acronyms

ABF   Absolute Fluorescence Method

ASOI   after Start of Injection

aTDC   after Top Dead Centre

avg   average

BMEP   Brake Mean Effective Pressure

BSFC   Brake Specific Fuel Consumption

bTDC   before Top Dead Centre

c.a.   crank angle

CAI   Controlled Auto Ignition

CARB   California Air Resources Board

CFD   Computational Fluid Dynamics

CO2   Carbon Dioxide

COV   Coefficient of Variation

CVC   Constant Volume Chamber

DI   Direct Injection

DIF   Double Image Frames

DISI   Direct Injection Spark Ignition

DPF   Diesel Particulate Filter

E10   10% Ethanol in 95RON Gasoline

E20   20% Ethanol in 95RON Gasoline

E85   85% Ethanol in 95RON Gasoline

EMOP   Exhaust Maximum Opening Point

FSI	Fuel Stratified Injection
FSN	Filter Smoke Number
GPF	Gasoline Particulate Filter
HCCI	Homogeneous Charge Compression Ignition
HR	Highly Reflective
HT	Highly Transmitted
ICCD	Intensified Charged-Coupled Device
IMEPg	gross Indicated Mean Effective Pressure
IMEPn	net Indicated Mean Effective Pressure
IMOP	Inlet Maximum Opening Point
incr.	increments
IVC	Intake Valve Closure
KrF	Krypton Fluoride
LEV	Low Emission Vehicle
LHV	Lower Heating Value
LNV	Least Nominal Value
LSPI	Low Speed Pre-Ignition
MBT	Maximum Brake Torque
MON	Motor Octane Number
MY2009	Model Year 2009
NVO	Negative Valve Overlap
OEM	Original Equipment Manufacturer
PDA	Phase Doppler Anemometry
PFI	Port Fuel Injection

PLIF	Planar Laser Induced Fluorescence
PM	Particulate Matter
PMEP	Pumping Mean Effective Pressure
PN	Particulate Number
PTFE	Polytetrafluoroethylene
PTG	Programmable Timing Generator
ROI	Region of Interest
RON	Research Octane Number
SI	Spark Ignition
SIF	Single Image Frames
SOI	Start of Injection
TEA	Triethylamime
THAF	Thermally Assisted Fluorescence
THC	Total Hydrocarbons
TS	Thermal Stratification
uHC	Unburned Hydrocarbon
ULG	Unleaded Gasoline
VOC	Volatile Organic Compounds
WOT	Wide Open Throttle
XeCl	Xenon Chloride
λ	relative air-to-fuel ratio

Chapter 1 Introduction

1.1 Background

The two main factors of evolving emissions legislation and concerns for diminishing fuel reserves continue to prompt the automotive sector to seek alternative modes of engine operation. Solutions currently being considered include hybrid and full electric vehicles [1], but at present these remain insufficiently technically advanced to be considered as a dominant mode of propulsion. It is therefore widely acknowledged that the internal combustion will remain key for decades to come, albeit operating in refined form and in some cases as part of a hybrid powertrain. In recent years European CO_2 emissions targets have been progressively tightened to $130gCO_2$/km for all new passenger cars registered from 2015 onwards, with manufacturers expected to meet $95gCO_2$/km by 2020 [2]. To date, such targets have mainly been met through increased diesel sales. However, the distillation of crude oil results in high proportions of both gasoline and diesel fuel [1] and ultimately this has resulted in Europe becoming "diesel lean" at times [3]. In addition, the full impact of the recent "diesel gate" emissions scandal remains uncertain. The current status of the European fleet indicates that significant work is still required in the field of gasoline Spark Ignition (SI) engines and recently proposed legislation in California indicates that the US market will enter a period of aggressive CO_2 emission reduction. Over the past few years, there has been a rapid growth in China's vehicle market and currently being the largest in the world, therefore severe energy and environmental issues begin to emerge. Large amounts of CO_2 emissions have been generated in China, and it has long been the largest CO_2 emitter in the world. In order to take responsibility for the global warming issue, the Chinese government has put forward plans for an even more aggressive CO_2 emission reduction in its road transport sector and promised to reach the peak of national total carbon emission before 2030 [4]. Overall, in order to meet future global CO_2 emissions goals, in the short term it will be necessary to improve the fuel consumption of the gasoline engine and in the longer term source sustainable alternatives to crude oil.

In recent years various technologies have emerged to improve the fuel economy of the SI engine, with considerable interest in methods such as direct fuel injection (including homogeneous and stratified variants [5], [6], [7]), variable valvetrain systems (variable valve timing, duration and lift [8], [9], [10], [11]), friction/parasitic reduction technologies [12], [13], advanced downsizing and boosting techniques [14], [15], [16] and alternative low temperature combustion modes including Controlled Auto-Ignition (CAI) [17], [18], [19].

Over the last decade or so the downsizing technique has been implemented as a highly promising short-to-medium term solution [7], [14], [15], [16], [20], [21], with moderately downsized production solutions emerging [22], [23], [24]. The strong synergy between downsizing and Direct Injection Spark Ignition (DISI) is now reasonably well understood, with charge cooling, volumetric and thermal efficiency gains already well quantified [7], [14], [20], [21], [22], [23], [24], [25], [26], [27]. Nevertheless, DISI engines may produce increased particulate emissions compared to fully optimised Port Fuel Injection (PFI) counterparts. Such particulate emissions from diesel and gasoline engines contribute to atmospheric pollution and have been shown to be hazardous to human health [28]. Particulate matter number concentration and morphology could be more relevant toxicological metrics than the total PM mass, which is especially relevant for DISI engines which have been reported to be a bigger contributor to ultrafine and nano-sized particulate emissions [29], [30], [31]. For these reasons, Europe has recently finalised the regulation for its PM emissions on DISI engines, with not just PM mass but also PN (6.0×10^{11} #/km) restricted, to be effective from September 2017 (Euro 6C). Similar proposals were also included by the California Air Resources Board (CARB) for the upcoming LEV III, although the PN emissions have not yet been addressed, but the intention of PN to be regulated in the future is firm [32], [33].

As the expected shortage of crude oil supply will sooner or later become a limiting factor, sourcing alternative renewable energy is another problem facing the automotive industry. Alcohol based fuels are probably the best candidate among biofuels to replace fossil fuels, especially if they can be blended within the existing gasoline pool for widespread displacement [34]. Ethanol and gasoline blends have been widely adopted as first generation biofuels, while ethanol can be produced from renewable sources as well as having advantages in source to wheel CO_2 emissions [35]. Nonetheless, issues of practicality remain

on current wheat ethanol as feedstock is limited globally, hence in the long term cellulose ethanol may take over [36] albeit significant challenges remain before this can be considered as viable on a grand scale [37].

1.2 Scope

The scope of the currently reported thesis has been generally focused upon improving understanding of the prior identified fundamental mechanisms leading to particulate emission formation in future homogeneous DISI engines. The ultimate goal of the research is to help in allowing future stringent emissions legislation to be met using a standard three-way catalyst after-treatment system. Albeit the general consensus is that OEMs could tackle the particulate number limit for Euro 6C (effective from September 2017) with in-cylinder methods alone, the application of Gasoline Particulate Filter (GPF) regenerating strategy in the future is firm. The work involves optical study of particulate formation and control, where a bespoke single-cylinder DISI engine with optical access was used to investigate the effects of different fuels on in-cylinder fuel distribution and temperature via the Planar Laser Induced Fluorescence (PLIF) technique, capable of providing valuable information on the tendency for in-cylinder particulate formation due to stratification of the fuel and/or (to a lesser degree) differences in charge temperature.

1.3 Outline of Thesis

In Chapter 2, a review of literature is presented which covers basic SI engine operation, current SI engine technologies, particulate formation in DISI engines along with current and projected emissions legislations and alternative fuels. Set out in Chapter 3 is a description of the experimental test facilities employed to undertake this research work, which included the engine test bed, bespoke single-cylinder engine and its fuels, laser equipment and the data acquisition system. Provided in Chapter 4 are the details of the data analysis and techniques, starting with a review of the state-of-the-art methodologies of in-cylinder fuel distribution and temperature measurements. Shown in Chapter 5 are details of the experimental results and analysis performed throughout the work. Finally, the conclusions and recommendations for future work are set out in Chapter 6.

Chapter 2 Literature Review

2.1 SI Engine Operation

The efficiency of a SI engine is often characterised by the Brake Specific Fuel Consumption (BSFC) contours over its full load and speed range (a so-called BSFC map). Figure 2-1 below shows such an engine fuel consumption map for a typical 2.0 litre naturally aspirated four-cylinder SI engine. The uppermost curve labelled in red illustrates the Wide Open Throttle (WOT) performance throughout its speed range, and also represents its full-load characteristics of being a naturally aspirated engine. This full-load curve is closely related to the volumetric efficiency which is governed by engine port, valvetrain, in-cylinder geometry and gas path design. The performance data points below this curve demonstrate its operating behaviours under part-load conditions. It can be derived that this engine has its minimum BSFC island near to the centre of the map where in the region of mid-speed and under part-load [38].
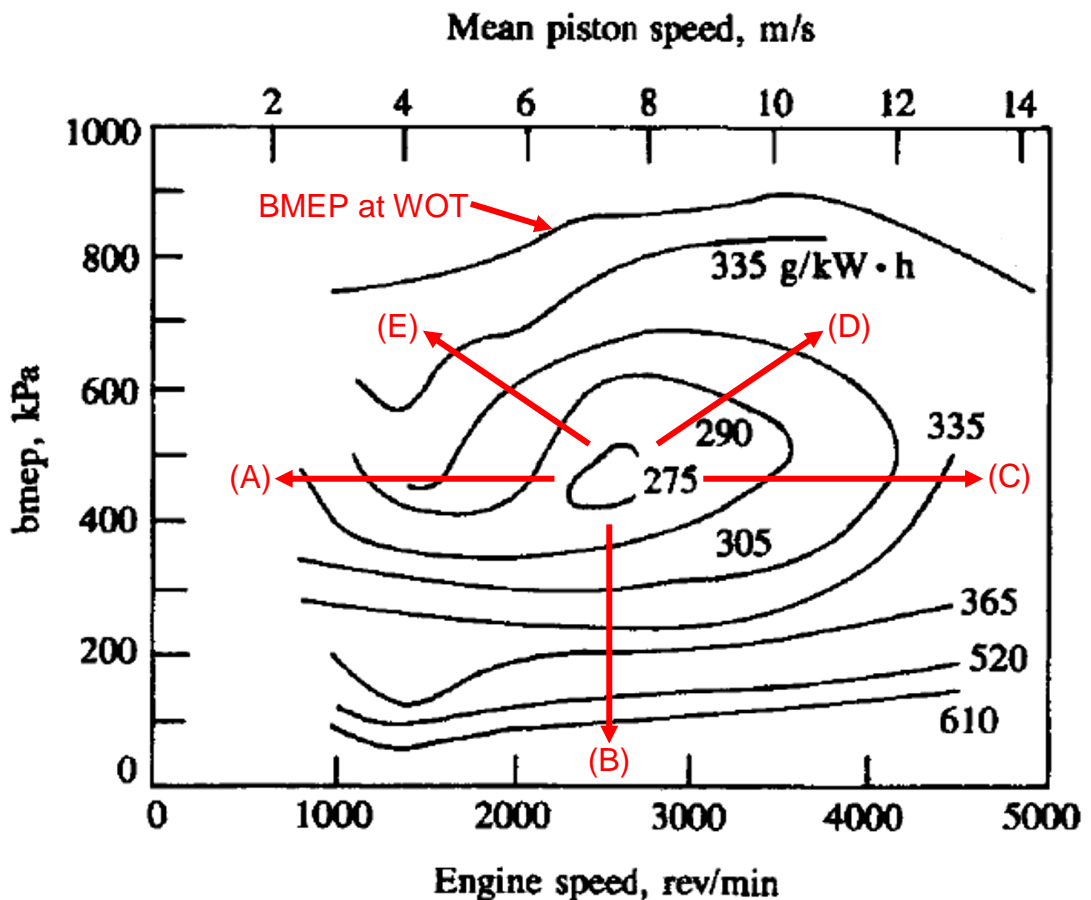
Figure 2-1: BSFC map for a typical 2.0 litre naturally aspirated four-cylinder SI engine [39]
(A) Heat losses

The contours on the map can be interpreted from the variations in volumetric efficiency, gross indicated fuel conversion efficiency (thermal efficiency) and mechanical efficiency along with heat losses, pumping losses, frictional losses and other losses (e.g. blow-by). Detailed discussions of these contours on increased BSFC (away from the minimum BSFC island) are made in the following subsections.

2.1.1 Heat Losses

As the data points deviate from the minimum BSFC island to the left, labelled as (A), meaning at constant load with decreasing engine speed. It can be derived that under these operating conditions, BSFC increases. This is primarily due to the increased heat transfer per cycle resulting in reduced thermal efficiency. SI engine heat transfer is a function of speed and load, where the heat transfer per cycle increases as speed and load decrease. Of greater importance to the cooling system is the absolute value of the heat rejection, with the heat rejected to the coolant more heavily dominated by its operating speed. At a constant load with decreasing engine speed more time is available during each cycle for the heat transfer to occur. Ultimately the higher heat losses lower the average combustion gas temperature and pressure to reduce the amount of work done per cycle remains secondary. Overall it can be said that thermal efficiency and BSFC are heavily affected by the magnitude of engine heat transfer [38], [40].

2.1.2 Pumping Losses

The red arrow labelled (B) pointing downwards identifies the operating behaviour with decreasing load at constant speed, where an increase in BSFC can also be observed. This phenomenon is attributed to increased pumping work in an engine with increasing exhaust-to-inlet pressure differential as the intake throttle is progressively closed with load. The need for such throttling arises at part-load as most modern SI engines operate with a stoichiometric fuel-air mixture to maintain three-way catalyst efficiency. In addition, "homogeneous" charge flammability limits result in the need to reduce the air mass ingested as the fuel mass, load and hence in-cylinder temperatures are reduced [40].

2.1.2.1 Pumping Work

As the throttle restricts the airflow, volumetric efficiency decreases. The intake manifold falls significantly below atmospheric pressure (vacuum), hence relative work is required across the piston to overcome this negative work (pumping loop) during the intake and exhaust strokes, as illustrated in Figure 2-2. For a given engine speed, pumping losses increase as load decreases due to reduced air and fuel flow demand [40].
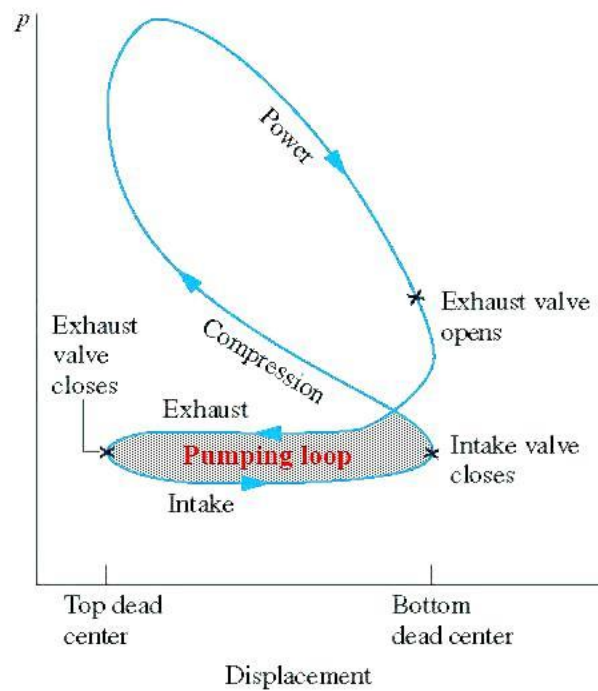
Figure 2-2: Typical P-V diagram for four-stroke SI engine under part-load with pumping loop indicated in grey shading, adapted from [41]

2.1.2.2 Idealised Otto Cycle versus Typical Real Cycle
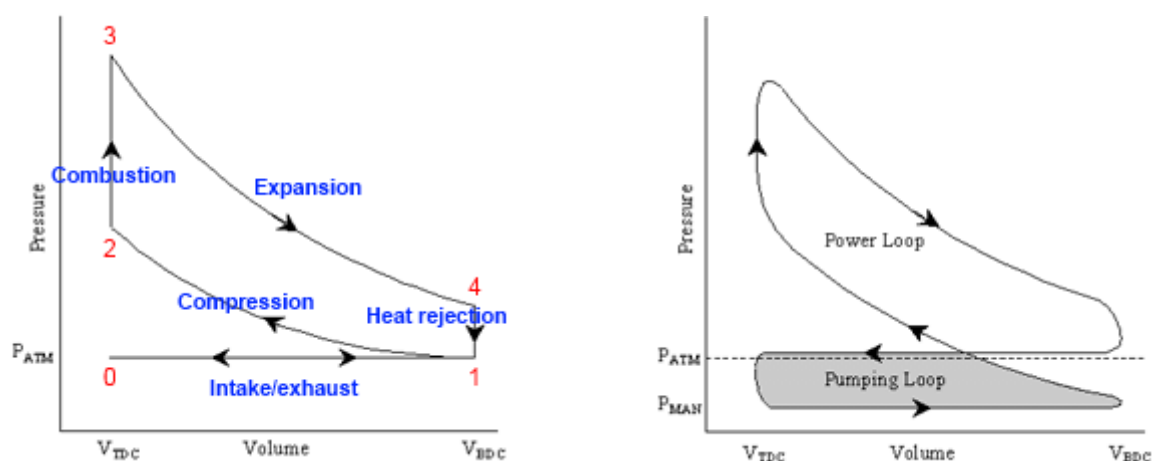
Figure 2-3: Four-stroke SI engine P-V diagrams for idealised Otto cycle (left) and typical real cycle under part-load (right), adapted from [42]

Further to the definition of pumping work above, it is useful to visualise the differences between an idealised Otto cycle (thermodynamic cycle) and a typical real engine cycle by comparing their P-V diagrams. As shown in Figure 2-3, a major difference between the two can be noticed as the pumping loop (in grey shading) is not included in the standard idealised model, meaning no associated losses occurred during the gas exchanges from the intake manifold into the cylinder (0-1), as well as from the cylinder into the exhaust manifold after combustion (1-0). In reality (as per the typical real cycle on the right), especially under part-load, work is always expended during these gas exchange processes. The net indicated work output per cycle is the difference in area of the power loop and the pumping loop and this is one of the key reasons that SI engines suffer poor fuel economy compared to diesel engines which operate without throttling under part-load. Two strategies have arisen to reduce SI pumping losses, namely 1) avoidance via technologies such as downsizing and cylinder deactivation [7], [14], [43] or pumping loop reduction via technologies such as variable valve actuation and high dilution combustion [9], [10], [44]. Other assumptions of the idealised Otto cycle include no blow-by or wall heat transfer during the compression and expansion strokes, no frictional losses, and instantaneous combustion occurring at constant volume (2-3). In practice, there are many irreversibilities associated with each process, leading to significant reduction in the achieved cycle efficiency.

2.1.3 Friction Losses

Point (C) depicts increasing engine speed at constant load. The increase in BSFC is due to increasing frictional losses at higher engine speeds and mechanical inefficiency. Although thermal efficiency increases with speed (less heat transfer per cycle, as mentioned previously), frictional losses remain dominant. Total friction work consists of pumping work, rubbing friction work (which results from the friction of all the moving parts within the engine, such as the piston-crank assembly, valvetrain, pulleys and belts) and accessory work (required to drive the engine accessories including fan, pumps, alternator etc.). The absolute value of the friction work changes with load and increases with

speed, some are proportional to the speed and some as a function of the speed squared [38], [40].

2.1.4 Over-fuelling

The red arrow labelled with (D) pointing towards the upper right corner of the map indicates the region of high speed and high load where maximum power is demanded. BSFC increases due to fuel enrichment, where Figure 2-4 below denotes the fuel enrichment zones for a typical four-stroke SI engine.
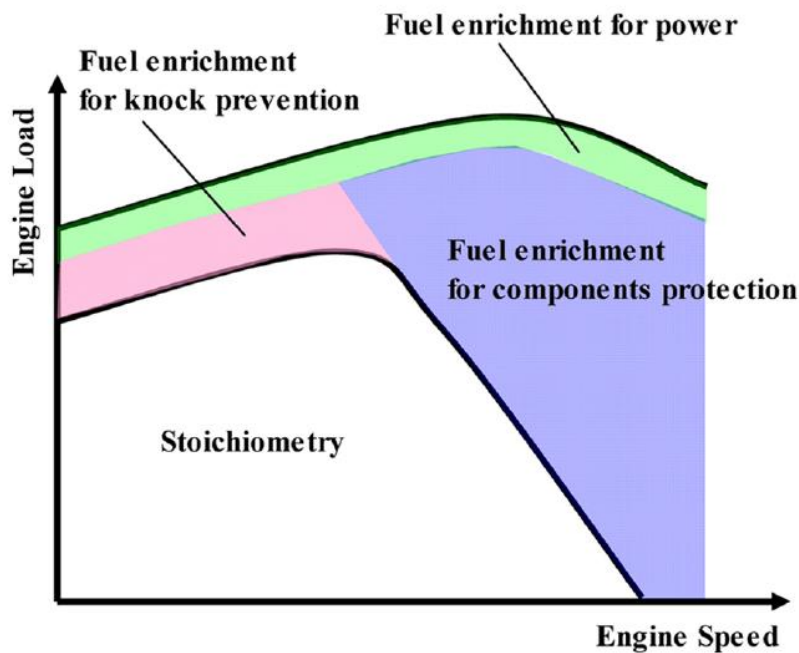
Figure 2-4: Four-stroke SI engine fuel enrichment zones, adapted from [45]

A general bias towards the high speed and high load region requires fuel enrichment for both maximum power output and exhaust component protection. Maximum power occurs slightly rich of stoichiometric, which is associated with dissociation and peak burning velocities. In addition, charge cooling effects may also come into play, with further increase in volumetric efficiency when slightly rich depending on the charge preparation and fuel injection system [38]. The additional benefit of fuel enrichment is decreased ratio of specific heats and lowered peak exhaust gas temperatures, which protects the turbocharger and three-way catalyst from excessive thermal loading [45]. In reality, modern boosted SI engines are now moving towards the adoption of integrated cooled exhaust manifolds that help alleviate the degree of over-fuelling employed [16], [46].

2.1.5 Knock

The red arrow labelled with (E) pointing towards the upper left corner of the map, illustrates the region of low speed and high load, and this is where knock primarily occurs. As also illustrated in Figure 2-4, fuel enrichment is sometimes also used for knock prevention in this region. The term knock refers to a metallic "pinging" noise associated with auto-ignition of the charge.

Downsizing (and "downspeeding") enforce a considerable proportion of "real world" operation to the low speed high load regime. Under such conditions the increased energy density of a highly pressure charged mixture leads to an increased tendency for the fuel and air to auto-ignite. The problem of auto-ignition is almost as old as the internal combustion engine itself and ultimately caps peak thermal efficiency, being commonly avoided by selecting a lower compression ratio, retarding the spark timing and/or introducing excess fuel. Such auto-ignition has been considered to be the result of exothermic centres, or "hot spots", leading to auto-ignition of the unburned charge ahead of the developing flame [47], [48]; so-called end-gas auto-ignition. However, recent aggressively downsized research engines of very high specific output have additionally experienced pre-ignition combustion at low engine speeds and high loads (>20bar BMEP). Previously pre-ignition was most commonly associated with higher engine speeds, when the components within the combustion chamber are typically at their hottest. Hence such pre-ignition was at first unexpected, arising below the auto-ignition temperature of the charge and occurring in a highly sporadic manner in short violent bursts in an "on-off" pattern, with sometimes tens of thousands of cycles in-between events [49].

This phenomenon, sometimes referred to as Low Speed Pre-Ignition (LSPI) and "Super-Knock", has been associated with low-to-moderate thermal gradients within the unburned charge leading to developing detonation events. Ultimately, this may produce multiple high frequency and intensity pressure waves within the cylinder that may interact and ultimately destroy the engine [47], [48]. Researchers at Leeds and Shell [50] have recently postulated that such Super-Knock events originate from a resonance between acoustic waves emitted by an auto-igniting hot spot and a reaction wave that propagates along negative temperature gradients in the fuel-air charge. The theory is based upon the

assumption that the temperature gradient extends smoothly over sufficient length across the turbulent flow field. Subsequently, localised detonations may develop which are then able to violently ignite the remaining unburned charge in timescales of less than a millisecond. Ultimately, this can lead to catastrophic mechanical engine failure. In existing downsized engines the phenomenon is avoided by running fuel rich, where the charge cooling properties of the excess fuel reduce pre-ignition tendency at the expense of poor fuel consumption and vastly increased tailpipe emissions (given that the three-way catalyst is not effective at these conditions). Such operation is clearly not sustainable, particularly in light of the real world driving cycles currently being proposed in the EU and elsewhere to cover a wider area of engine operation in the future.

2.1.6 Other Losses
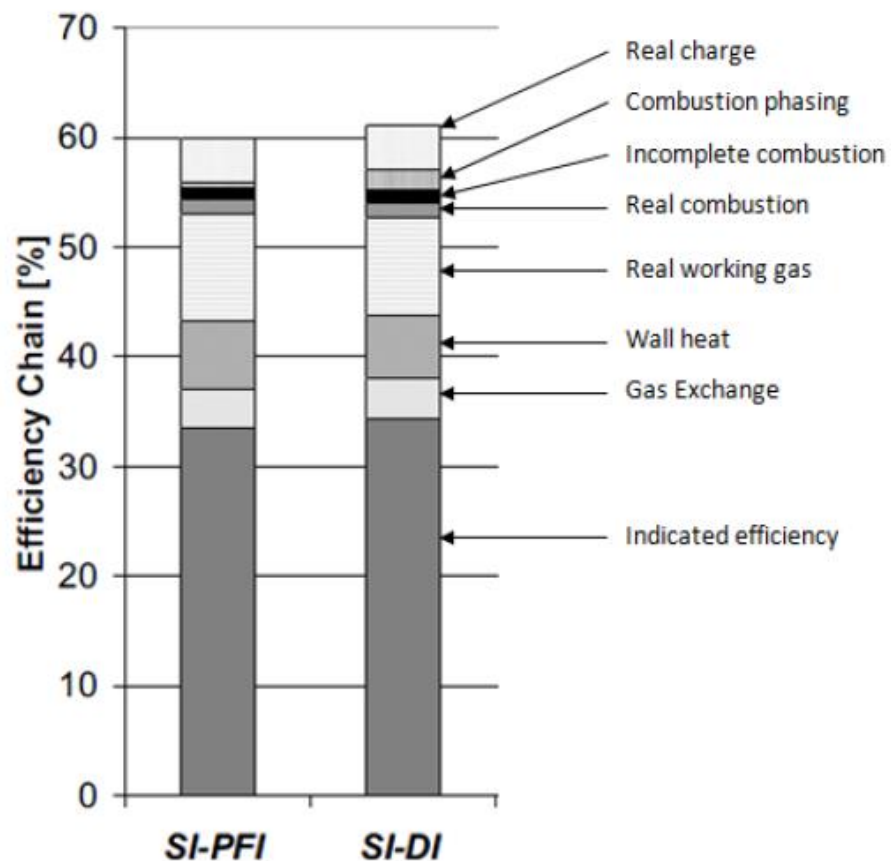
Figure 2-5: Thermodynamic split of losses compared to ideal constant volume cycle at 2000rpm at 5bar IMEP$_{net}$, adapted from [51]

In addition to the causes of losses (reduced efficiency) outlined in Section 2.1.1-2.1.5, there are still other losses present which reduce the brake fuel

consumption. Kulzer et al. [51] performed a thermodynamic "split of losses" analysis using pressure trace analysis and reverse cycle simulation, with a comparison made against the ideal constant volume cycle (Otto cycle). Figure 2-5 shows the output of the analysis for an SI engine operating at 2000rpm and 5bar net Indicated Mean Effective Pressure (IMEP$_{net}$). Both Port Fuel Injection (PFI) and Direct Injection (DI) strategies are presented, with compression ratios of 10 and 11 respectively. A slightly higher ideal efficiency (~62%) can be observed during DI operation due to the higher compression ratio (allowed by the charge cooling effect). Real charge, real combustion and real working gas irreversibilities were all accounted for within the reverse mode analysis. The analysis denotes that considerable losses are attributed to heat transfer losses through the combustion chamber walls (labelled as wall heat) and pumping losses during intake and exhaust strokes (labelled as gas exchange) as previously discussed. Furthermore, under ideal conditions, where no heat transfer (adiabatic) takes place during the ideal cycle, in reality the flame propagation occurs over a finite amount of time with dissociation effects and exhaust gas reactions not reaching chemical equilibrium, as reflected in real world combustion efficiency values for the SI of engine 95-97% [40].

2.2 SI Engine Technologies

The concept of introducing the fuel directly into the cylinder of an SI engine is by no means new, with early applications including aircraft engines [5]. The recent trend towards DI was triggered the work of Mitsubishi in applying side direct injection in combination with reverse tumble to achieve a stratified charge. The associated overall lean fuel-air equivalence ratio led to reduced part load fuel consumption. However, such early adoptions suffered problems with injection repeatability, injector fouling and unacceptable engine calibration robustness. In addition the high cost of the lean NOx trap required led to a general trend away from stratification and towards homogeneous DI as the preferred mode. A specific example of this was the early Audi "Fuel Stratified Injection" (FSI), with the stratified operation dropped soon after initial roll-out in the early 2000's due to problems with misfire (ultimately forcing Audi into a recall and calibration "re-flash" for homogeneous-only operation). Nonetheless, homogeneous operation was still considered to enable higher geometric compression ratio (~1.5), with associated NEDC drive cycle benefits of ~2% [5], [52]. In addition, the ability of

11

the injection system to improve full load volumetric efficiency (together with the inherent increased expansion ratio that accompanies compression ratio increase) allowed improved torque and peak power capability. Set out in Figure 2-6 is a database showing the benefits of such homogeneous DI when adopted in various naturally aspirated V6 gasoline engines available in the mid-2000s. The engine database behind this diagram was obtained courtesy of MAHLE Powertrain. The triangles representing the DI engines clearly demonstrate the increase in full load performance. Some noise exists due to varying friction and port/breathing performance however the effect of varying capacity is considered to vastly outweigh these effects and has been taken into account by showing specific power.
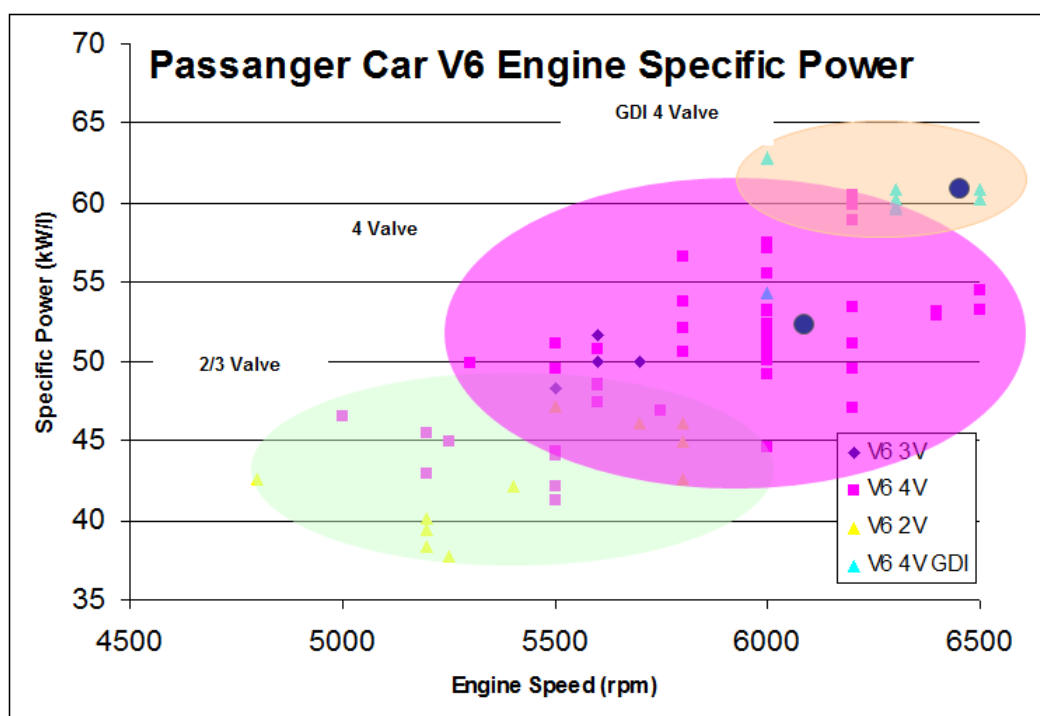
Figure 2-6: Database showing peak power engine speed versus specific power for selected PFI and DI engines available in the mid 2000s

Around the same time, multiple engine manufacturers began developing and producing the first moderately downsized automotive SI engines, which facilitated the shift to higher engine loads over the legislative drive cycles [14], [21], [26]. These engines offered strong synergy with the dual independent variable valve timing systems also more widely entering production around this time [53], [54], [55] primarily to enable internal EGR (with the associated part-

load benefits in reduced pumping, wall heat transfer and NOx and ability to reduce the residuals at full load to avoid knock and/or maximise volumetric efficiency). Such valvetrain systems are particularly attractive for downsized SI engines, where at full load and low speeds a high valve overlap strategy can be used to maximise inlet to exhaust scavenging ("blowthrough"). At higher speeds the typical fixed geometry turbocharger becomes restrictive, leading to higher exhaust back-pressure and the need to minimise valve overlap to avoid loss of load and/or knock [56], [57].
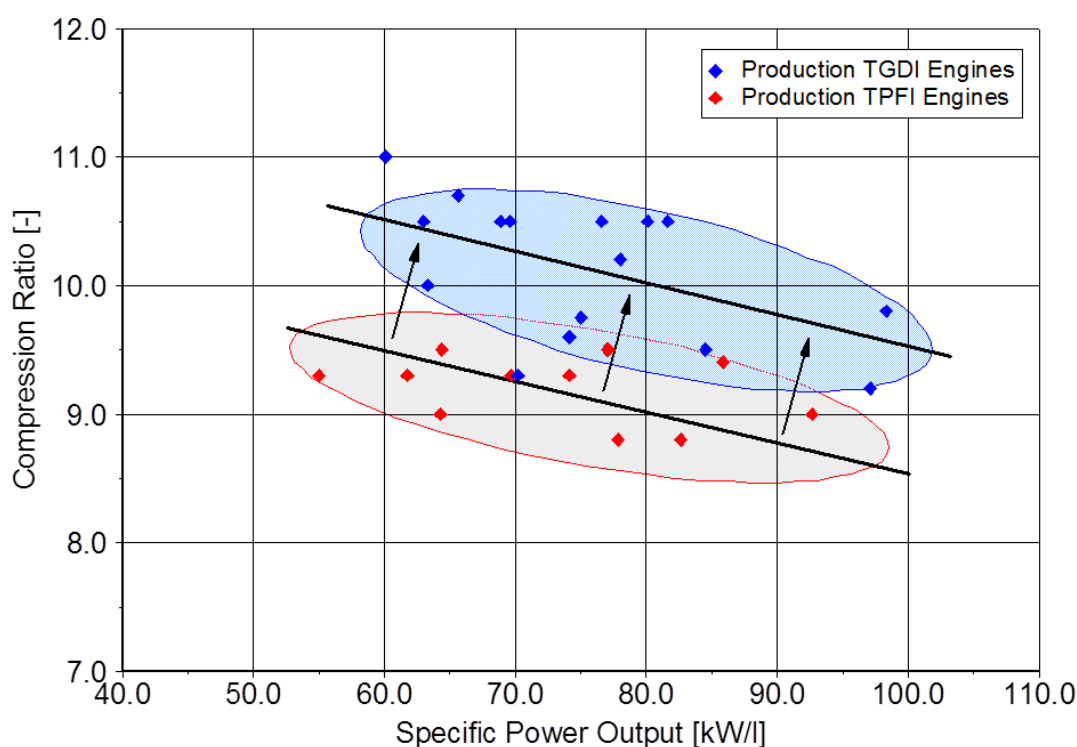
Figure 2-7: Comparison of turbocharged SI port fuel injected and direct fuel injected engine compression ratios taken from a historic database of production engines available in 2009, adapted from [6]

Direct fuel injection is considered to be critical for downsized SI engines, facilitating compression ratio to be elevated by ~1-1.5 ratios, as denoted in the database compiled by Fraser and co-workers [6] set out in Figure 2-7. The first adaptations of such downsized DISI engines included combustion chambers that were mainly based on either the wall guided or air guided side direct injection principle, with the solenoid fuel injector tip typically located underneath the two intake valves as illustrated in Figure 2-8. The air guided principle remains arguably less popular, being more heavily reliant on consistently repeatable bulk

charge motion within the cylinder, which in reality does not always occur. Many previous workers have shown that the bulk air motions may largely repeat but not necessarily on every cycle over a sustained duration [59], [60]. The same issues arise for the wall guided design, however the "ski slope" of the piston can be more reliably used to direct the initial distribution of the charge prior to reliance on the in-cylinder turbulent spectrum. The reality is that either solution can lead to remaining stratification, which in turn can result in increased NOx and PM. Furthermore, the side direct injection layout also effectively directs the fuel towards the opposing cylinder wall. Due to such cyclic variations in the flow it may still be possible for excessive fuel penetration across the bore, with increased wall wetting also well known to be associated with increased pollutant emissions and detrimental oil dilution.
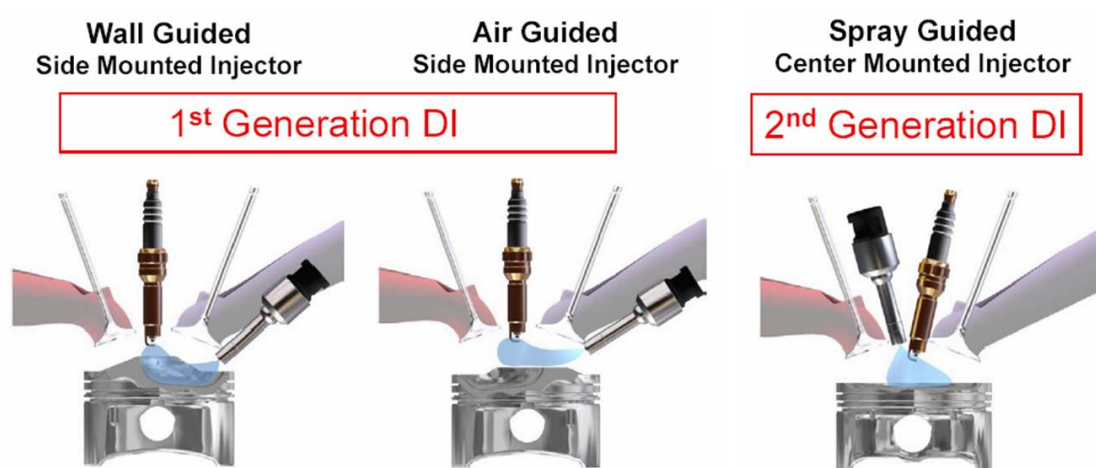
Figure 2-8: Illustration of the typical wall guided, air guided and spray guided direct fuel injector layouts, adapted from [58]

As a result of these problems, and also due to advancements in fuel injector design and fuel pressure control, the central direct injection layout has arguably become more attractive to many engine manufacturers. This layout was the subject of significant research by Ford in the early to mid 2000s [58], with a solenoid-actuated inwardly opening multi-hole injector concept investigated as a low cost solution. It was concluded that such a system layout had the potential to reduce wall wetting and further improve fuel economy by up to ~5% over the NEDC by extending the stratified charge window. However, the inward opening multi-hole injector evaluated was prone to injector fouling, with poor repeatability

when adopted for stratified charge. As a result the outward opening piezo injector has been adopted by premium automotive manufacturers wishing to pursue a stratified charge combustion system (notably including BMW and Mercedes). In recent work by Schmidt and co-workers [61], the outward opening fast acting piezo injector was found to offer high repeatability along with the ability to introduce the fuel in multiple injection events. Schmidt and co-workers concluded that an apparent shift in in the optimum 50% mass fraction burned angle towards TDC was associated with the near adiabatic combustion, where the delivery of the fuel in multiple packets enabled precise control over flammability away from at least part of the chamber walls. However it was also noted that the calibration was highly sensitive and potentially difficult to control under real world transient operation.

In the last few years some automotive engine manufacturers have looked to combine downsized SI engines with fully variable valvetrain technologies, which ultimately allow yet further reductions in fuel consumption and CO_2 over the legislative cycles. When fitted to the exhaust, switching duration valvetrain technology can be used to increase the blowdown pulse and spin up the turbocharger for enhanced low speed torque [62] albeit at the expense of reduced expansion ratio and hence thermal efficiency. Elsewhere, various workers have considered variable intake valve durations to facilitate Miller cycle operation, with increased expansion-to-compression ratio and (provided sufficient boost is available) the ability to partially further compress the charge prior to entry to the cylinder. In turn the charge can be intercooled to reduce the propensity to knock [63]. At the time of writing this thesis, workers at Ford were considering the use of such switching valvetrains to facilitate cylinder deactivation, with Ford actively researching a "rolling deactivation" technology [64] to maintain temperatures across the engine assembly.

In addition to hardware optimisation, in recent years there has also been high interest in manipulation of the fuel to improve charge preparation in DISI engines, including fundamental studies of the flash boiling phenomenon of a directly injected fuel spray. Such flash-boiling may occur when a superheated liquid is expelled into an environment with lower pressure than the fuel saturation pressure. These conditions sometimes exist in DISI engines when operating at low in-cylinder pressures and/or high fuel temperatures. Fuel flashing plays a significant role in mixture formation by promoting faster breakup and higher fuel

evaporation rates compared to non-flashing conditions. Price and co-workers [65] undertook computational modelling of flash-boiling of n-Pentane and iso-Octane sprays using a Lagrangian particle tracking technique. The computational results were validated against optical experimental data obtained previously with the same injector by high-speed imaging techniques. Ultimately these workers were able to predict spray collapse, with the tool being suggested to enable future study of new fuel additives and blends to promote such rapid fuel air mixing with minimal wall wetting.

2.3   Particulate Formation in DISI Engines

Delivery of the fuel directly into the cylinder inherently results in delay in charge mixing, with increased chamber wall wetting primarily governed by the penetration, break-up and atomisation of the spray that varies with overall operating conditions. Ultimately some degree of charge stratification often remains, even under "homogeneous" targeted conditions [66], [67]. As a result DISI engines may produce increased particulate emissions compared to fully optimised Port Fuel Injection (PFI) counterparts. Such particulate emissions contribute to atmospheric pollution and have been shown to be hazardous to human health [28]. Particulate Matter (PM) number concentration and morphology could be more relevant toxicological metrics than the total PM mass, which is especially concerning for DISI engines which have been reported to be a bigger contributor to ultrafine and nano-sized particulate emissions [29], [30], [31].

Particulate matter emissions emitted from internal combustion engines mainly comprise of solid carbonaceous material (soot), Volatile Organic Compounds (VOC's), sulphur and ash. While soot is generally formed from locally rich combustion of the fuel and oil, the VOC's mainly arise from vaporised oil and fuel in the crevice volumes. The sulphur arises from the fuel, whereas the ash consists of any non-combustible metallic additives in the fuel and oil as well as metallic particles from engine wear [31]. In automotive applications, diesel vehicles have been historically considered as the major source of PM emissions, with both PM mass and Particulate Number (PN) now being regulated fairly strictly. Even though gasoline vehicles emit relatively low PM emissions by mass, recent studies have shown that modern gasoline engines may emit substantial

amounts of ultrafine and nano-sized particles. Once released into atmosphere, these superfine particles of very low mass but high number [68], [69], [70], may penetrate deep into the lungs and ultimately may cause cardiovascular disease [28], [31]. For these reasons, Europe has recently finalised the regulation for its PM emissions on DISI engines, with not just PM mass but also PN (6.0×10^{11} #/km) restricted, to be effective from September 2017 (Euro 6C). Similar proposals were also included by the California Air Resources Board (CARB) for the upcoming LEV III. Although the PN emissions target has not yet been set the intention of PN to be regulated in the future is firm [32], [33].
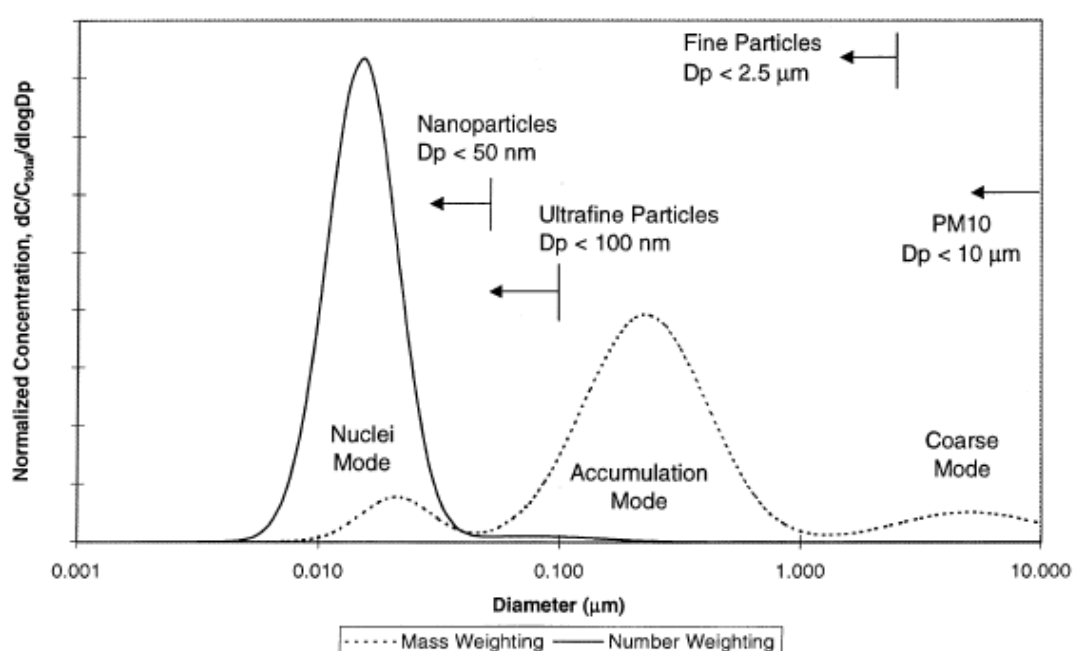
Figure 2-9: Idealised Diesel exhaust particulate number and mass weighted size distributions, adapted from [31]

Shown in Figure 2-9 are idealised diesel exhaust particle number and mass weighted size distributions. The distributions shown are trimodal, lognormal in form. The concentration of particles in any size range is proportional to the area under the corresponding curve in that range. Most of the particle mass exists in the so-called accumulation mode in the 0.1-0.3 micron diameter range. This is where the carbonaceous agglomerates and associated adsorbed materials reside. The nuclei mode typically consists of particles in the 0.005-0.05 micron diameter range. This mode usually consists of volatile organic and sulphur

compounds that form during exhaust dilution and cooling, and may also contain solid carbon and metal compounds. The nuclei mode typically contains 1-20% of the particle mass and more than 90% of the particle number. The coarse mode contains 5-20% of the particle mass. It consists of accumulation mode particles that have been deposited on cylinder and exhaust system surfaces and later re-entrained. Also shown in Figure 2-9 are some definitions of size for atmospheric particles. PM10 and fine particles are actually defined by standard sampling systems in which the sampling probability falls to 50% at the designated aerodynamic diameter. Exact definitions of ultrafine and nanoparticles have not been agreed upon. Note that by number, nearly all of the particles emitted by a diesel engine (the same is true for a spark-ignition engine) are nanoparticles. As particulate filters are adopted for diesel engines and potentially for gasoline engines in the future as mentioned previously, the particulate size becomes increasingly important. Although the two metrics for particulate emissions (both mass and number) do not require particulate size measurements under current legislations, the efficiency of filtration of a GPF or a DPF (Diesel Particulate Filter) is heavily size dependent.

In terms of prior observed fuel effects, Price and co-workers [67] undertook a detailed study of the particulates produced in a modern spray guided DI engine when operating on gasoline-ethanol or gasoline-methanol blends. With up to 30% alcohol adopted the particulates produced were relatively similar. When stoichiometric, E85 resulted in the lowest PM number concentrations. For methanol, M85 fuel led to consistently higher number concentrations although mainly in the nucleation mode. However, the accumulation mode concentration was actually lower than gasoline which suggested lower overall PM mass.

2.4 Alternative Fuels

As the expected shortage of crude oil will sooner or later become a limiting factor, sourcing alternative renewable energy is another problem facing the automotive industry. Alcohol based fuels are one major candidate to displace fossil fuels, especially if they can be blended within the existing gasoline pool for widespread displacement [34]. Ethanol and gasoline blends have been widely adopted as first generation biofuels, while ethanol can be produced from renewable sources and incur advantage in source to wheel CO_2 emissions [35]. Nonetheless,

issues of practicality remain on current wheat ethanol due to feedstock being limited globally, hence in the long term cellulose ethanol may dominate [36] albeit significant challenges remain before this can be considered as viable on a grand scale [37]. Two key significant advantages of ethanol are high latent heat of vaporisation and the associated high octane number providing knock resistance, providing the DISI "charge cooling" effect and improved performance [71]. On these terms ethanol seems a favourable component within gasoline for future boosted DISI engines, where higher compression ratios can be utilised to further improve fuel economy. However, the Lower Heating Value (LHV) of ethanol, at a reduction of ~33% in comparison with gasoline, is a major drawback which results in increased volumetric fuel consumption. Additionally, the high latent heat of vaporisation and differences in vapour pressure lead to an adverse effect on cold-start behaviour of gasoline-ethanol blends [72]. Furthermore, in recent years, reports on PM emissions of gasoline-ethanol blends in DISI engines remain highly contradictive. For example, Storey et al. [73] stated reduced content of ethanol in the fuel (E10-E20) decreases PM emissions, while He et al. [74] observed lower content of ethanol has similar PM emissions as gasoline. Elsewhere, Francqueville [75] demonstrated an increase in ethanol proportion (E85) decreases PM emissions, whereas Chen et al. [76] concluded both PM mass and PN emissions increase with the ethanol content of the fuel increased.

Chapter 3 Experimental Test Facilities

3.1 Engine Test Bed

The engine test bed consisted of a bespoke optical single cylinder DISI research engine, mounted on a Cussons single cylinder test bed with integrated dynamometer, oil and coolant control systems as described in more detail below. The engine has been used extensively at Brunel for several years, as reported previously by prior workers including Tongroon [77] and Anbari Attar [78].

The operation and control of the engine speed and load were carried out via a dynamometer manufactured by McClure. It was an electric DC machine which had a continuous power rating of 30kW with a maximum rotor speed of 6000rpm, rated at 400 volts and 70 amps. The assembly could be used as a DC motor to drive the engine for starting and motoring operations (i.e. when the engine was operated as an air compressor with non-firing operations) via its KTK thyristor converter unit and/or as a DC generator during engine braking operations (i.e. when the engine was operated as an air expander with firing operations). Whilst performing the engine braking operations, the DC power generated by the dynamometer was converted to three-phase AC power by the converter unit and fed back into the mains supply. A speed signal was provided by a tachogenerator mounted on the dynamometer shaft so that the speed selected at the control console by the operator was maintained within an accuracy of < ±5rpm by automatic adjustments to the motoring or loading torque. As is usually the case with single cylinder research engines, cyclic variations in speed were reduced via an oversized flywheel directly coupled to the engine crankshaft. In addition, the Cussons rig includes an appropriately heavy base plate to help dampen the vertical vibrations (essential in optical work, with acceptable low vibrations verified by a crude "penny test" i.e. placing a penny on the optical head and observing no movement during motoring or firing). The cooling method for the dynamometer was via an electrically driven force ventilation fan mounted on the base frame.

The lubrication and coolant circuits were integrated into the test bed base frame. A schematic of the circuits is presented in Figure 3-1. The engine coolant was a mixture of de-mineralised water and commercial anti-freeze with a mixing ratio of 1:1. The coolant was drawn from the bottom of the header tank and pumped

through the heat exchanger before entering into a three-way valve which separated and controlled the flow for both the engine block and cylinder head, which operated on fully separated flow paths. Upon exiting the engine, the coolant was returned to the top of the header tank via separate return pipes. In order to achieve a desirable operating temperature prior to and during starting and motoring operations, an electric heater was in place within the system. The coolant temperature was measured and controlled via a closed loop system by a Spirax Sarco sensor mounted in the vertical sub frame of the header tank. The lubrication system was comprised of a pump driven with an AC motor and a heat exchanger fitted among a closed loop control system that monitored and controlled the oil temperature by another Spirax Sarco sensor. Both the coolant temperature (with an accuracy of $< \pm 2°C$) and oil temperature ($< \pm 4°C$) could be adjusted on the control panel to fulfil different operating requirements.
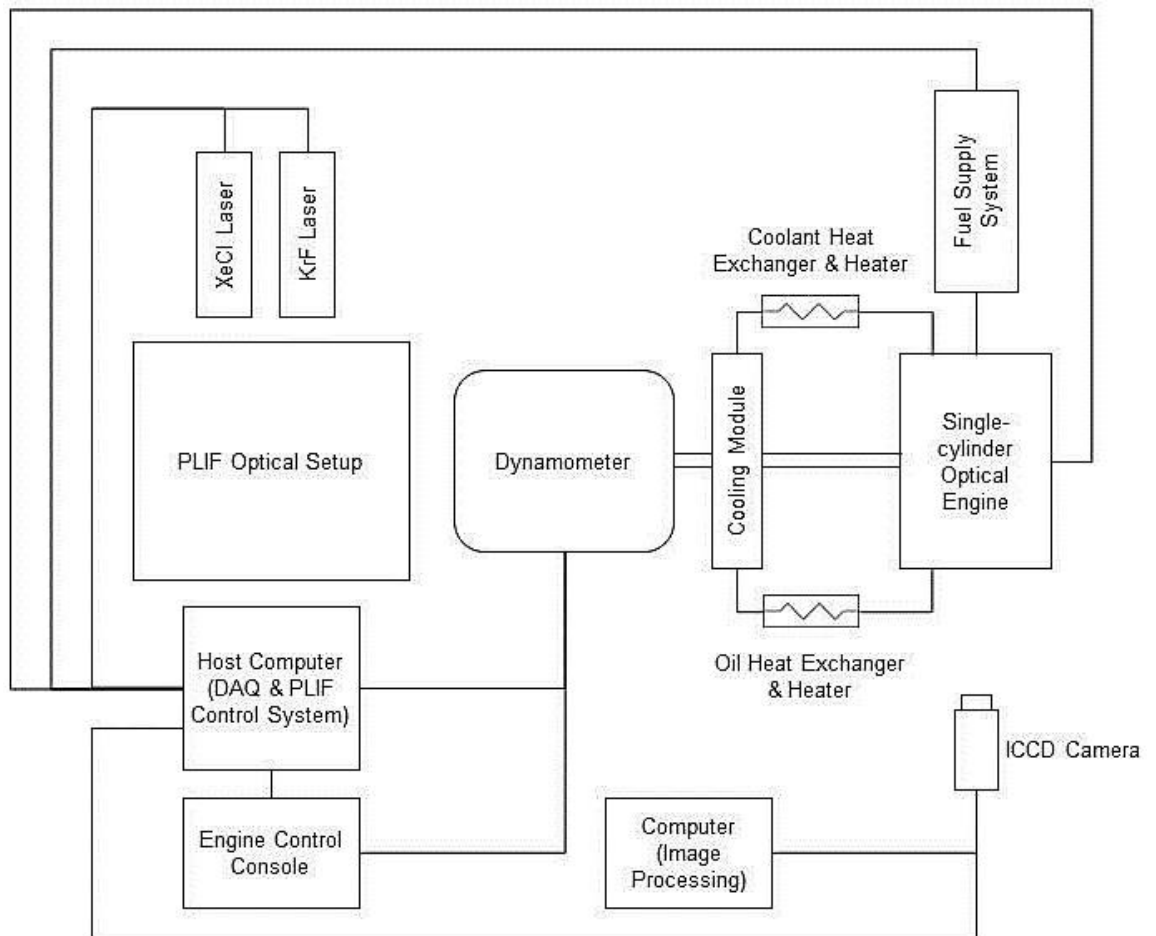
Figure 3-1: Laboratory setup (top) and experimental setup schematic (bottom)

3.2 Experimental Engine

The experiments were performed in a bespoke optical single-cylinder DISI research engine representative of a modern pent-roofed four valve central direct injection layout. This engine had a swept volume of 447cc with its stroke and bore being 89mm and 80mm respectively. A compression ratio of 8.67:1 was calculated by taking into account the actual Bowditch piston dimensions after assembly. The chosen camshafts used were intended to perform under SI operations with both normal and positive valve overlap timing, the set had a valve lift of 9mm with 220°c.a. duration (end of ramp) with the valve timing set at EMOP at 265°aTDC (compression) and IMOP at 455°aTDC (compression) leading to 30°c.a. positive valve overlap. The key engine specifications are listed in Table 3-1.

Table 3-1: Key engine specifications

Displaced volume	447cc
Stroke	89mm
Bore	80mm
Compression ratio	8.67:1
Inlet valve diameter	29.5mm
Exhaust valve diameter	21mm
Valve lift	9mm
Cam duration	220°c.a. (end of ramp)
EMOP	265°aTDC (compression)
IMOP	455°aTDC (compression)

The bottom end was based upon a standard Ricardo Hydra SI unit as previously described by Tongroon [77], fitted with a custom extended block and an extended piston (Bowditch) as illustrated in Figure 3-2. The extended cylinder block was made from a cast iron barrel with centrifugal cast wet liner, which bolted onto the lower cylinder block that was attached to the crank case.
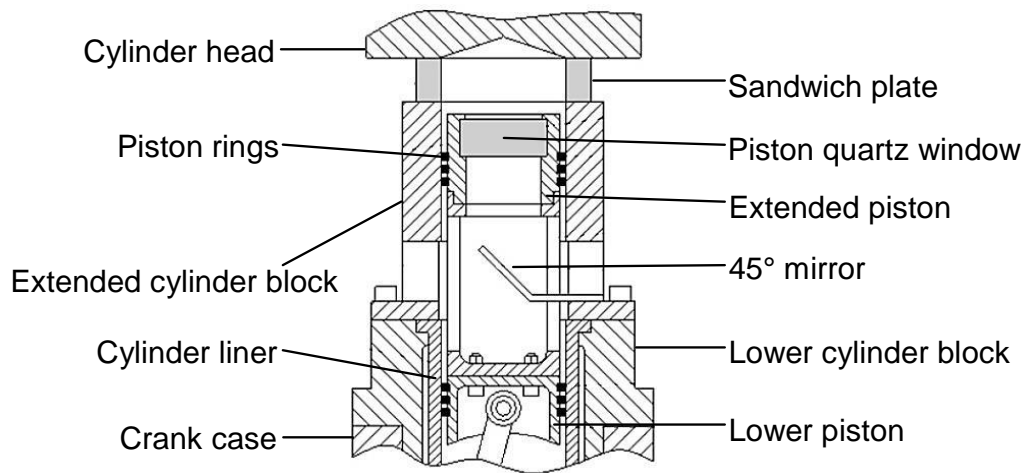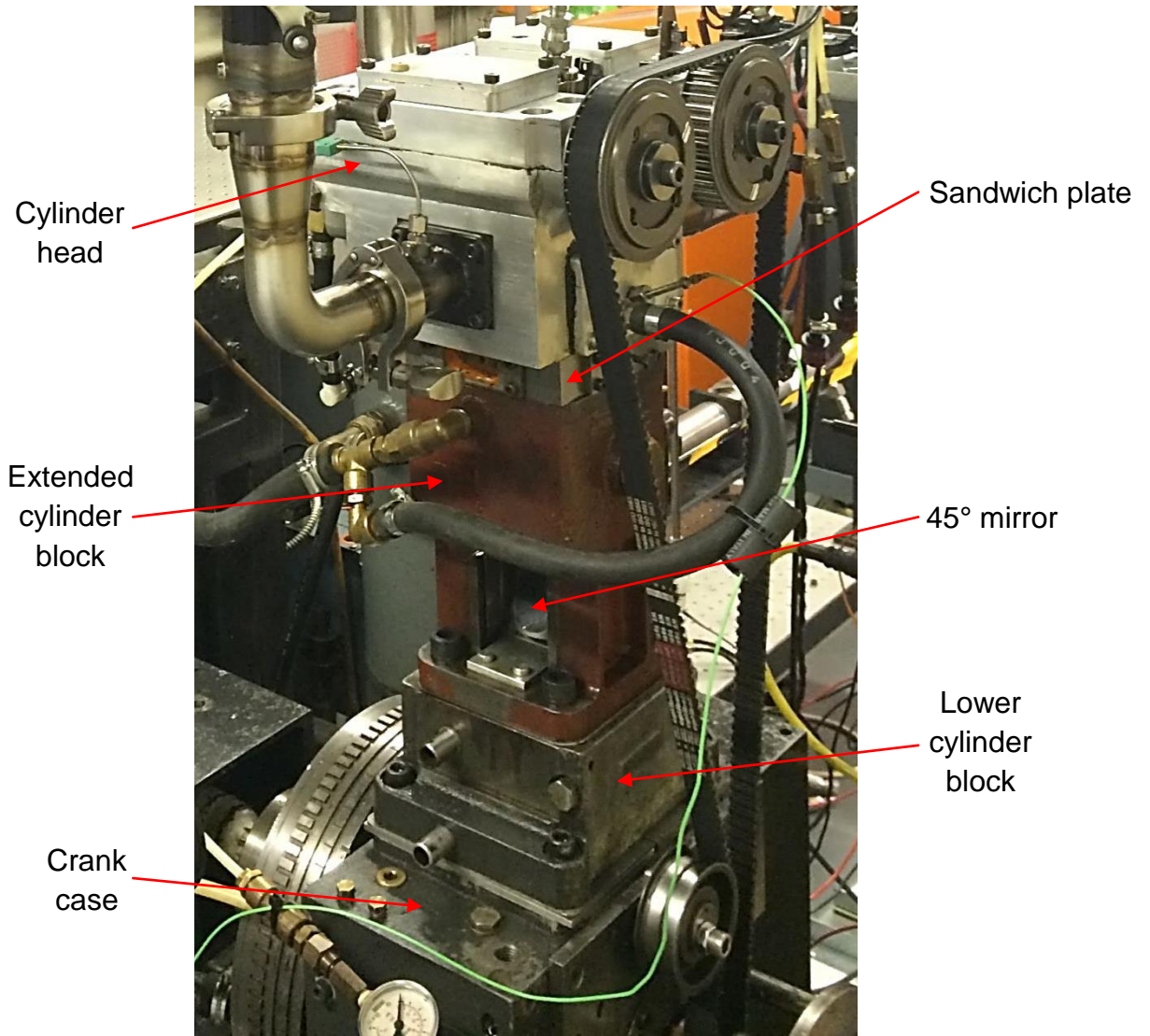
Figure 3-2: Bespoke engine assembly (top) and engine setup schematic (bottom)

Set out in Figure 3-3 is a picture of the Bowditch piston assembly. This extended piston was made of aluminium utilising two PTFE compression rings lubricated with grease. The piston crown included a $\varnothing$55mm flat-topped quartz piston window providing access to ~50% area of the bore when considered on a planar basis. The lower piston operated in the lower cylinder block had a conventional ring pack with two compression rings and one oil control ring.
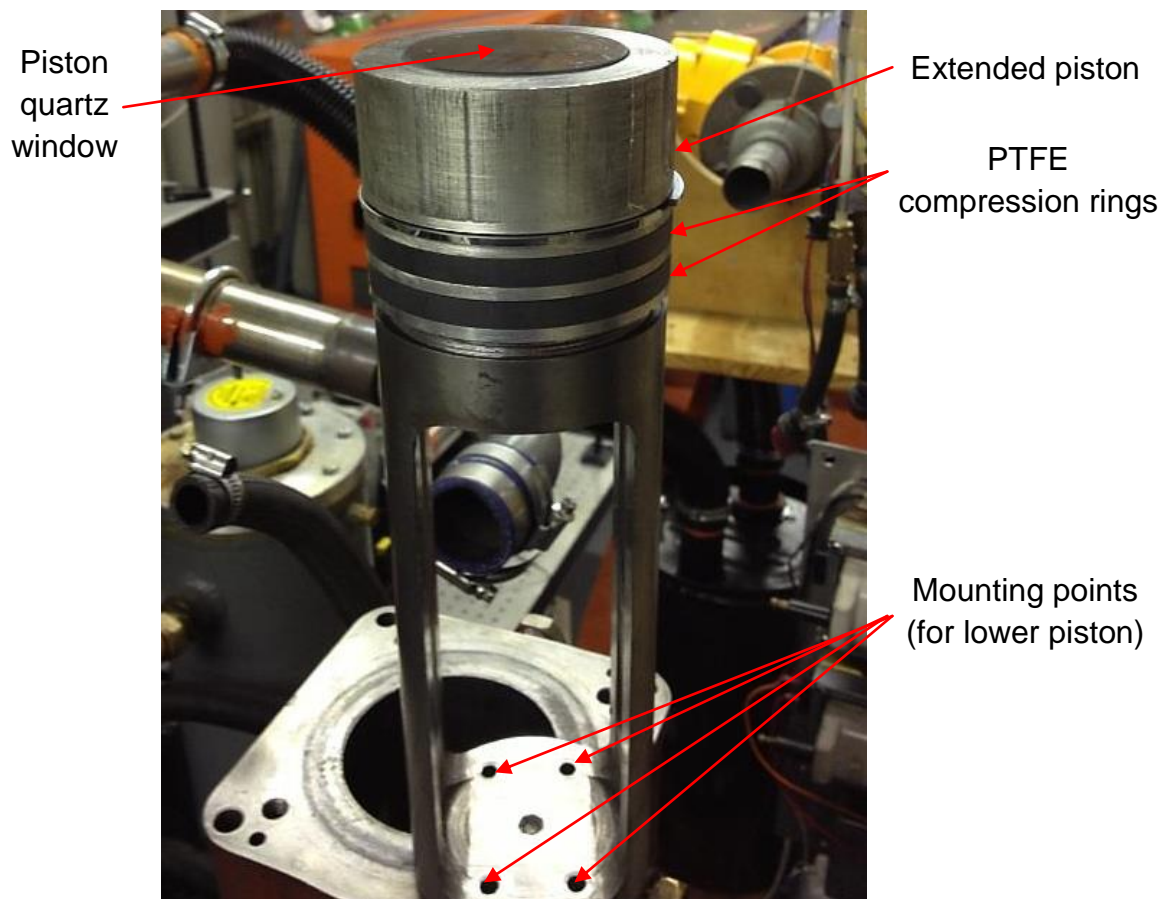
Figure 3-3: Extended cylinder/piston assembly

A sandwich plate was designed to mate between the cylinder head and the extended block as shown in Figure 3-2, with additional optical access to the combustion chamber available via two side windows of 21mm height and 45mm width. In the current work these were used to allow laser light entry in a plane through the combustion chamber with the piston at 30°bTDC firing, where the laser sheet was aligned at 5.77mm above the optical piston and 10.5mm below the spark plug for an optimised location for fuel distribution visualisations.

The cylinder head was a machined-from-solid prototype originally supplied to Brunel by the Orbital Engine Corporation Ltd, where the combustion chamber

was of pent-roof spray-guided direct injection design, with four valves operated by double overhead camshafts housed in an aluminium casing. A view of the combustion chamber is provided in Figure 3-4. The original design was produced to help evaluate the Orbital air assisted direct fuel injection system, which was removed and replaced in the currently reported thesis as detailed below.
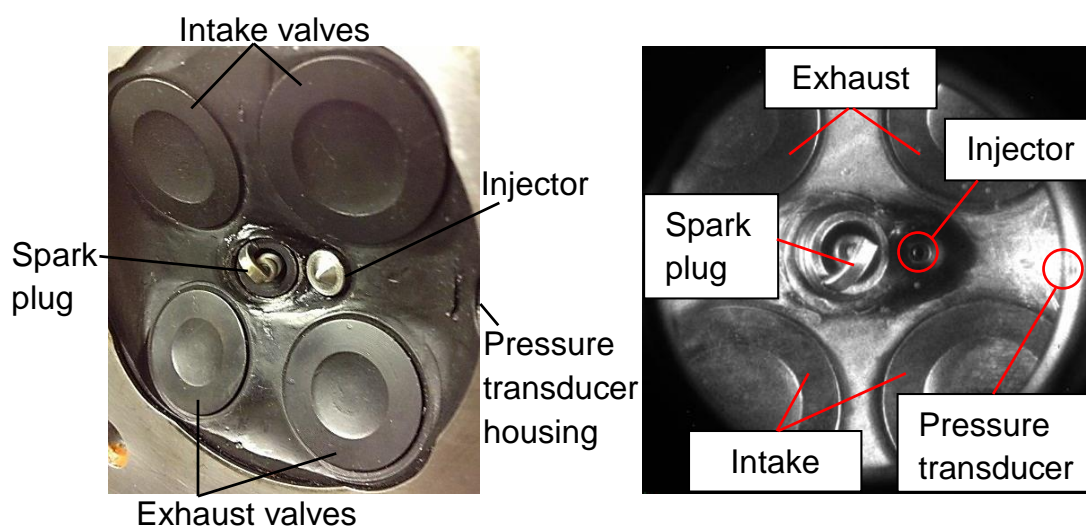
Figure 3-4: Bottom view of the combustion chamber (left) and view via 45° mirror (right)

The in-cylinder pressure transducer used throughout the experiments was a Kistler type 6055B80 piezoelectric pressure transducer which mounted flush with the chamber wall. In order to achieve accurate measurements, the transducer must be checked and calibrated beforehand. A dead weight pressure gauge tester was employed for such purpose, by assigning the voltage signal outputs from the transducer to the correct pressure readings. The process involved cleaning the face of the transducer in an ultrasonic bath then attaching it to the hydraulic circuit of a "dead weight" testing rig. The hydraulic circuit was then pressurised by adding known loads (precision weights) to the balancing piston of the tester, the corresponding voltage signal outputs provided by the transducer could then be linearly correlated by applying a range of different weights within the full measuring range of the pressure transducer. Since the anticipated maximum in-cylinder pressure throughout the operations would not be exceeding 100bar, the transducer was calibrated within this range with the time constant of the charge amplifier set to 'long' for calibration purposes, this would be selected to 'short' throughout the actual experiments to account for the rapid change in

pressure during in-cylinder pressure measurements. The corresponding pressure-to-voltage ratio was 10.03bar/V, which was entered in the data acquisition software for the relevant pressure calculations.

Another critical factor affecting the accuracy of in-cylinder pressure measurement is the determination of thermodynamic loss angle; which is the measure of the angle before TDC at which the peak motoring in-cylinder pressure arises due to thermodynamic irreversibilities including heat transfer and mass blow-by. Prior worker at Brunel [79] has concluded that the use of a capacitive probe allows the most accurate determination of the loss angle, where the engine may be motored under warmed up conditions and the loss angle directly measured in a dynamic testing condition (albeit without combustion present). Unfortunately no such probe was available at Brunel at the time of the tests. Therefore a loss angle of 1.0 was selected based on prior experience of optical SI engines and the general recommendation of the pressure measurement manufacturer, AVL. This assumption was considered to be acceptable given the pressure measurement was mainly required for qualitative analysis.

The injector used throughout the tests was a current production Piezo unit manufactured by Siemens (MAHLE Part Number: NGM00084766), which sprayed a 90° conical plume of fuel. The injector was identical to that adopted by MAHLE Powertrain is early testing of their DI3 downsizing demonstrator engine [15], who kindly provided design information in terms of the external packaging of the injector and recommended location of the spark plug relative to the plume. To achieve the precise requirements for the spray pattern, moderate modifications to the cylinder head and injector were carried out to comply with these manufacturer guidelines, as illustrated in Figure 3-5. While the recommended peak operating pressure of the injector was 200bar, the burst pressure of the injector was informally confirmed to be 275bar.
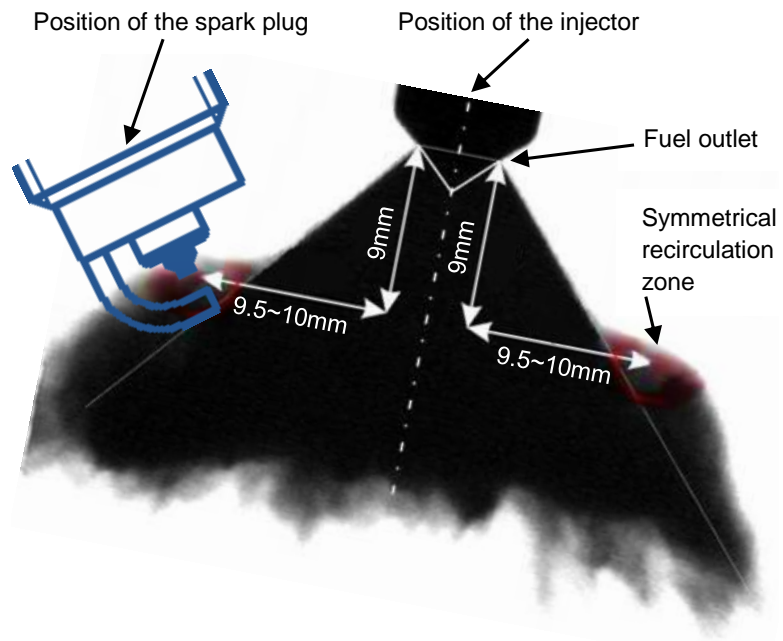
Figure 3-5: Manufacturer guidelines for injector location (provided courtesy of MAHLE Powertrain)
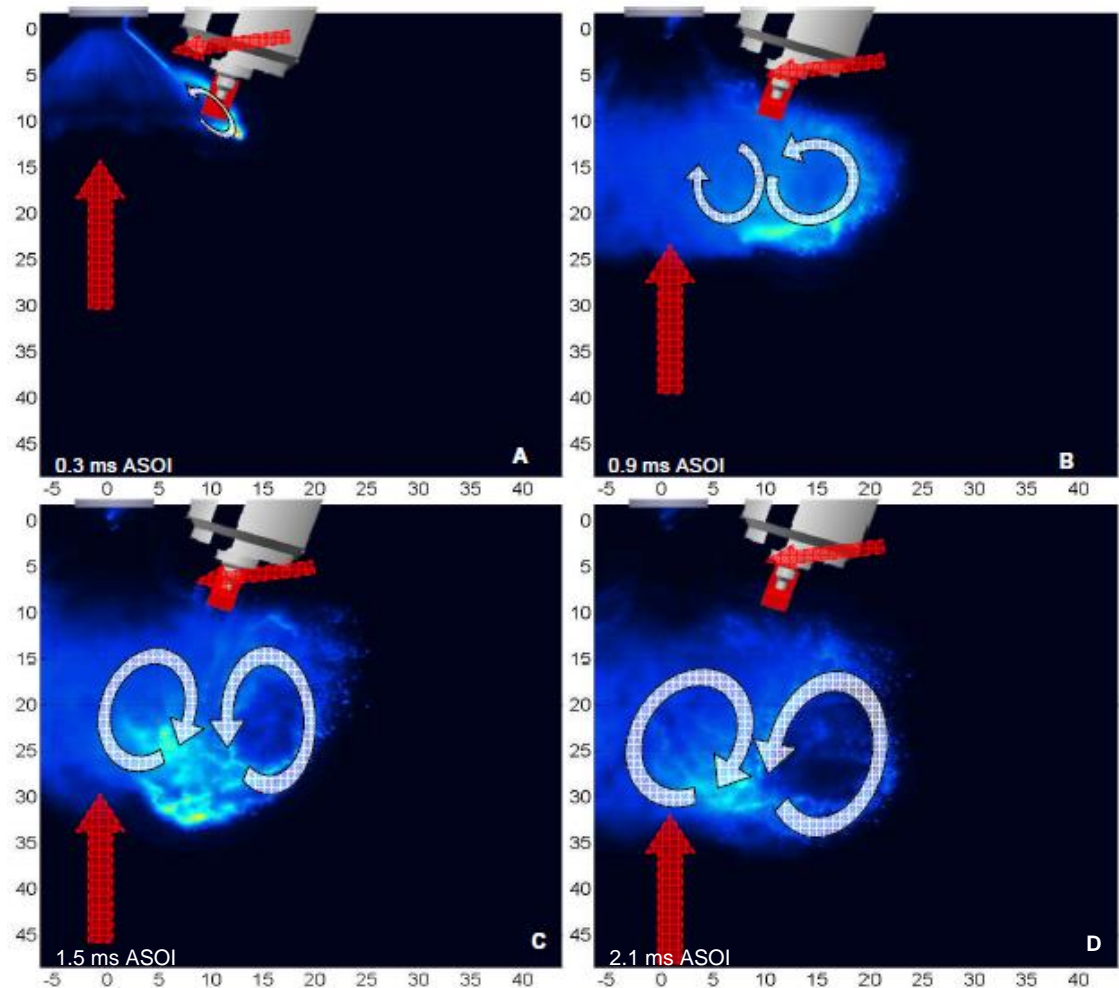

Figure 3-6: Planar Mie images showing the liquid fuel distribution at four time points during a single injection of 10mg fuel at 200bar [80]

Researchers at Chalmers University of Technology Gothenburg [80] have experimentally investigated the spray formation and consequent atomisation of such outward opening piezoelectric gasoline DI injector mentioned above using a constant pressure spray chamber. The sizes and velocities of the droplets and the resulting spray shapes were evaluated by adopting Planar Mie scattering and PLIF techniques (with same fuel and tracer configurations used throughout the currently reported thesis) combined with Phase Doppler Anemometry (PDA) analysis and high-speed imaging. Figure 3-6 (A – D) shows the spray formation via Planar Mie images illustrating the shapes and movements of the spray generated by a single injection of 10mg fuel under 200bar rail pressure at four different time points.

The original design of the cylinder head was based on the air assisted fuel injector for prior work with Orbital. For the current work, it was necessary to undertake moderate modifications to accommodate modern injectors including the Piezo type mentioned above and also a Bosch (MAHLE DI3) multi-hole solenoid injector intended for back-to-back comparisons as future work, however this was not carried out due to time constraint. The modifications involved first reviewing and reverse engineering the existing configuration of the cylinder head (as the Orbital drawings were not available). It was necessary to enlarge the diameter of the hole for the injectors but this was possible without relocating the location of the spark plug. This modification was possible as the cooling jacket did not pass between the plug and injector (as would normally be the case in a production cylinder head). Such lack of injector tip cooling was not ideal and was only considered viable given the typical limited test duration during optical engine tests. It is critical that any future testing on this engine takes this limitation into account, to avoid premature injector failure. Another pre-requisite of the re-design was to allow the piezo and multi-hole injector to be interchangeable, therefore it was concluded that a common sleeve was needed to address the issue of the differing outer dimensions of the two injector tips.

Prior to designing the sleeve, spare fuel injectors were sourced and cut open. This was necessary to measure the internal wall clearances and establish if any machining of the end tip of the injectors was feasible. This crude reverse engineering left considerable risk of unit failure, but this was considered acceptable given no direct information was available from the injector supplier. Set out in Figure 3-7 and Figure 3-8 are the views on the donor multi-hole unit
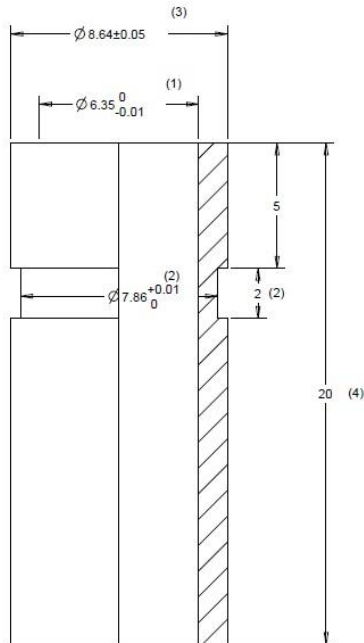
and Piezo type respectively before and after dissections, both internal wall thicknesses were found satisfactory for further machining.

Figure 3-7: Multi-hole solenoid injector external (left) and internal (right) views

Figure 3-8: Piezo type injector external (left) and internal (right) views

(1) -
    To match it, the injector tip will be machined
    to $\varnothing$ 6.35(upper+0.040; lower+0.025)

(2) - Measured from the injector which uses the determined seal

(3) - Measrued from the injector which uses the determined seal
    To match it, the cavity in cylinder head will be enlarged from
        $\varnothing$ 8 to $\varnothing$ 8.75$\pm$ 0.02

Machining Process

1 - Inner diameter(1) and axis dimension(4) shall be machined first

2 - Insert the injector into the pre-machined sleeve.
    A tight interference fit shall be applied.

3 - Other dimentions to be machined

Material

- Mild Steel

Figure 3-9: Sleeve design

The design of the sleeve was then finalised and manufactured to be fitted with an interference of 0.025 – 0.050mm onto the injector tips, as illustrated in Figure 3-9.
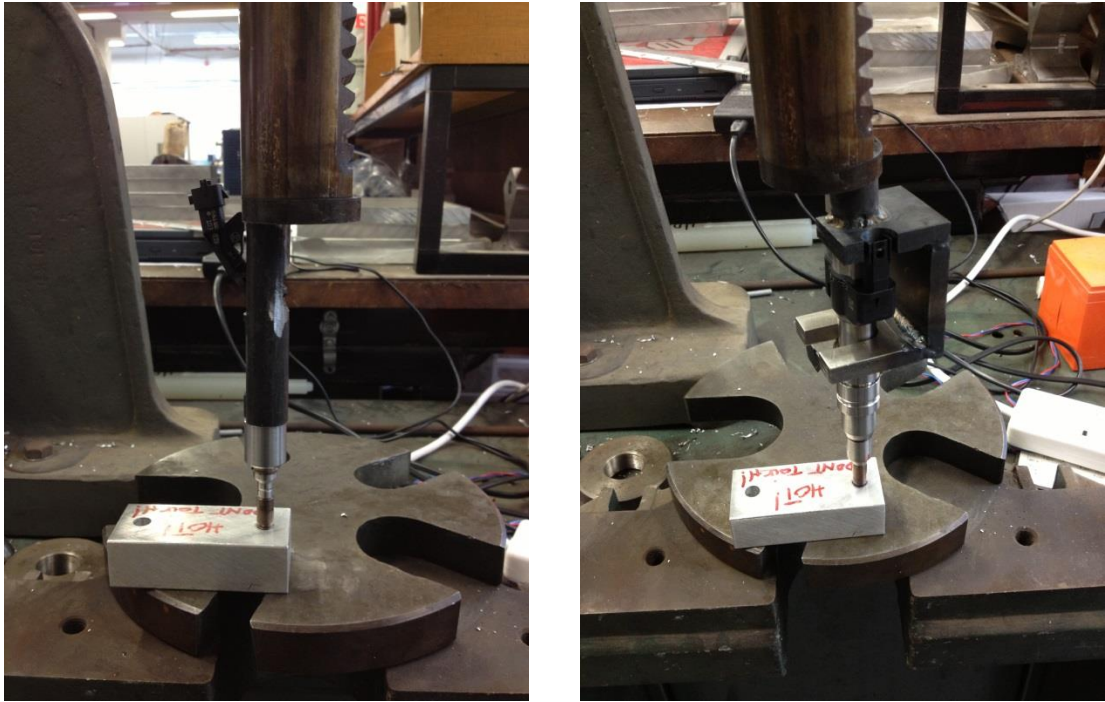
Figure 3-10: Sleeve press fitting - Multi-hole solenoid injector (left) and Piezo type (right)

Figure 3-10 shows the sleeves are being press fitted onto both injector tips, where left view shows the multi-hole solenoid injector and right view shows the piezo unit.
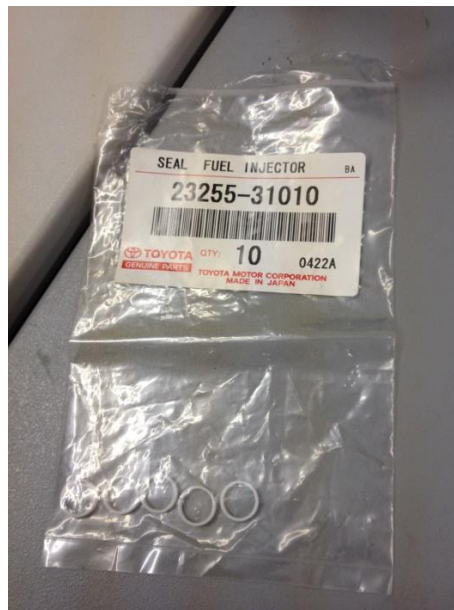
Figure 3-11: Toyota Denso injector seals

An alternative sealing solution was resolved by using Toyota Denso injector seals (Figure 3-11) with the outer and internal diameters taken into account for the fitment in the cylinder head. The fitting methods complied with the original manufacturers' guidelines for both injectors were also sought, as shown in Figure 3-12.

Figure 3-12: Manufacturers' fitting guidelines for multi-hole solenoid (top) and Piezo (bottom)

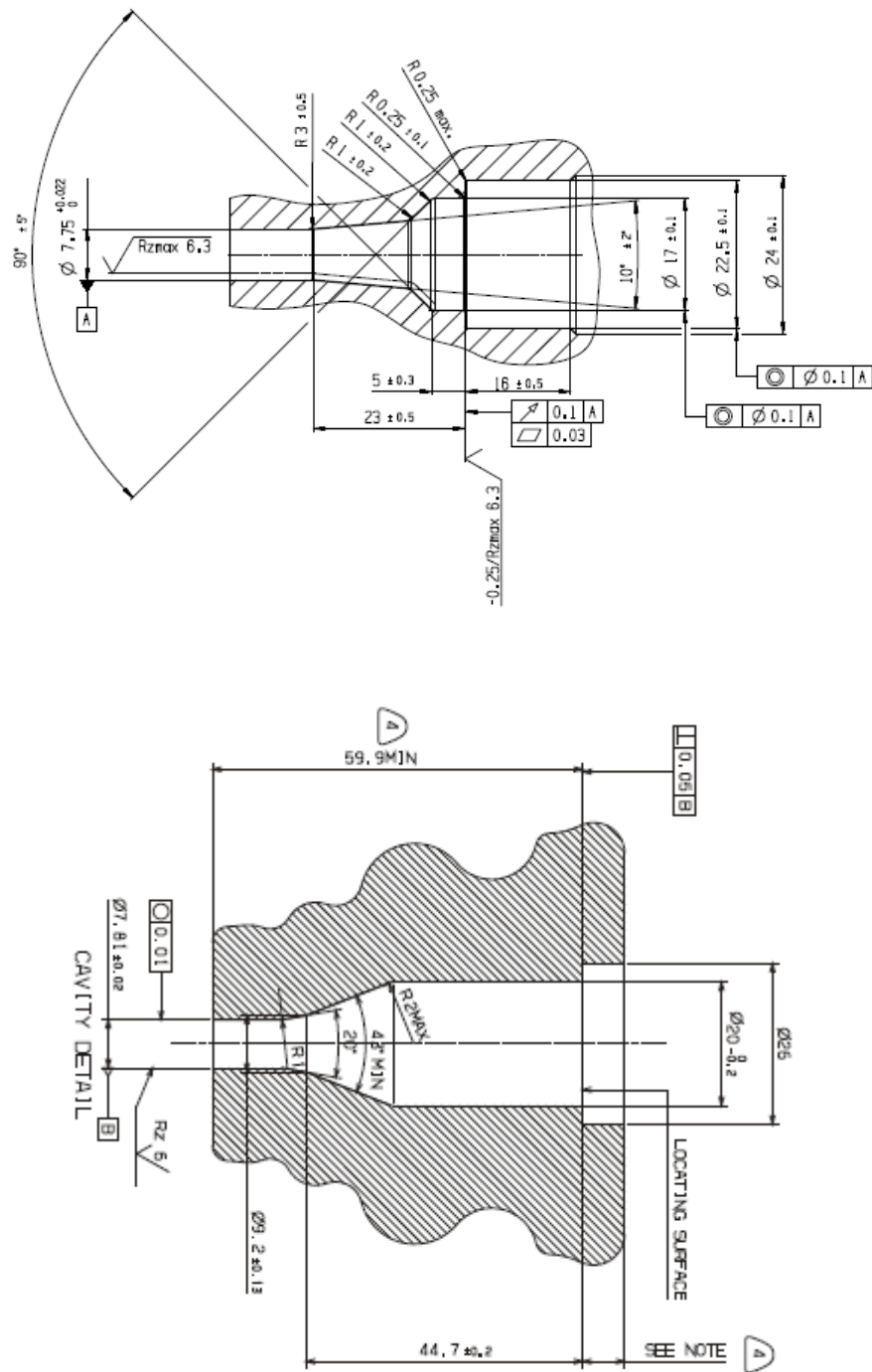A bespoke 11/32" (H7) hand reamer was modified to enlarge the existing diameter of the injector hole of 8mm to a new diameter of 8.75mm (±0.02) on the cylinder head according to the sleeve design discussed previously, as demonstrated in Figure 3-13.

Customised hand reamer
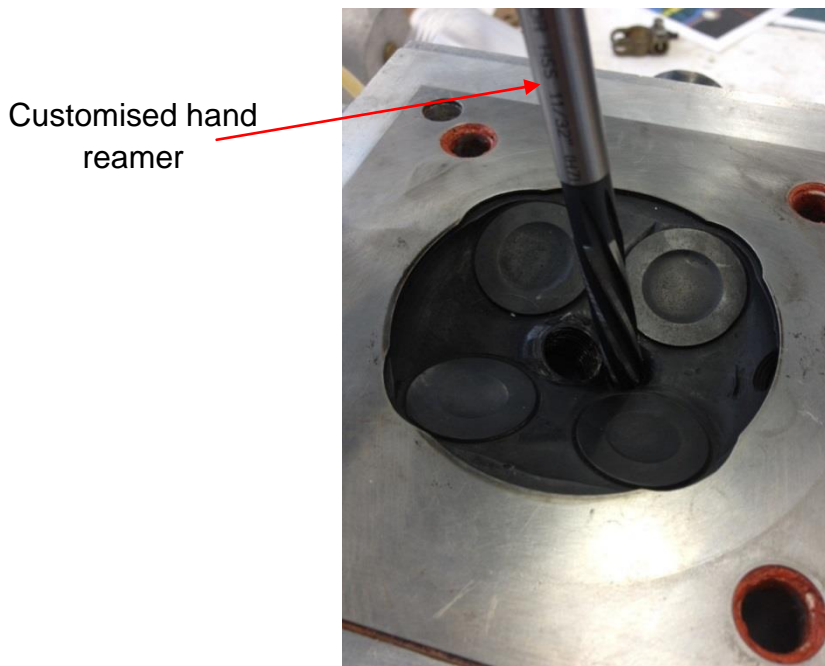
Figure 3-13: Cylinder head modifications with customised hand reamer

Following the moderate modifications to the cylinder head and injectors, new clamping methods for accommodating both injectors were sought and finalised. These methods were replicated by those used in the MAHLE DI3 engine assembly, which was previously developed by MAHLE in collaboration with the injector suppliers. Figure 3-14 shows the clamping method for the multi-hole injector intended for future use. This comprised of 6 parts as detailed in the CAD model:

- Top hat high pressure rail adaptor (Brown)
- Forked clamp (Yellow)
- Clamp spacer (Grey, fitted below the forked clamp)
- Clamp supporter (Blue block)
- Threaded bar (Green)
- Injector tip spacer (Green)
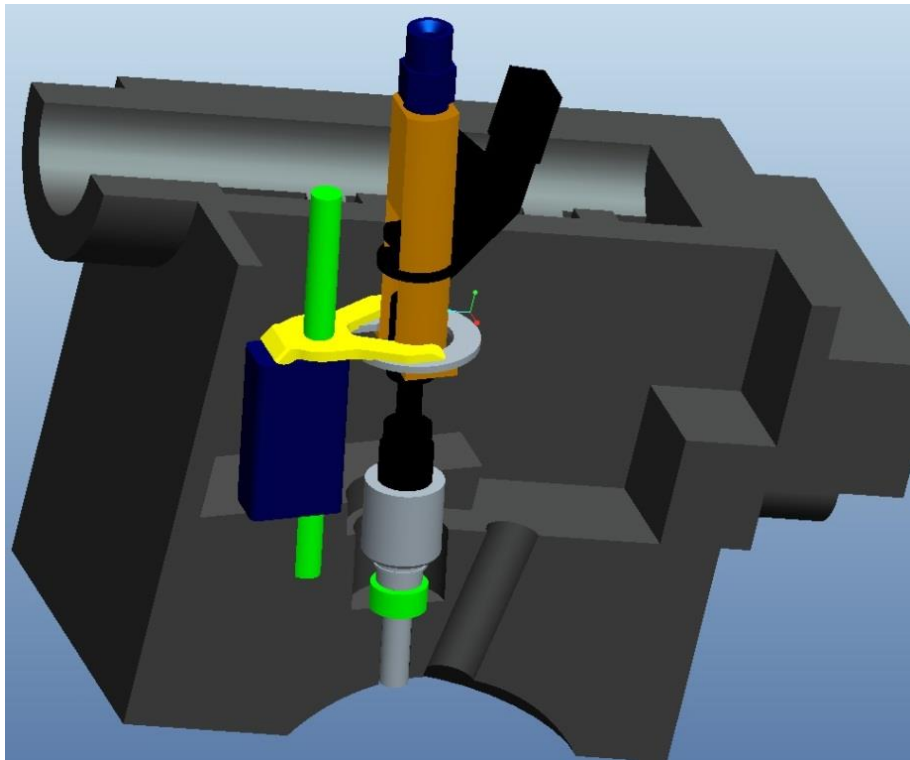
Figure 3-14: Clamping method for multi-hole injector

Set out in Figure 3-15 is the clamping method for the Piezo injector, which was used throughout the experiments with parts included as below. Shown in Figure 3-16 is the top view of the cylinder head.

- Forked clamp (Yellow)
- Clamp supporter (Blue block)
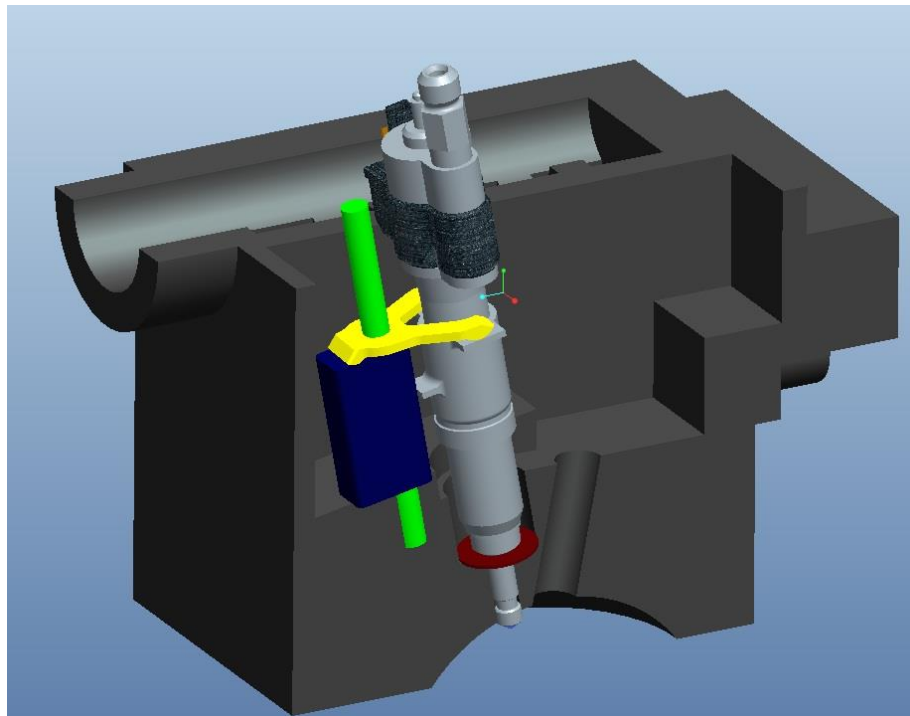- Threaded bar (Green)
- Injector tip washer (Red)

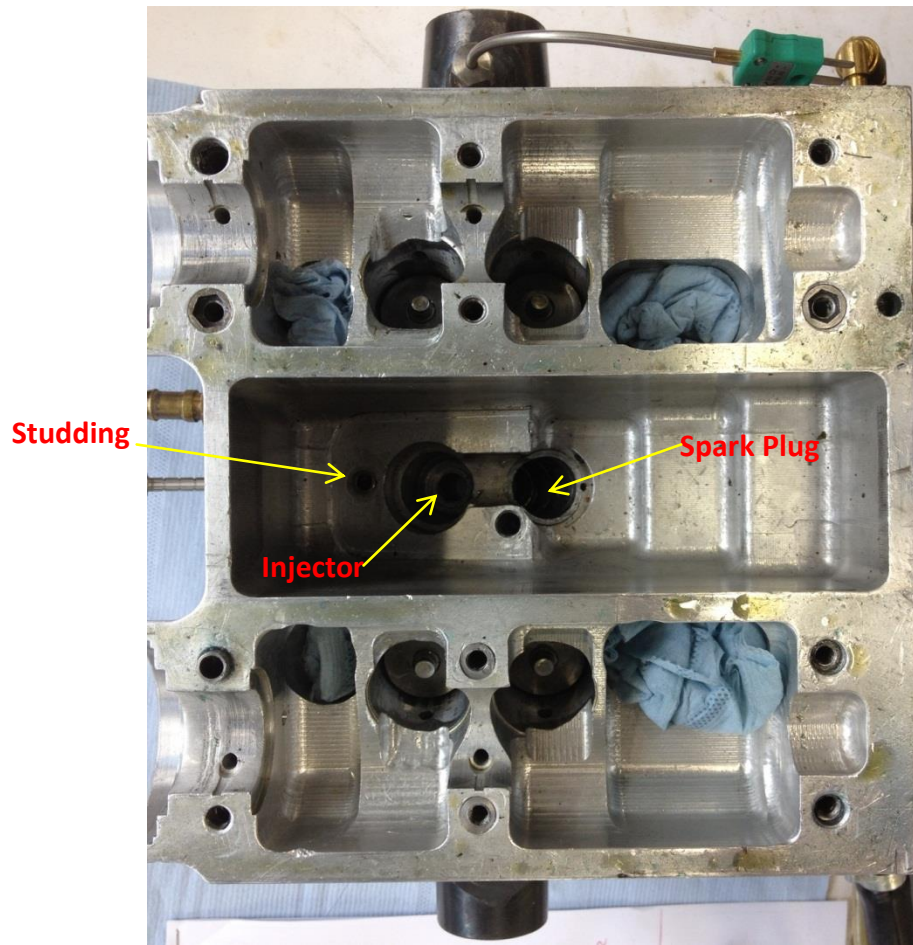

Figure 3-15: Clamping method for Piezo injector

Figure 3-16: Top view of the cylinder head

3.3 Fuel Preparation

The key properties of the fuels and dopant used are presented in Table 3-2. The two gasoline-ethanol blends were selected as potential "real" fuels for DISI engines. For both fuels a pump grade 95RON unleaded gasoline (ULG) was splash blended with the ethanol on a volumetric basis. Fuel containing 10% volume ethanol was of interest as such blends are now widely available in the US market and still being considered within the EU. The E85 type blend has also emerged in key markets and was required to provide information on the behaviour of a higher ethanol content fuel under DISI flex-fuelled conditions. Iso-octane was also used to establish a single component benchmark for comparisons with these real fuels.

Table 3-2: Key properties of the experimental fuels and dopant

	ULG	Iso-octane	E10	E85	3-Pentanone
Lower Heating Value (MJ/kg)	43.16	44.31	41.64	29.28	33.4
RON	95	100	98	108	-
MON	86	100	88	90	-
(R+M)/2	91	100	93	99	-
Density at 15°C (kg/dm^3)	0.74	0.69	0.75	0.78	0.81
H/C Ratio	1.891	2.25	1.945	2.769	2
O_2 (% weight)	0	0	3.35	29.5	18.6

Given its similar boiling behaviour to iso-octane, 3-Pentanone is a common and arguably highly suitable PLIF tracer for such work and was chosen to be the tracer used. For the fuel distribution visualisations, all fuels were doped with tracer (9:1 fuel to dopant in volume), premixed in the fuel tank and injected directly into the combustion chamber. For the in-cylinder temperature measurements, the tracer was injected (at 4.5mg/cycle) into the intake air via a port fuel injector mounted on the intake port.

3.4 Fuel and Fuel Dopant Supply System

The bespoke fuel supply system consisted of a PowerStar4 (S64 P4S64) double ended air driven pump with an amplification ratio of 64:1. With the regulated air inlet pressure at ~5.5bar this pump could generate rail pressures of up to ~340bar, which satisfied the test criteria being operating from 100 – 250bar and towards the intended burst pressure of 280bar for the Piezo injector. Figure 3-17 lays out the schematic of this bespoke fuel supply system accompanied with a view of the setup shown in Figure 3-18.
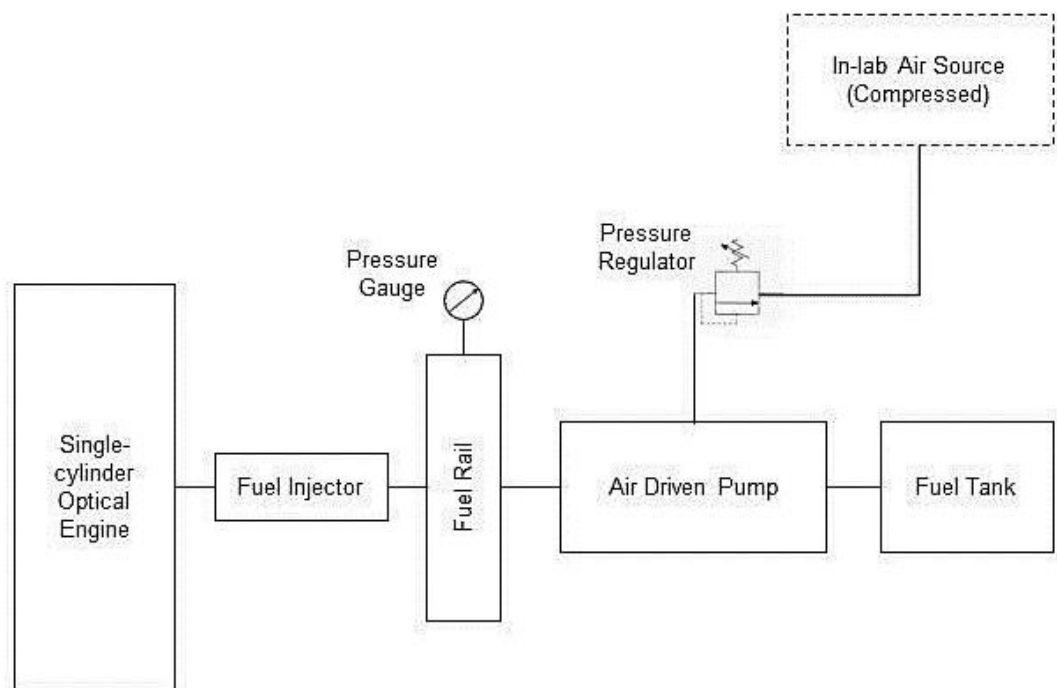

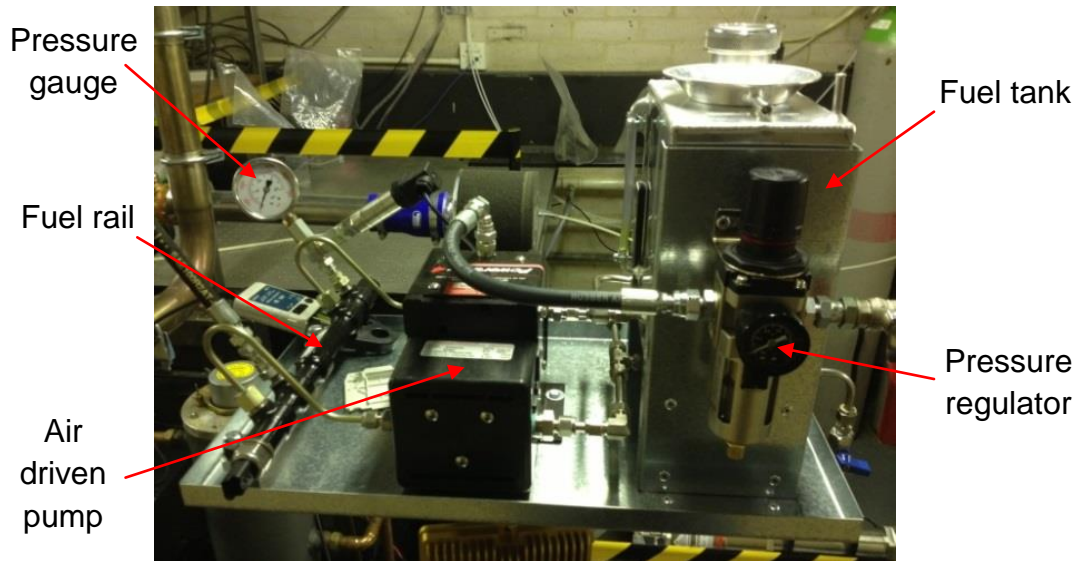Figure 3-17: Bespoke fuel supply system schematic

Figure 3-18: Bespoke fuel supply system

Figure 3-19 plots the performance curve for such double ended pump, with its operating characteristics including the relationship between inlet and out pressure with the losses taken into account as well as the corresponding flow rates shown.
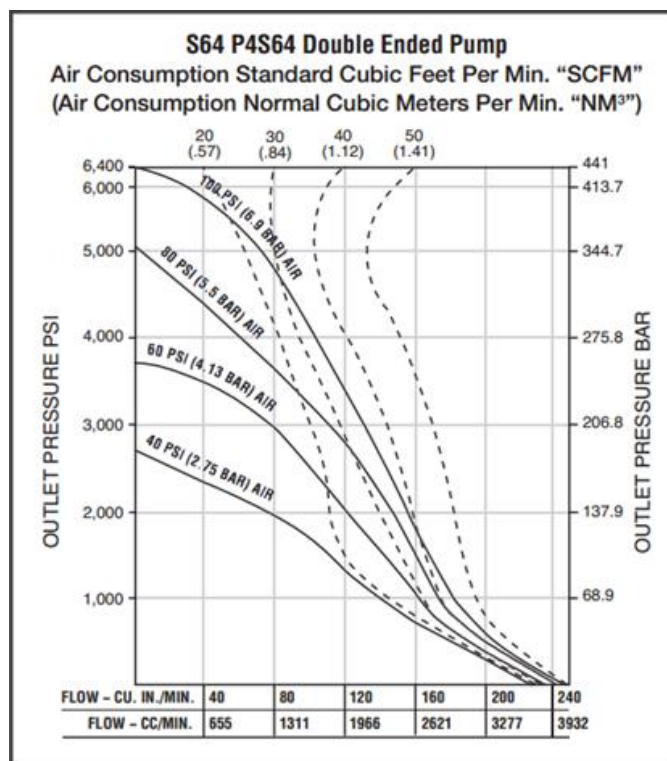

Figure 3-19: PowerStar4 S64 P4S64 performance curve

The pressure variation in the fuel rail was measured at ±4bar at 200bar fuel pressure with 0.5ms injection duration using iso-octane. This was completed by utilising a pre-calibrated pressure sensor (GE UNIK 5000) with a measuring range from 0 to 600bar (span range from 0 to 4.998V). Figure 3-20 shows a variation of 68mV in the output voltage signals from the pressure sensor, this correlates to ~8bar, therefore a ±4bar was obtained.
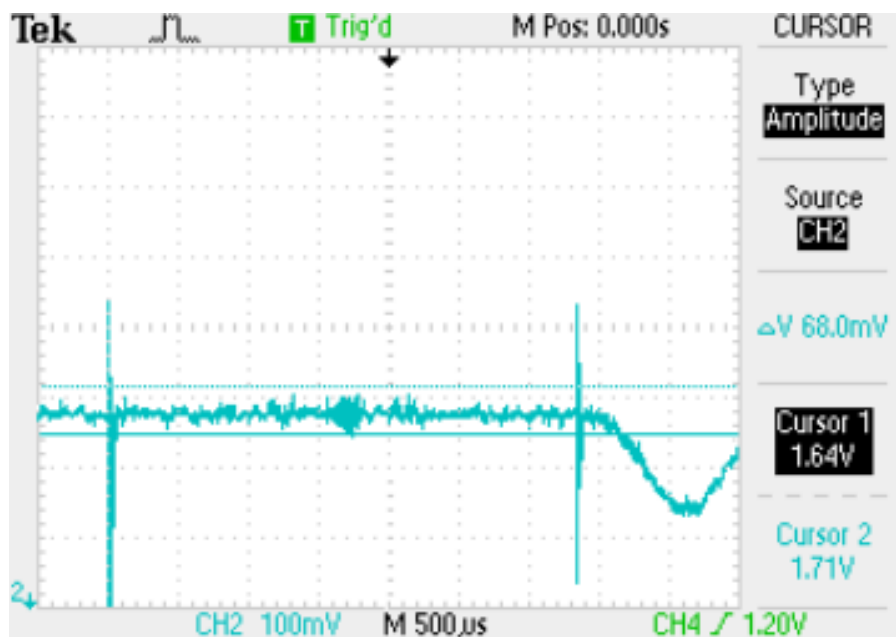
Figure 3-20: Pressure variation of the bespoke fuel supply system (rail measurement)

3.5 Data Acquisition System

3.5.1 In-cylinder Pressure Measurement

In-cylinder pressure has always been regarded as one of the most important parameters for characterising engine combustion. These pressure transducers are designed to measure the in-cylinder pressure dynamically in order that the rapid changing in-cylinder pressure trace can be found; therefore the data can be used for analysing the cycle-to-cycle variations as well as identifying any misfiring and knocking events among with any abnormal combustion. Furthermore, performance analysis including mean effective pressure, heat release analysis and etc. can be carried out. Instantaneous in-cylinder pressure data acquisition was utilised throughout the experiments, which required use of a

Kistler 6055B80 piezoelectric pressure transducer connected to a charge amplifier Kistler 568 via a high impedance cable. The charge output of the transducer is interpreted to the corresponding voltage readout within the amplifier; this analogue signal is then converted to a digital signal via an analogue-to-digital converter within the data acquisition system. This system is rated at ~250bar with a sensitivity of 19.4 pC/bar and uncertainty of +/-0.1%. To ensure the accuracy of the pressure sensor, a dead weight pressure gauge testing was performed for calibration purposes as discussed previously.

3.5.2 Data Acquisition Synchronisation

The data acquisition system used in the work consisted of a National Instruments board type NI USB-6251, a host computer and a LabView based program written previously at Brunel University. This program was capable of realtime data acquisition as well as some calculations including IMEP and COV of IMEP. The NI USB-6251 is a multifunction data acquisition card with 16-bits resolution and a sampling rate of 1.25 MS/s. It has 3 inputs which receive the pressure charge amplifier output signal, the engine clock signal and engine reference signal. The card was connected with a USB cable to the host computer which was used to store the data and perform the calculations for every test run.

A reference signal is required to synchronise the data acquisition system, laser diagnostic system and engine control units including direct injection fuel supply system and ignition system to the engine crank angle. This reference signal was provided by an And Gate Logic unit at 80° CA bTDC. This unit received a signal from a shaft encoder (clock signal) with 1° CA resolution and a signal from the hall-effect cam sensor. The hall-effect sensor was attached on the exhaust camshaft pulley and provided a signal for each cycle at 80° CA bTDC, as illustrated in Figure 3-21 below.
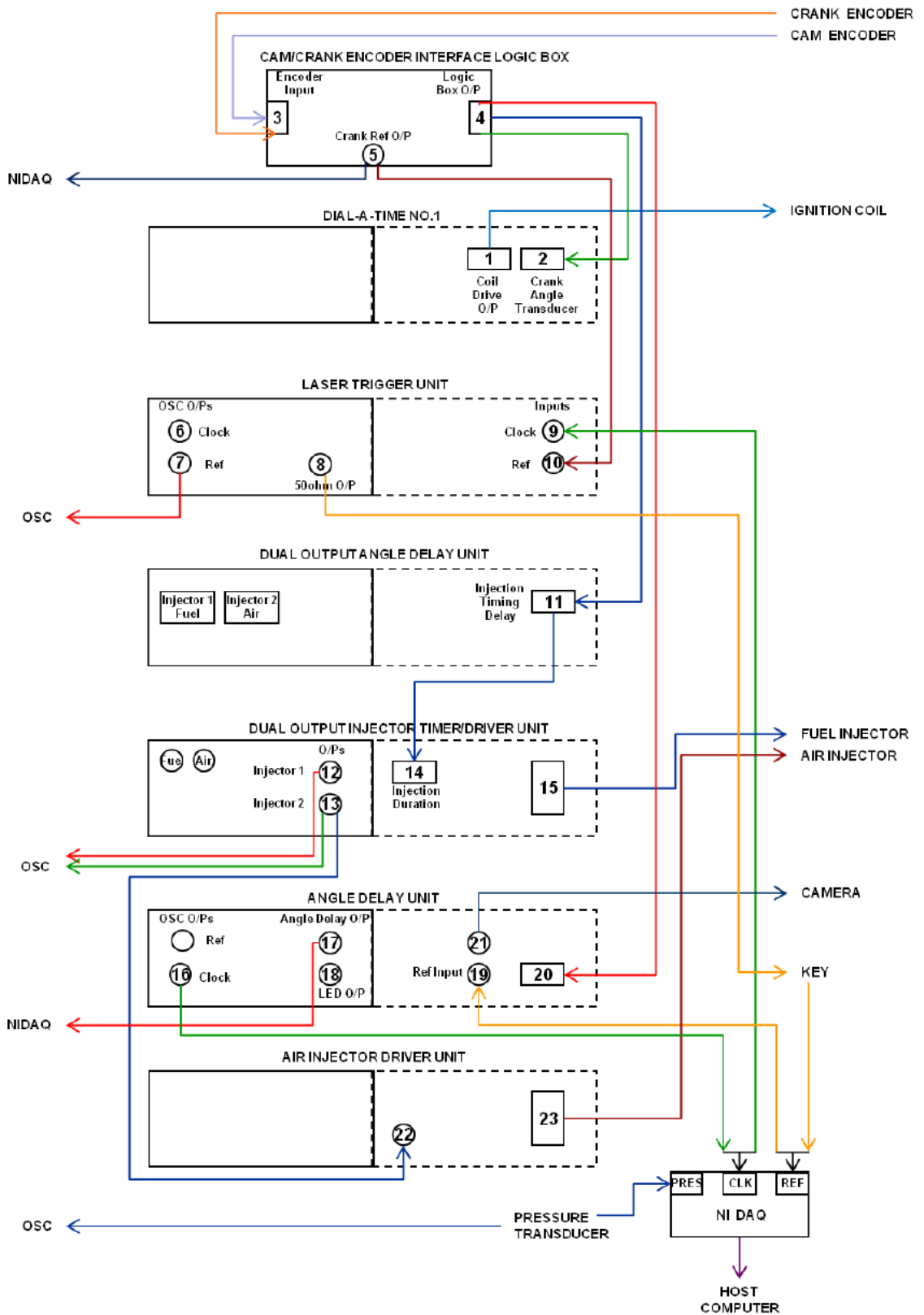
Figure 3-21: Data acquisition system [78]

3.6 PLIF Setup

Planar Laser Induced Fluorescence is a well-known diagnostic technique that allows the distribution of the fuel, residual burned gases and in-cylinder gas temperature to be qualified. In the current work this technique provided valuable information on the tendency for in-cylinder particulate emission formation due to stratification of the fuel and/or (to a lesser degree) differences in charge temperature. The PLIF system consisted of two lasers, a Raman converter, a dual-frame ICCD camera and the ancillary optics including mirrors, a prism, lenses and filters for steering, shaping and collecting the laser beams. The two excitation wavelengths of 308nm and 277nm were generated by a XeCl Excimer laser (Lambda Physik COMPexPro 102) and via Raman shifting of a 248nm KrF Excimer laser (Coherent COMPex 102) respectively, as illustrated in Figure 3-22.

The Raman converter was of custom made for this work, measuring 60cm in length (internal volume of 1.3 litre) with a large aperture size of 1 inch accompanied with an internal recirculation system, and was operated at a total pressure of 55bar (800psi) filled with Grade 5 Hydrogen (BOC Special Gases, purity at 99.999%). Two Lithosil lenses with focal length of 33.3cm (nominal) with a thickness of 15.8mm (5/8 inch) were used to focus and re-collimate the laser beam. The 277nm pulse was generated by Raman shifting the 248nm KrF Excimer laser to the first Stokes wavelength in H_2 with an energy conversion efficiency of 12 – 15% measured by prior worker at Brunel [78].
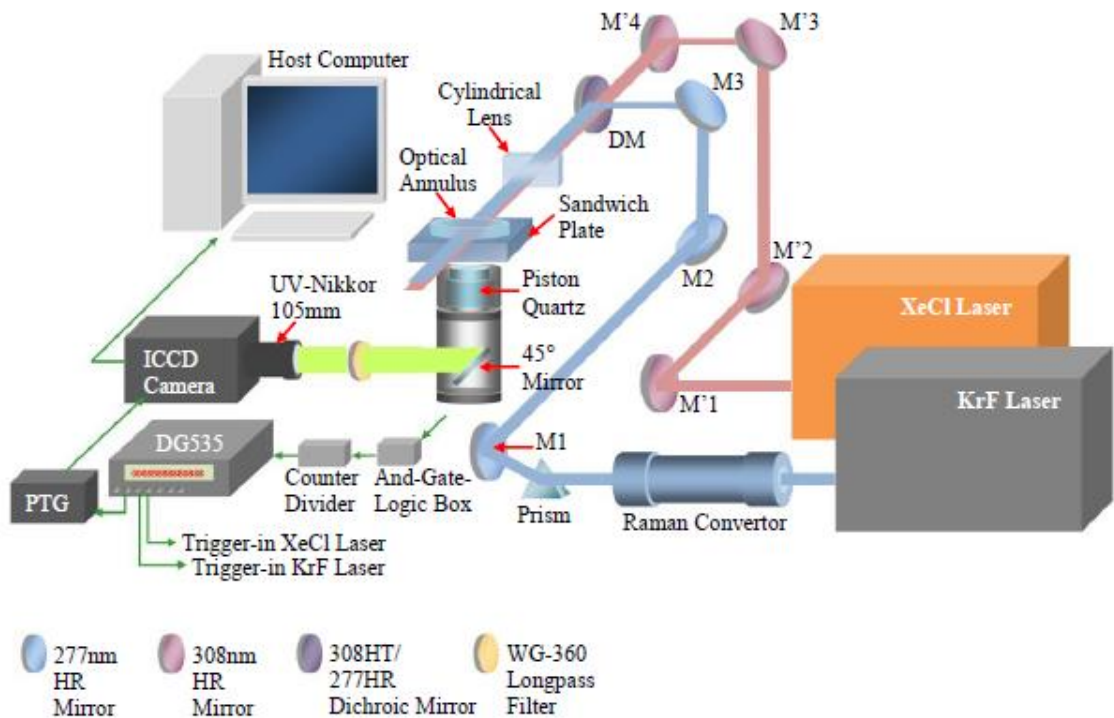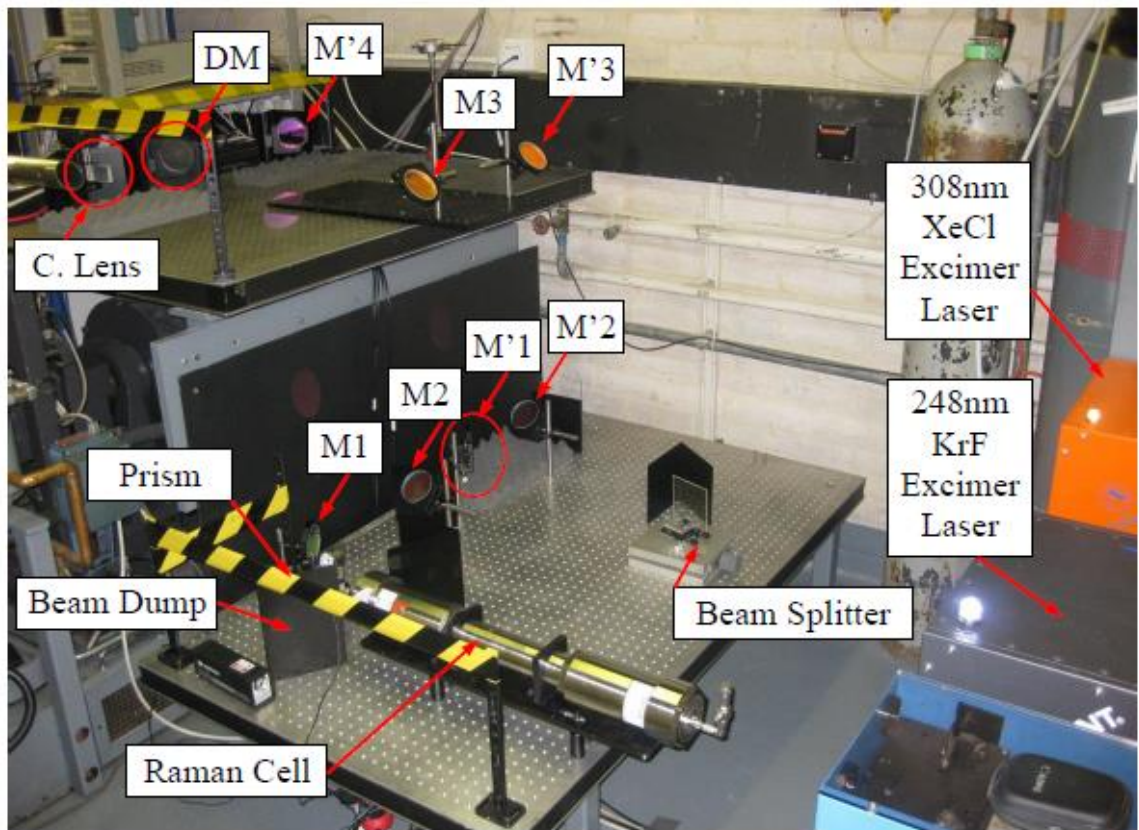
Figure 3-22: Beam delivery and shaping system setup (top) and PLIF system schematic (bottom) [78]

The in-cylinder temperature measurements via the tracer based PLIF technique can be summarised in two basic steps. Firstly, by capturing images from rapidly triggered successive two-line excitation pulses the ratio of the two fluorescence signals can be cross-referred to temperature. Secondly, by adopting two different tracers and a single excitation pulse the ratio of the fluorescence signals may also be analysed to indicate temperature. In recent work such a technique was adopted by Rothamer et al. [81] who indicated a high accuracy of ±5% for in-cylinder temperature measurement when compared to 1-D engine simulation results.

The two-line PLIF technique requires two precise spatially overlapping laser sheets to illuminate the targeted plane in the combustion chamber. The output beam generated by the XeCl laser went through a beam splitter while the KrF laser beam was sent through the Raman converter and passed through a dispersive prism. Both laser beams were then redirected by highly reflective mirrors, combined using a dichroic mirror and finally focused by a cylindrical lens. The dichroic mirror was a key component that allowed spatial overlap of the two laser beams, while the special coating helped transmit the 308nm (>90% efficiency) and reflect the 277nm wavelengths (>97% efficiency). Both Excimer laser beam divergences were measured at 9mrad and 1mrad for the vertical and horizontal axes respectively using a pulse energy meter and a knife-edge technique. The laser sheets (55mm wide and ~0.5mm thick) were transmitted through the side optical window with high divergence in the horizontal axes and low divergence in the vertical axes to maximise the homogeneous illumination coverage over the targeted plane. The pulse energies of the 308nm and 277nm lasers were 40mJ and 20mJ respectively, with typical shot-to-shot pulse energy variation kept below 2% (308nm) and 1% (277nm) throughout the experiments (a pulse energy meter was used to monitor and record prior to each test, samples can be found in Figure 3-23 and Figure 3-24 below).
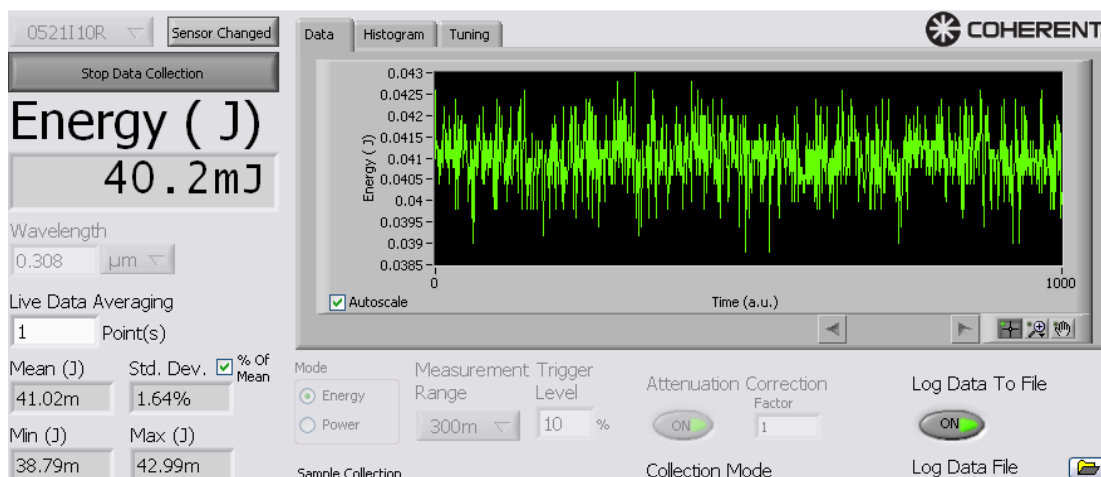
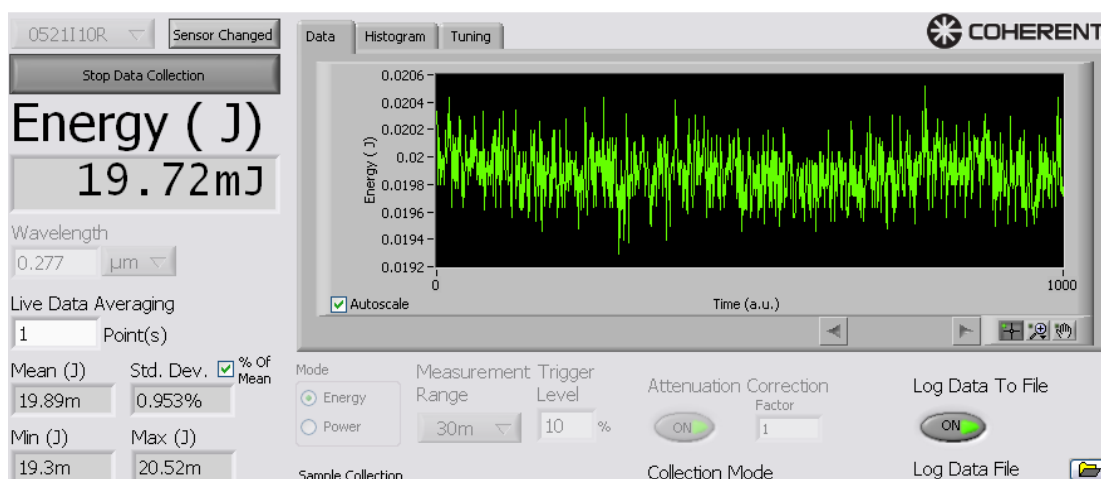**Figure 3-23: Laser pulse energy variation of XeCl (308nm)**

Figure 3-24: Laser pulse energy variation of KrF (277nm)

The imaging system included a Princeton Instrument PI-MAX III ICCD camera that provided a low noise and high dynamic range. The readouts could be scanned at a variety of pixel rates. When carrying out two-line PLIF Double Image Frames (DIF), the overlapped operation allowed a new exposure to begin while the existing one was still in progress. Thus overall the system was capable of capturing two images in very rapid succession. A Nikkor UV 105mm f/4.5 lens and a Schott WG-360 long-pass filter were used to collect the fluorescence signal and block the unwanted wavelengths. The camera and lasers were synchronised to the engine via a crankshaft encoder. A counter/divider was used to provide the camera and laser trigger-in signals. The camera Programmable Timing Generator (PTG) and DG535 delay generator were used to set the delays

between the lasers and the camera trigger-in signals (with a maximum total system delay of 77ns recorded).

Chapter 4 Optical Measurements and Analysis

4.1 Background to the Optical Measurements

4.1.1 Physical Probes vs. Laser Diagnostic Techniques

The combustion process in an internal combustion engine involves a finite but relatively rapid heat release process with high pressure and temperature, specifically involving complex physical and chemical events with high cyclic variations between these events. Even today, the harsh conditions and fast timescales limit what combustion diagnostic measurements can be made using physical probes. Typical prior efforts have included velocity field measurements via hot wires, with multiple wires sometimes adopted in an attempt to additionally quantify direction. Recently, extremely thin hot wires have also been used in an attempt to capture dynamic motoring gas temperatures and associated differences in charge cooling effects with alcohol fuels [82]. However, the excessive temperatures during combustion still inhibit any measurements in the presence of burned gases, which may reach peak temperatures in excess of 2200K. As a result, over the last four decades or so there have been considerable efforts to develop non-intrusive laser diagnostic techniques, with multiple variants now available to characterise the in-cylinder flow, direct fuel injection process (and associated interactions), combustion imaging (flame propagation in SI engines) and gas temperature profiles. Such experimental techniques have proven invaluable in characterising the complex interactions, allowing predictive models to be developed to help reduce engine development times. Nonetheless, the combustion process in SI or diesel engines is far from being fully understood and capturing evidence of new phenomena remains limited by laser frequencies and both temporal and spatial resolutions of the data acquisition.

The term LASER is an acronym (Light Amplification by Stimulated Emission of Radiation) and when adopted for combustion characterisation often involves some form of scattering of the light, followed by high speed optical detection and/or imaging at an incident. Rayleigh scattering is an elastic process, so that

the scattered signal occurs at the same wavelength as the excitation source. For this reason, the Rayleigh signal is subject to interference from the intense scattered light produced by particles and nearby surfaces. Also being an elastic process, Rayleigh scattering is not species specific and involves the elastic scattering of light or other electromagnetic radiation by particles much smaller than the wavelength of the radiation. Rayleigh scattering does not change the state of material and is, hence, a parametric process. The process involves interference from scattered light from particles and surfaces in the relative region [83].

Raman scattering is an inelastic process in which the oscillating polarizability of the molecule modulates the scattered radiation, thereby leading to the appearance of two sideband frequencies. If a molecule gains energy from the radiative field, the resulting lower frequency scattered radiation is termed the Stokes component. If the molecule loses energy to the radiative field, the scattered radiation is referred to as the anti -Stokes component [83], [84].

To summarise, Raman scattering is:

- Inelastic, with oscillating polarizability
- Emitting a signal wavelength that is different from excitation source.

One key difference from Rayleigh and Raman scattering, for fluorescence, is that a precise excitation frequency is required. Fluorescence is the emission of light by a substance that has absorbed light or other electromagnetic radiation. It is a form of luminescence. In most cases, the emitted light has a longer wavelength, and therefore lower energy, than the absorbed radiation. Since molecules in a particular rovibronic level of the ground electronic state must be excited to a specific rovibronic level in another electronic state. Spontaneous emission can then be monitored from the upper rovibronic level to a variety of such levels in the ground electronic state. Fluorescence can also occur from indirectly excited levels in the upper electronic state owing to collisional dynamics, i.e., rotational and vibrational relaxation [83]. Figure 4-1 shows an energy level diagram for Rayleigh scattering, vibrational and rotational Raman scattering and laser induced fluorescence scattering methods.
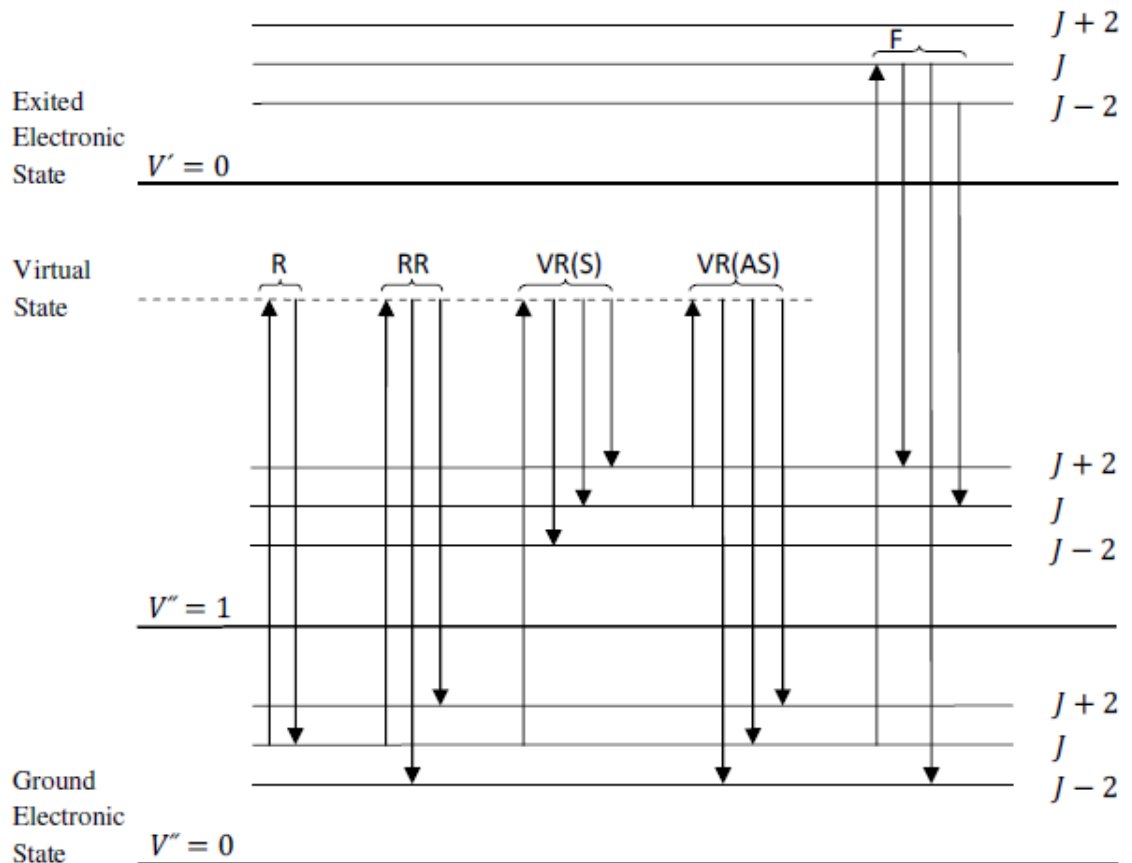
Figure 4-1: Energy level diagram - Rayleigh (R), Rotational Raman (RR), Vibrational Raman (VR), and Fluorescence (F) scattering methods [83]

4.1.2 Thermometry by Excitation or Fluorescence Scans

Slow excitation of fluorescence has been used for laminar flow systems to determine the rotational temperature of the subjects. Instead of taking a line-of-sight temperature, this technique measures local temperature directly. The spectral bandwidth of the detector is fixed for excitation scans. In contrast, the excitation frequency is fixed for fluorescence scans. In both cases an accurate temperature requires that the fluorescence spectrum be uncontaminated by self-absorption. For the excitation case, optically thin conditions are also needed to avoid variations in laser beam absorptivity with changes in excitation wavelength [85], [86]. Such techniques are commonly applied for steady flame studies, for engine applications, these techniques are very hard to be applied.

Two-line fluorescence thermometry has been developed to tackle the difficulties for excitation and fluorescence scans due to its slow response, so the technique applications can be extended to turbulent flame cases.

4.1.3　Thermometry by Single-line Fluorescence

Thermally Assisted Fluorescence (THAF) is known as the most straightforward monochromatic method. In this technique, the laser induced populations are equilibrated, so that an electronic, vibrational or rotational temperature can be extracted from the resulting fluorescence spectrum [87].

Another monochromatic method named Absolute Fluorescence Method (ABF), which relies on the inherent temperature dependence of the fluorescence signal, and requires the mole fraction of the absorbing species, χs, to be constant, thus best results are to be obtained for non-reactive flows [88].

4.1.4　Thermometry by Two-line Fluorescence

Two-line fluorescence thermometry has been developed to tackle the difficulties for excitation and fluorescence scans due to its slow response, so the technique applications can be extended to turbulent flame cases. By introducing a pair of laser shots with different wavelengths, two fluorescence signals are generated. The TLAF (Two-line Atomic Fluorescence) thermometry can be achieved at much lower laser power than TLMF (Two-line Molecular Fluorescence) thermometry as the atomic species have much higher oscillator strength. However, measurements at temperatures below 500 K are not feasible due to low vapour pressure of atomic seeds. Kaminski et al. demonstrated temporally resolved TLAF thermometry in a SI engine using indium as an atomic additive for a temperature range of 800 to 2800 K. A precision of 14% on single-shot temperature distributions was claimed [89], [90].

4.1.5　Choice of Tracer

For the reason discussed previously, Laser Induced Fluorescence (LIF) is a technique suitable for in-cylinder fuelling and combustion investigations in internal combustion engines. Furthermore, two-line Planar Laser Induced Fluorescence (2-line PLIF) is capable of taking temperature measurements accurately with careful experimental design. Many studies of fuels and tracers for use with PLIF have been reported. Fluorescence from combustion intermediates such as the OH radical [91], [92], commercial-grade gasoline or even iso-octane

without tracer has been used [93], [94]. However, the use of gasoline has some drawbacks and also the use of iso-octane without any tracer limits the capabilities of the PLIF technique.

The resulting quality of LIF is highly dependent on the choice of tracer. In this work, iso-octane was used as the base fuel. Finding a proper tracer species and the ideal ratio between tracer and base fuel was therefore crucial.

Toluene, acetone and 3-pentanone are the most commonly used tracer candidates when iso-octane is adopted. Oxygen quenching is the major restriction of the usage of toluene (aromatic tracer), when comparing with a ketone tracer like acetone and 3-pentenone. However, its nature of high sensitivity to oxygen is ideal for fuel-air ratio measurements in engines. This significant finding was first reported by Reboux [95]. Also toluene's prevalence in a variety of fuels (e.g. as an octane booster) and fuel surrogates (as a single high octane element e.g. TRF blends) makes it a suitable candidate for a range of combustion-related mixing applications. Acetone was first recommended by Lozano et al. [96], [97] for non-reactive gas phase mixing applications because it is safe, cheap, easy to handle and it also has the following characteristics [98], [99], [100], [101], [102], [103]. Acetone is attractive for a variety of reasons including:

- High vapour pressure, which is desirable for seeding into the gas phase
- Broad absorption spectrum where high-power lasers are available
- Strong, non-resonant fluorescence spectrum in near-UV/visible where detector quantum efficiencies are high
- Short fluorescence lifetime which enables measurements of fast flows without blurring effects
- High resistance to collisional quenching or bath gas effects.

These properties made acetone PLIF one of the popular laser diagnostics for studying basic fluid mechanics and a variety of other engineering applications. However it was soon realized that acetone is not the ideal tracer for all applications. This was mainly due to the fact that it has a different mixing rate compared to iso-octane (the main surrogate fuel for gasoline due to similar calorific and burn rate properties). Iso-octane is a much heavier compound than

acetone and therefore it tends to remain in the liquid phase much longer than acetone. As a result acetone PLIF measurements could not present for example fuel concentration.

According to the discussed work above, acetone is a very popular candidate for LIF engine study applications. However, due to the physical property difference between acetone and iso-octane, a representative mixture is hard to be made since iso-octane is heavier so that it will remain in a liquid phase for a longer time than acetone. This makes acetone incapable of taking fuel concentration measurements.

3-pentanone was the next ketone proposed by many researchers for PLIF measurements in IC engines. The first use of 3-pentanone as a tracer in IC engine was demonstrated by Arnold et al. [104], they used a high purity iso-octane as the baseline fuel doped with 6% 3-pentanone for measurements of relative fuel concentration fields to study the fuel intake, start and propagation of the combustion, where a two-line PLIF technique (combination of a tuneable excimer laser at 248 nm and a broadband excimer laser at 308 nm) was utilised to characterise the performance of a 4 cylinder 16-valve SI engine. Berckmüller et al. [105] developed a single-line (XeCl excimer laser at 308 nm) PLIF technique using 3-pentanone for imaging the in-cylinder fuel concentration to study the charge stratification in a lean burn SI engine. They applied this technique to a firing optical-accessed single cylinder SI engine. Instantaneous planar fuel distributions at different crank angles in the inlet and compression stroke have been obtained. A series of such images provides a picture of the overall fuel motion within the cylinder.

3-pentanone has many of the same attractive photo-physical characteristics as acetone but it is heavier in molecular weight. The higher boiling point of 3-pentanone (102 °C) which is very comparable to iso-octane's (99 °C), this has made it arguably more suitable for PLIF measurements in SI engines. For heavier fuels such as diesel and jet fuels with boiling point at around 200 °C, higher aliphatic ketones such as heptanone and nonanone are the obvious candidates. The physical and thermodynamic properties of the most frequently used organic tracer molecules in comparison to iso-octane are illustrated in Table 4-1.

Table 4-1: Physical and thermodynamic properties of iso-octane, toluene, acetone and 3-pentanone [106]

Property	iso-octane	Toluene	Acetone	3-Pentanone
Molecular weight (g/mol)	114.2	92.1	58.1	86.1
Density at 25 °C (g/cm^3)	0.69	0.87	0.79	0.81
Boiling point (°C)	99.2	110.6	56.1	102.0
Heat of vaporization at 25 °C (kJ/mol)	35.1	38.0	31.0	38.5
Heat of combustion (MJ/mol)	5.50	3.95	1.82	3.14
Max. burning velocity at 25 °C and ϕ =(cm/s)	41.0 at 0.98	–	44.4 at 0.93	–
Flash point (°C)	-12 to 22	4.5-7	-18	7
Autoignition temperature in air (°C)	415-561	480-810	465-727	425-608
Flammability limits in 1 bar air (% vol)	0.95-6.5	1.2-7.1	2.6-13	1.6-8
Gas-phase viscosity at 100 °C (µPa s)	7.7	8.8	9.5	8.2
Gas-phase diffusion coeff. (1 bar air, 100 °C) (cm^2 s^{-1})	0.102	0.132	0.166	0.129
Gas-phase diffusion coeff. (8 bar air, 130 °C) (cm^2 s^{-1})	0.0148	0.0190	0.0239	0.0187
Octane number (RON/MON)	100/100	111/95	–	–
Heating Value (LHV) (MJ/kg)	44.31	40.58	28.55	–

4.1.6 Two-line PLIF Measurements

Grossmann and co-workers [107] studied the temperature and pressure dependences of the LIF signal of both gas-phase acetone and 3-pentanone. They showed for the first time that after excitation at two different wavelengths, a combination of KrF excimer laser at 248 nm and 277 or 312 nm radiations which were obtained by Raman shifting the KrF excimer wavelength to the first and second Stokes lines of H_2 respectively, the ratio of the fluorescence signal intensities correlated with the local temperature. Since this temperature

measurement is based on the ratio of signal intensities, it is independent of local tracer concentrations and therefore allows measurements of 2D-temperature distributions in non-homogeneously mixed systems. They compared the PLIF calculated temperature values with thermocouple readings and reported a satisfactory precision up to 550 K. However at higher temperatures the calculated values tended to underestimate the thermocouple readings by 50 K at around 600 K. They suggested that the deviation at higher temperatures may be due to uncertainties of the calibration curve.

The first application of the two-line PLIF technique for temperature distribution measurements in a SI engine was demonstrated by Einecke et al. [108]. The measurements were carried out in an optically accessible two-stroke engine fuelled with iso-octane and doped with 3-pentanone. Temperature distribution fields were obtained for both the compression stroke and the power stroke (from unburned gases). The use of two different excitation wavelengths, 308 nm and 248 nm from XeCl and KrF excimer lasers respectively simplified the otherwise complicated relation between LIF signal intensity and system parameters. This work was continued by measurements of the absolute concentration and the fuel/air equivalence ratios. Instantaneous temperature distribution fields obtained from the two-line PLIF technique were used to evaluate fuel distributions quantitatively in terms of number densities and fuel/air equivalence ratio. The measurements were performed at an engine speed of 1000 rpm and overall fuel/air equivalence ratio of Ø0.62. The low equivalence ratio was chosen as it leads to a very slow combustion and thus produces small pressure increase compared to the motoring test. This was necessary to ensure some of the tracer was left for temperature measurements during the late compression stroke. They reported ±25 K uncertainty for temperature measurements of up to 600K [109].

Researchers at the University of Wisconsin Madison exploited the PLIF technique using 3-pentanone and Hydroxyl radicals (OH) for flame structure visualisation of stratified combustion in an optically accessible DISI engine under both stratified and homogeneous operating conditions. OH radicals were used to illustrate the location of the burned gases, where 3-pentanone was used to show the location of unburned fuel. By capturing during the expansion stroke long after the major heat release, lean flame quenching was directly observed by the presence of 3-pentanone in the end gas [110].

Kakuho et al. [111] experimentally investigated the relation between in-cylinder mixture temperature distribution and auto-ignition in HCCI combustion. In this report two types of fluorescent tracers, 3-pentanone and triethylamime (TEA), were used with one excitation light source of frequency-quadrupled YAG laser at 266 nm. The results of this study showed that stratifying the in-cylinder temperature distribution could be an effective way of controlling HCCI combustion, albeit how this might be controlled in practical automotive IC engines remains highly questionable.

Rothamer et al. [81] recently carried out the work on optimising laser excitation wavelengths for two-line PLIF of 3-pentanone for simultaneous imaging of temperature and composition in a HCCI engine. They exploited two-line PLIF with a single tracer and a single interline ICCD camera. By comparing the experimental average temperatures and the values computed assuming isentropic compression, and they indicated an absolute accuracy of the temperature measurements of ± 5% when compared to 1-D engine simulation results. The diagnostic was tested during fired HCCI operation and was used to investigate the mixing of hot EGR with fresh intake charge [81], [112]. This work had then been followed on in a similar way to study the Negative Valve Overlap (NVO) strategy in HCCI engine operation. Snyder and co-workers employed single-line and two-line PLIF technique with 3-pentanone to study the distribution and evolution of naturally occurring Thermal Stratification (TS) in a HCCI engine under fired and motored operation. The two-line diagnostic was first applied during intake and early compression to provide simultaneous temperature and air mole fraction measurements. Subsequent single-line temperature measurements characterised the thermal stratification development during the latter part of the compression stroke. PLIF images were used to investigate the similarities and differences in the development of temperature stratification between motored and fired operation and to investigate the impact of direct fuel injection and cylinder wall temperature on TS [113], [114], [115], [116].

4.2 Planar Fuel Distribution Visualisation Processing

The output images of the fuel distributions were saved in one file for each different fuel used. WinView 32 data acquisition software was employed to process the large amount of data. The image processing procedure is illustrated in Figure 4-2. By averaging the background images, then subtracting these from the DI (fuel & tracer) images at different test points the variation in background laser light intensity throughout the imaging area was appropriately taken into account.
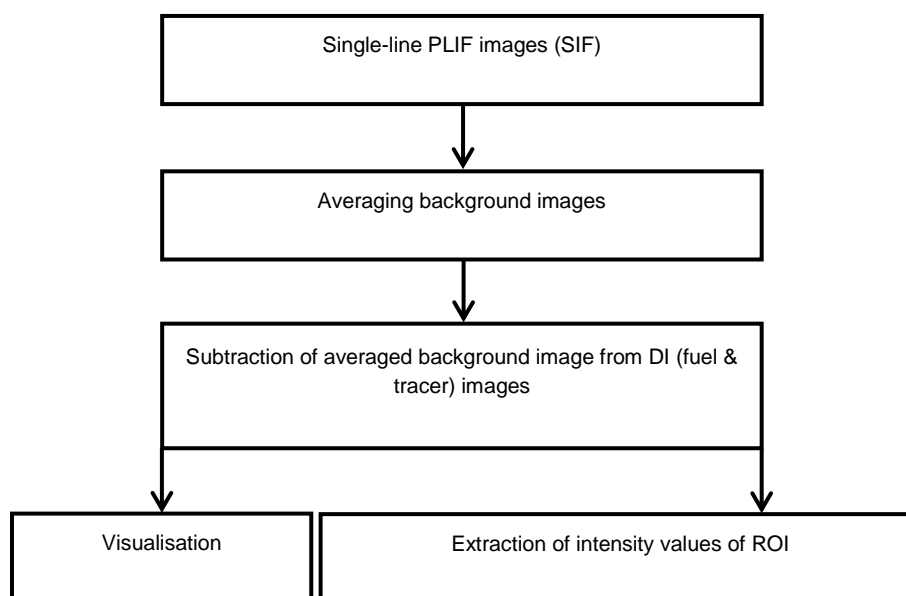
Figure 4-2: Image processing procedure for Planar Fuel Distribution Visualisations

4.3 Planar Gas Temperature Measurements

In the currently reported thesis, a calibration curve was used to quantify the degree of charge cooling with iso-octane at varied conditions. Although the relationship between the fluorescence signal intensity ratio of two beams and the temperature of the sampling area can be determined via theoretical models developed for fluorescence quantum yield and absorption cross section of the tracer, it was found that further validations and adjustments are usually needed [78]. Therefore in recent alternative work at Brunel on the same engine, a Constant Volume Chamber (CVC) was developed to replicate the 'real' engine motoring condition for an experimentally based calibration. The CVC was used

as a steady state calibration device (without any piston motion), being primed and sealed with gas containing the same proportion of tracer as used in the currents tests. In addition, the top of the CVC was mounted and sealed with the same optical cylinder head to ensure the consistency in light transmission efficiency. The CVC had a working pressure of up to 3bar and temperature up to 850K (imposed by the melting point of the material used). A combination of cartridge heaters and tubular heaters were attached to the CVC thus the temperature could be specified. A tracer supply system was designed to feed a homogenous mixture of both tracer and air via an inlet and outlet valve on the chamber. Two-line PLIF images were captured from room temperature up to 750K in 10K increments under a constant atmospheric pressure as reported elsewhere [78]. Shown in Figure 4-3 are the calibration results, where the red and blue data points represent the fluorescence signal intensity as a function of CVC temperature for both lasers. The temperature calibration curve was obtained by calculating the signal intensity ratio at each data point, with the fitted trend line shown superimposed.
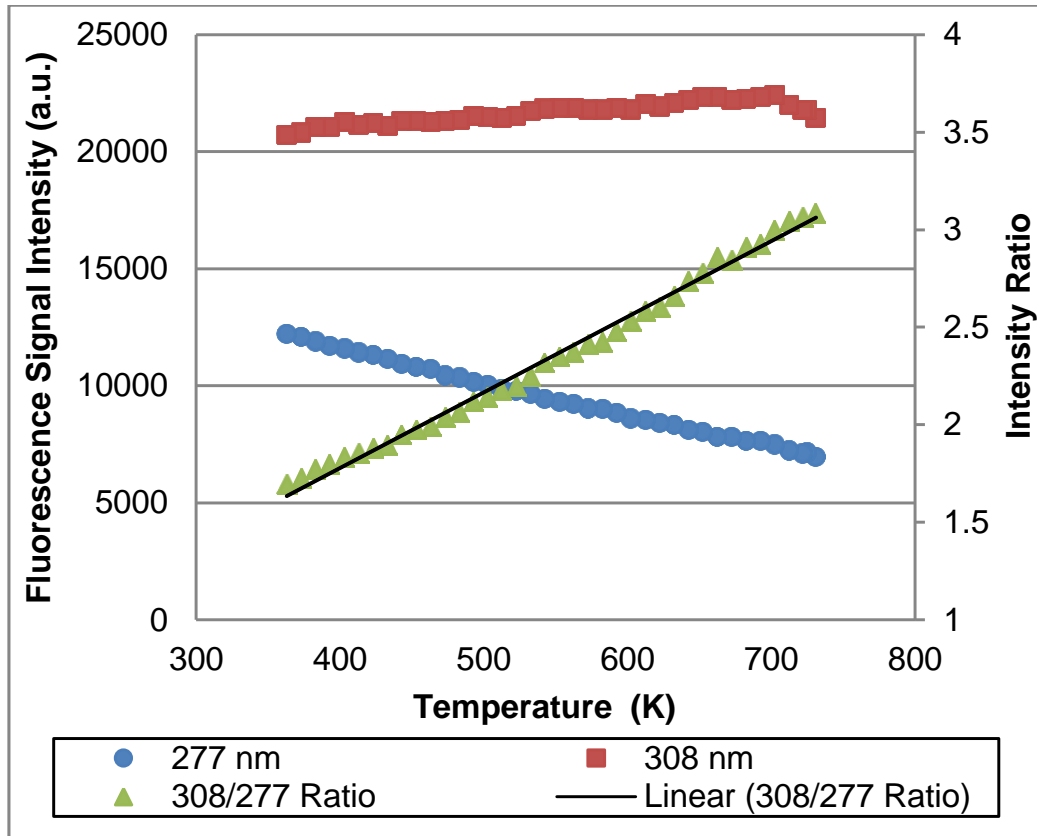
Figure 4-3: Two-line PLIF CVC calibration [78]

In previous work at Brunel [78], validation measurements were also performed in the same engine by comparing the calculated temperature from in-cylinder pressure data with the PLIF temperature calibration results, under similar motoring and firing conditions to those employed here. The results are illustrated in Figure 4-4. When using pressure data the perfect gas law was used in conjunction with air & fuel flow and gas temperature measurements in the ports. For the motoring case, the average percentage difference between the two methods was 3.53% with a standard deviation of 2.37%, while for the firing test the average percentage difference was found to be 2% with a standard deviation of 1.28%. Overall, from this prior work, it was concluded here that the PLIF calibration technique was acceptable for the current tests given identical tracer concentration would be used at similar engine conditions.
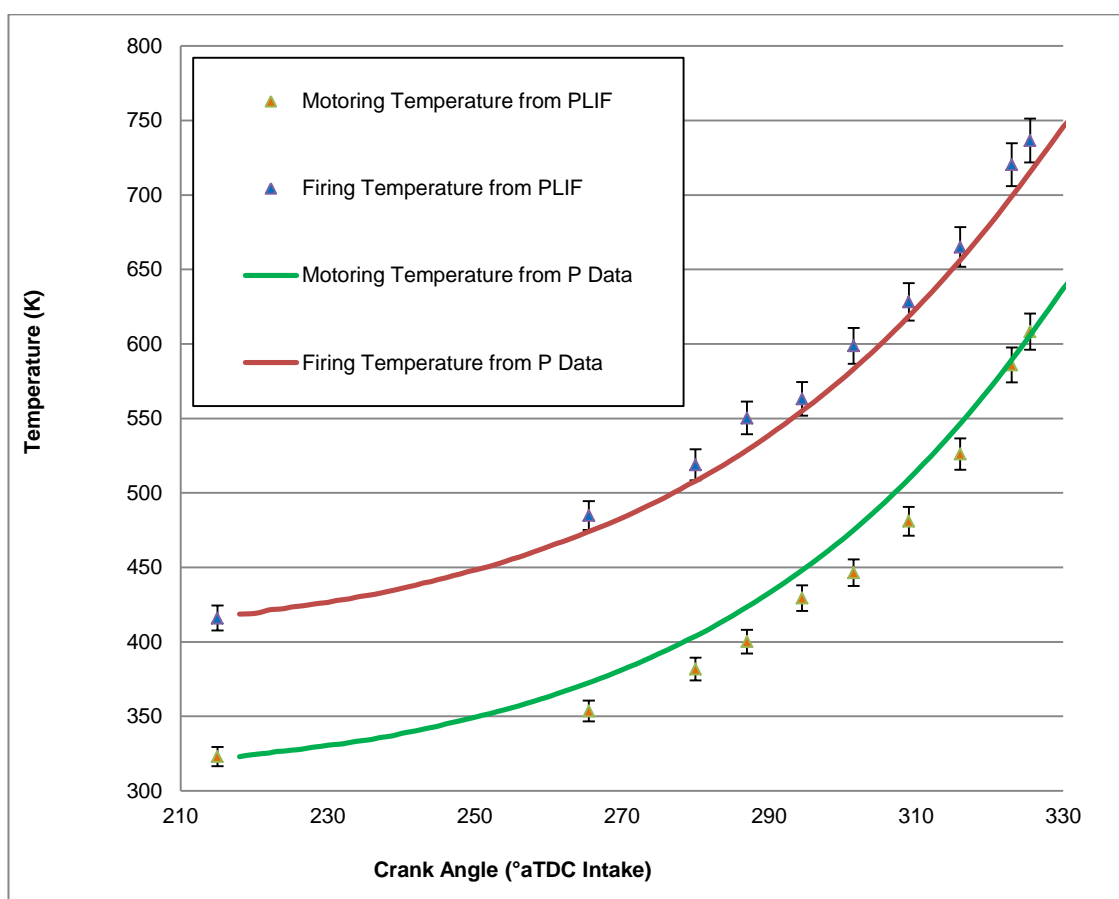
Figure 4-4: Validations under motoring and firing conditions [78]

Figure 4-5 includes details of the image processing procedure for temperature measurements. Customised software was used to separate odd and even files for 308nm and 277nm respectively from the combined 40 frames captured. WinView 32 was used to subtract the averaged background images from averaged data images in which the PFI (tracer) and PFI (tracer)+DI (fuel) were present, thus the averaged intensity values of a fixed ROI for both lasers could be obtained.

$$R_{PFI} = \frac{308PFI_{avg} - 308BK_{avg}}{277PFI_{avg} - 277BK_{avg}} \tag{1}$$

$$R_{(PFI+DI)} = \frac{308(PFI+DI)_{avg} - 308BK_{avg}}{277(PFI+DI)_{avg} - 277BK_{avg}} \tag{2}$$

Equation 1 indicates the ratio of intensities for PFI (tracer) which was intended to analyse the averaged charge temperature without fuel injection. Whereas Equation 2 represents the ratio for the cases with fuel added, therefore the degree of charge cooling could be determined at varied operating conditions. The initial intent was to compare the degree of cooling obtained with the different fuels but due to the relatively poor performance of the ethanol fuels under warm engine conditions (plus potential additional interference from gasoline component fluorescence), this proved not to be possible as discussed in detail later on.

To specify the actual temperature values, data pegging with the calibration curve requires further processing including laser effect removal and calculating the temperature from in-cylinder pressure data of a reference point. However, as it was only intended to evaluate the charge cooling effect (ΔT) for the current work, these processes were not deemed necessary.
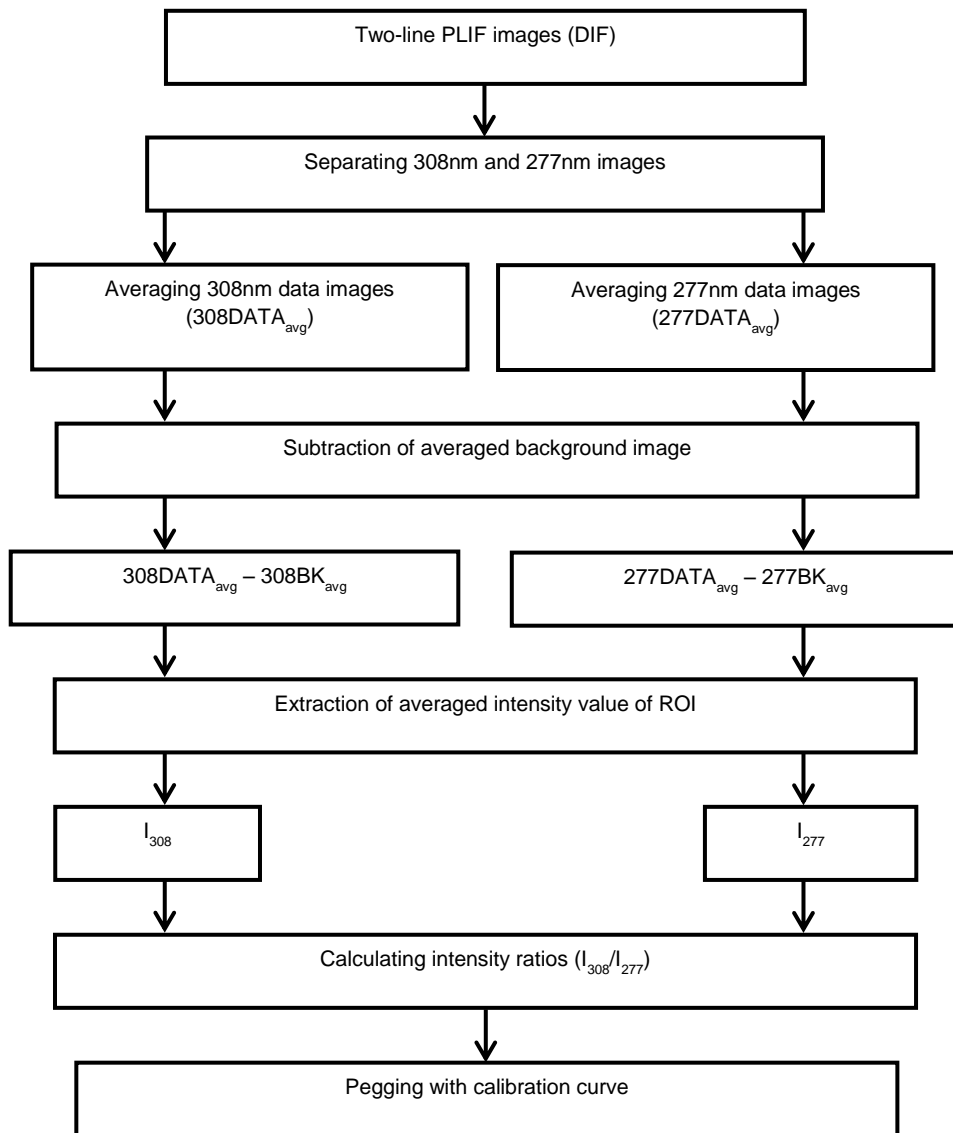
Figure 4-5: Image processing procedure for Planar Gas Temperature Measurements

4.4 Image Analysis and Cycle Selection Procedures

4.4.1 Fuel Distribution

The aim of initial testing was to evaluate the fuel stratification apparent in the visible horizontal plane within the combustion chamber at varied fuel injection timings and pressures with different fuels. Specifically, the goal was to evaluate stratification during "typical" individual cycles and thereafter quantify cyclic variation in such stratification over 20 cycles captured at each fixed condition. The typical cycle was selected manually as that considered to be visually representative of the most common reoccurring fuel pattern at the given injection timing and pressure. The fuel imaging tests were all performed under motoring conditions at 1200rpm, with the engine coolant and oil supplies operated fully warm as described previously.

While visual inspection of such images provides a primary method of qualitative interpretation, statistical analysis of the intensity spectrum significantly bolsters the evaluation of such results. In order to statistically verify the homogeneity of the typical cycles for all timings and fuels a fixed Region of Interest (ROI) was defined, as shown in Figure 4-6. This ROI consisted of a total 235,875 pixels (555x425), which equated to ~55% of the piston window viewing area. Thus the statistical analysis is restricted to the region around the spark plug where the laser sheet maintained acceptable profile. This viewing area restriction was still considered tolerable, as this region is where the crucial early flame development process takes place. An additional limitation of the analysis was exclusion of the segment on the left of the ROI, where that area apparently often consisted of a relatively high concentration of fuel (the result of the injector aiming towards that direction).
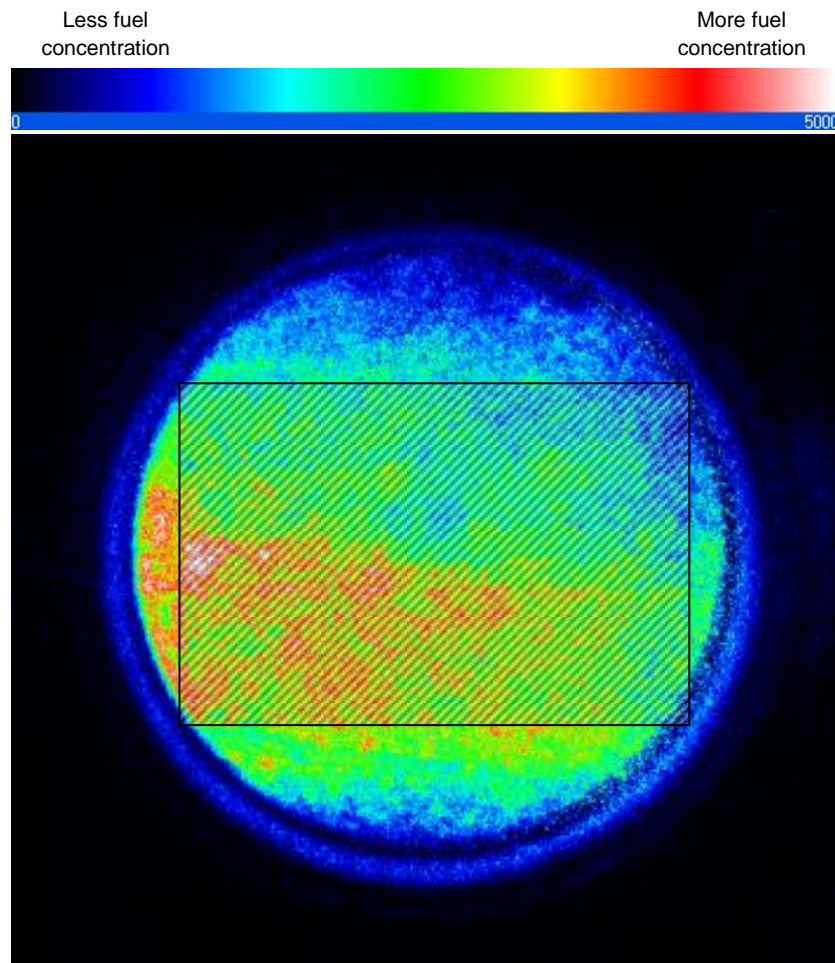
Figure 4-6: ROI (555x425) for homogeneity quantification

4.4.2 Repeatability Effects

Given the "typical" cycle was manually selected (as is often the case for such optical imaging work) the analysis presented in the currently reported thesis must be considered as subjective. One advantage of additional simple statistical analysis is demonstration of the repeatability of such images without need to manually review all 20 sets of images for all cases. In particular, the repeatability of the biased stratification towards the left-hand side of the bore required further quantification (which visually seemed repeatable when looking at frames from successive cycles). Some caution is required as 20 cycles is probably insufficient in number to fully bottom-out cyclic variation in the fuel distribution. However, clearly such work was restricted due to the labour intensive nature of the task.

In an attempt to quantify such effects the images were divided into two new separate regions of interest, as illustrated in Figure 4-7. The combined ROI contained a total of 435,420 pixels (738x590), therefore a greater area of interest was covered than above. As illustrated, the ROI was equally divided into left and right hand regimes. During the processing the mean value of intensity was calculated within each of these regimes (individually and also when recombined as a whole) and this was repeated for the full 20 cycles captured at every fixed condition. In summary, this additional processing was not aimed at evaluating the stratification within individual cycles but rather the repeatability of such stratification effects across the full 20 cycles captured at each injection timing and pressure.
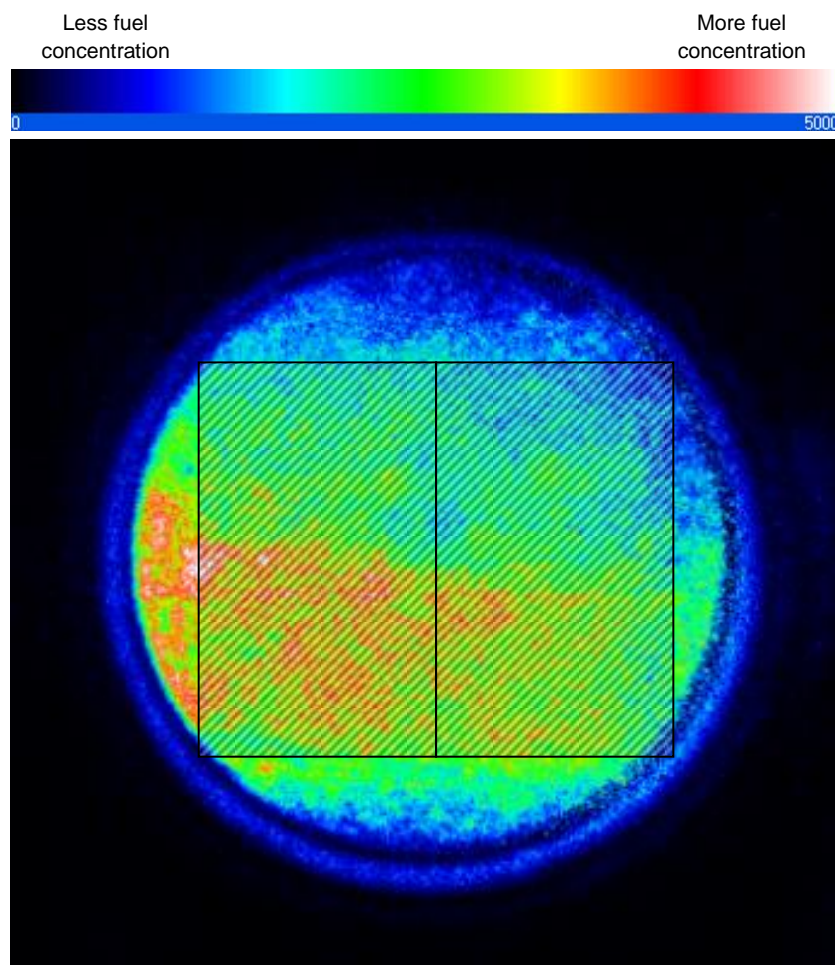
Figure 4-7: ROI (738x590 total) for repeatability clarification

Chapter 5 Results and Analysis

5.1 Planar Fuel Distribution Visualisations

The fuel injection pulse width was determined in prior firing setup tests (with the optical windows still fitted). For each fuel the pulse width and intake throttle position was fixed to the value required to maintain a load of 3.5bar net IMEP with optimum spark timing, fixed SOI timing of 270°bTDC and a rail pressure of 100bar. This process was then repeated to determine the required pulse width to be used with each fuel at 200bar rail pressure. Hence one limitation of the work, for a given fuel pressure, was the assumption that the pulse width would remain fixed throughout the injection timing sweeps. In all of the motoring tests the single-line PLIF technique was adopted, with the 308nm XeCl laser employed alone. The three fuels used were iso-octane, E10 and E85 which were all evaluated at both 100bar and 200bar rail pressure, with the SOI timing swept but the pulse width held constant at that mapped in firing mode for each fuel. For the image processing, Single Image Frames (SIF) was adopted and two sets of 20 frames were taken under i) background and ii) DI (fuel & tracer) conditions for test, as detailed in Table 5-1.

Table 5-1: Planar fuel distribution visualisations

Fuel	Iso-octane	E10	E85
Speed (rpm)	1200	1200	1200
IMEPn (bar)	~3.5	~3.5	~3.5
λ	1	1	1
SOI (°bTDC)	330 → 90 (60°c.a. incr.)	330 → 90 (60°c.a. incr.)	330 → 90 (60°c.a. incr.)
Fuel Pressure (bar)	100 & 200	100 & 200	100 & 200
Injection Duration (ms)	0.54 & 0.41	0.59 & 0.44	0.80 & 0.64
Coolant Temperature (°C)	30 & 60 & 90	30 & 60 & 90	30 & 60 & 90
Camera Capture Timing (°bTDC)	30	30	30

5.1.1 Fuel Type and Injection Setting Effects

The aim of initial testing was to evaluate the fuel stratification apparent in the visible horizontal plane within the combustion chamber at varied fuel injection timings and pressures with different fuels. Specifically, the goal was to evaluate stratification during "typical" individual cycles and thereafter quantify cyclic variation in such stratification over 20 cycles captured at each fixed condition. The typical cycle was selected manually as that was considered to be visually representative of the most common reoccurring fuel pattern at the given injection timing and pressure. The fuel imaging tests were all performed under motoring conditions at 1200rpm, with the engine coolant and oil supplies operated fully warm as described previously, throttle was set at its minimum opening.

Set out in Figure 5-1 are the selected "typical" fuel distribution images at 100bar for all three fuels with the SOI timing swept from 330 to 90°bTDC, as annotated. Every image was obtained with the piston at 30°bTDC firing and therefore illustrated the two-dimensional planar fuel field just before ignition. The dimensionless intensity scale was set to 0-5000, considered to allow the best compromise between avoiding wasted scale and optimising the visual impact of the comparison. The position of the intake and exhaust valves are also shown marked in the first frame of Figure 5-1 for clarity (with the intake valves at the bottom). In the second frame the usable width of the laser sheet can also be seen marked, which clearly further restricted the appropriate viewing area. Comparing the images visually, the iso-octane case appears to present the most homogeneous appearing planar image for the typical cycles selected, with an apparent optimum injection timing of around ~270°bTDC in good agreement with the low COV of IMEPn (~2%) observed with this timing during prior firing setup tests. Caution is required as this imaging only represents a single two-dimensional slice through part of the chamber. Nonetheless, it would appear that injection at or near to this timing was beneficial with all three fuels in terms of minimising the planar stratification. Comparing fuels, both E10 and E85 resulted in a higher degree of variation in intensity, although the E10 case appears much improved and more similar to iso-octane at 270°bTDC. Some caution is required as the alcohols were mixed with pump gasoline, some of the components within which may have fluoresced and hence influenced the spectrum of intensity values recorded. However the similarity between the iso-octane and E10 cases

at 270°bTDC might indicate that such gasoline components were not drastically interfering.
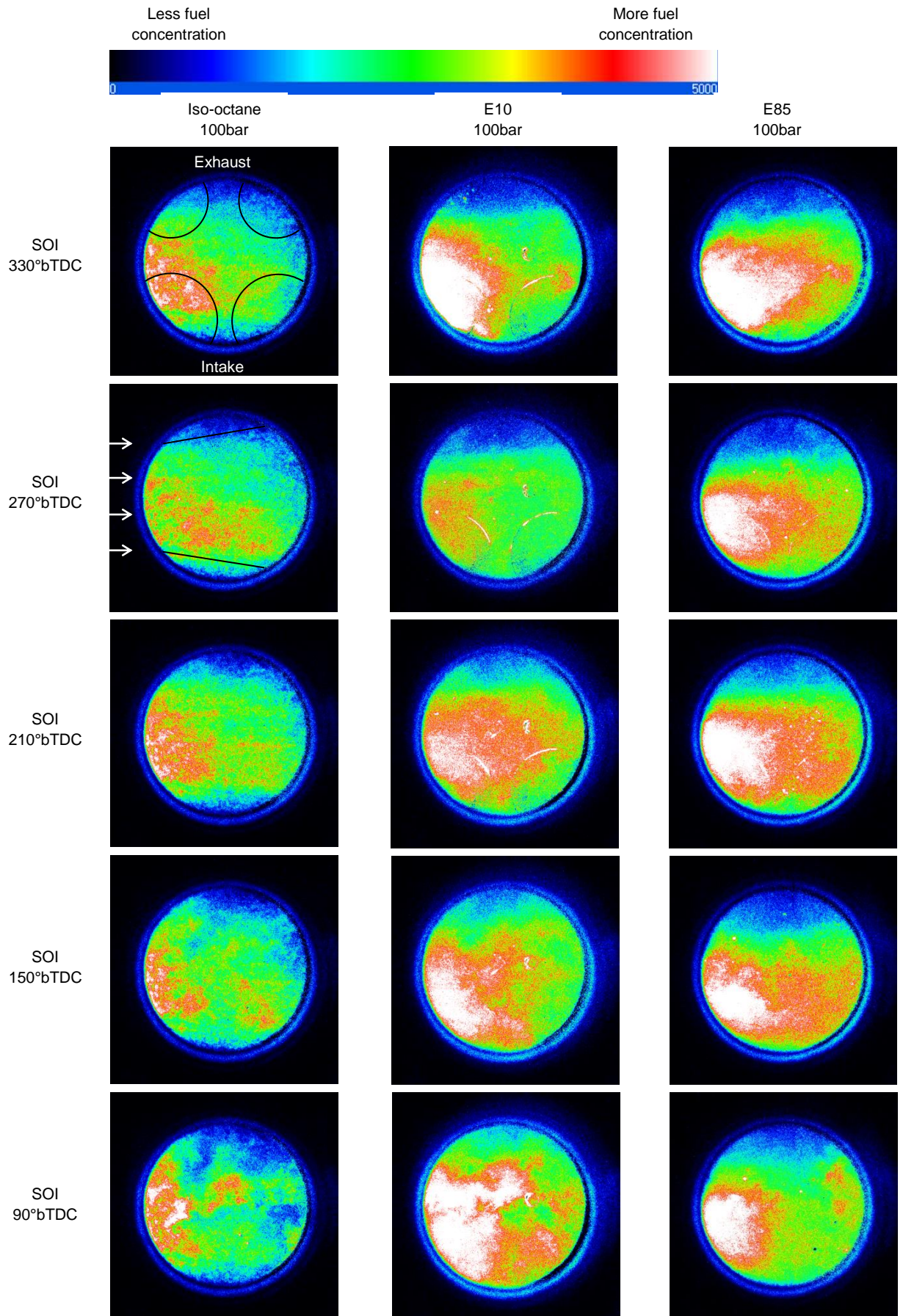
Figure 5-1: "Typical" fuel distribution images (100bar rail pressure)
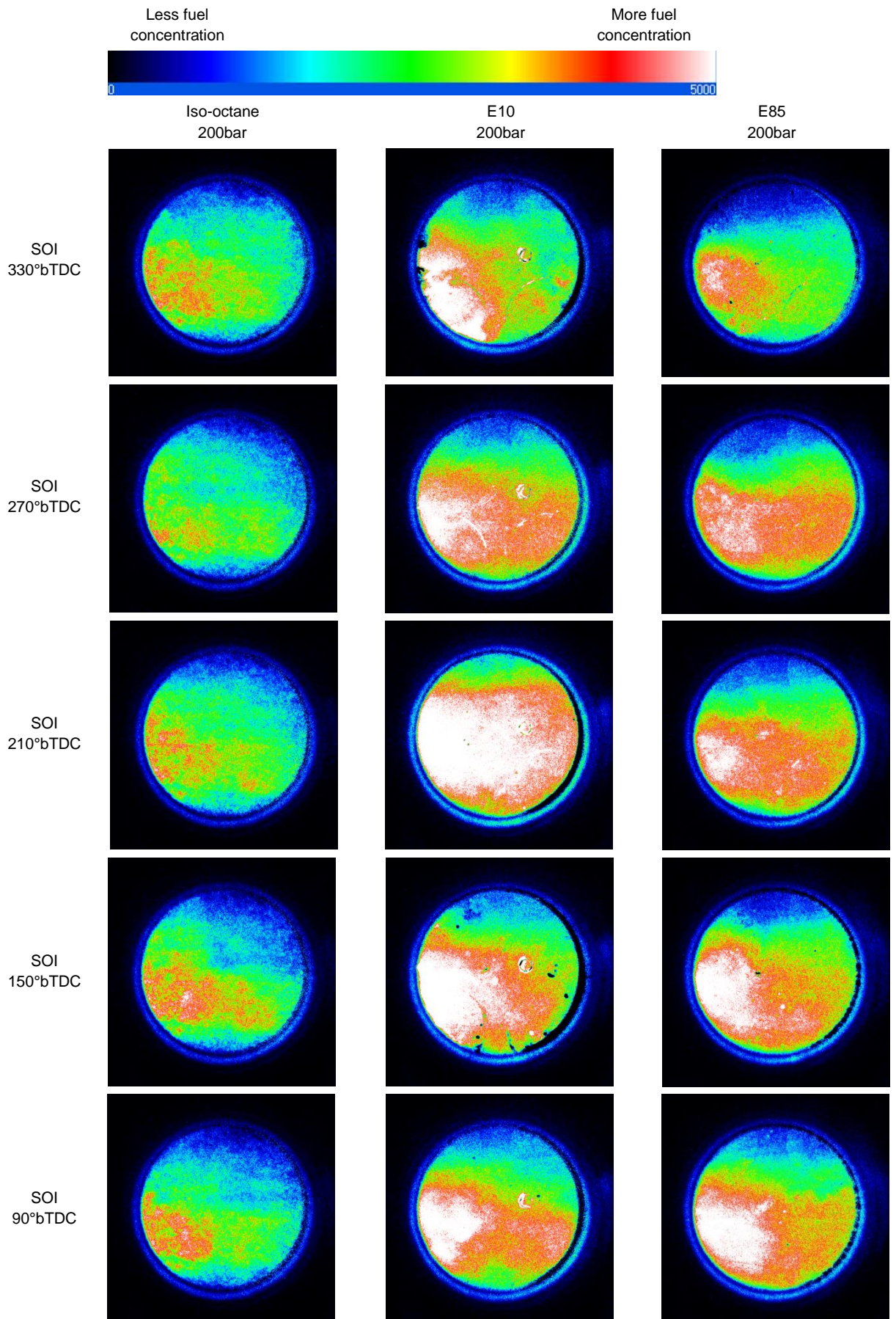
Figure 5-2: "Typical" fuel distribution images (200bar rail pressure)

Set out in Figure 5-3 are corresponding values of the COV of intensity in the ROI for each of the frames set out in Figure 5-1. Overall, considerable variation in intensity was recorded for all fuels. Translation to real variation in absolute fuelling would require prior understanding of the real minimum and maximum air-to-fuel ratio, and while Johansson et al. [117] have shown this can be extracted from PLIF (by effectively calibrating the signal using a series of known homogeneous fuel fields at varying fuelling levels), such calibration was considered beyond this work. Nonetheless, the current simple analysis further demonstrates the variation in intensity was apparently worse with very early or late injection and also with alcohol/gasoline content in the fuel under "homogeneous" DI conditions (albeit the high ethanol fuel arguably exhibited a flatter response at the extreme settings studied). These observations will be returned to later in when discussing measured exhaust emissions data.
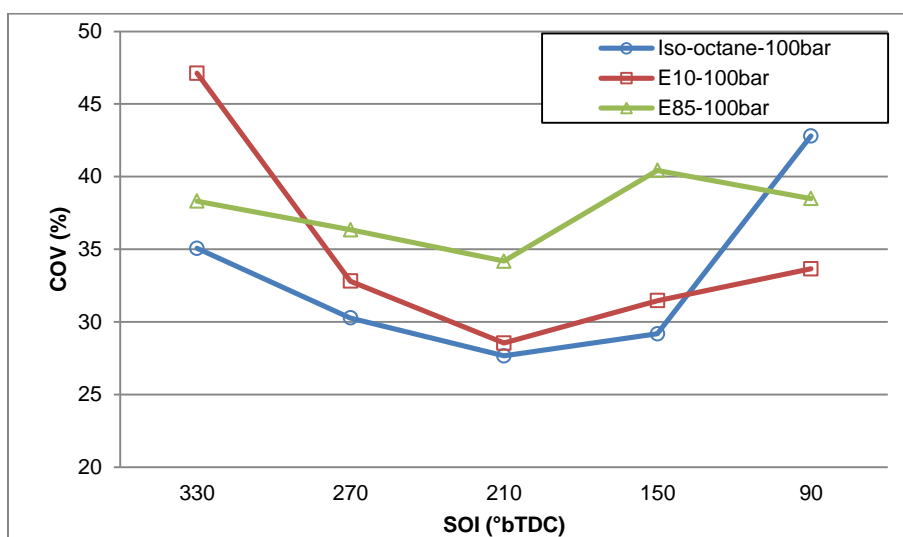
Figure 5-3: COV of intensity (100bar)

Set out in Figure 5-2 are equivalent images for the "typical" cycle images recorded at 200bar. Visually, it appears that the degree of bias towards the left-hand side of the bore had been reduced with elevated rail pressure, particularly in the case of the ethanol fuels. As shown in Figure 5-4, the ROI analysis revealed considerable variation remaining across the interrogation area for all fuels. However, this variation was generally reduced by the order of ~5% COV of intensity for all fuels and injection timings when compared to the prior 100bar rail

pressure cases summarised in Figure 5-3. It was again interesting to note the relative flat response of the high ethanol E85 case.

This elevated rail pressure resulted in reduced size of the fuel droplets hence added kinetic energy to the turbulent mixing, as droplet size is a function of pressure, the higher the fuel pressure the smaller the droplet size. Furthermore, droplet size is also dependent on spray pattern type, spray angle, nozzle type, specific gravity of the fuel (i.e. density), viscosity and surface tension. Ethanol has a relatively high density (0.78kg/m^3 @15°C) compared to gasoline (0.74) and iso-octane (0.69), together with relatively high kinematic viscosity (~1.5 cSt c.f. ~0.8 for gasoline) leads to a relative high resistance to flow (and hence injection). Such effects may at least partially account for the apparent reduced sensitivity of the high ethanol content fuel when viewing COV values (with high ethanol exhibiting higher resistance to injection flow under all conditions and hence less sensitive to varying timing).
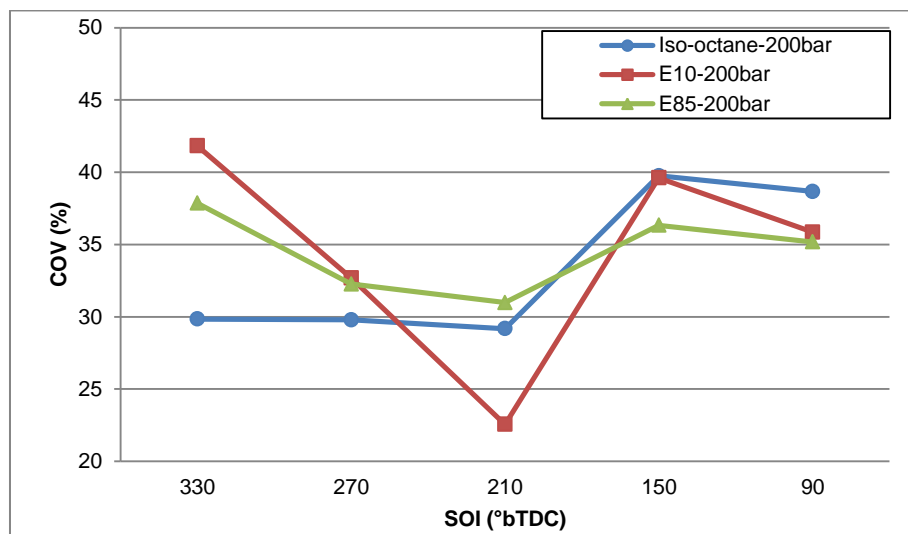
Figure 5-4: COV of intensity (200bar)

5.1.2 Fuel Pressure Repeatability Effects

Given the "typical" cycle was manually selected (as is often must be the case for such optical imaging work) the above analysis must be considered as subjective. One advantage of additional simple statistical analysis is demonstration of the repeatability of such images without need to manually review all 20 sets of images for all cases. In particular, the repeatability of the biased stratification towards the left-hand side of the bore required further quantification (which visually seemed repeatable when looking at frames from successive cycles). Some caution is required as 20 cycles is insufficient in number to fully bottom-out cyclic variation in the fuel distribution. However, the work was restricted due to the labour intensive nature of the task.

Set out in Figure 5-5 are corresponding results when comparing varying fuel pressures for the iso-octane alone. Overall it can be seen that the repeatability was consistent in each side, with a reasonable COV of mean intensity of ~5-8%. The mean of averaged intensity values for each zone are shown in Figure 5-6. These observations help quantify the repeatability within each side and persisting bias of the fuel towards the area targeted by the injector. The results also indicate that elevating the fuel pressure generally reduced the variation in ROI mean intensity between cycles, which is indicative of improved fuel-air mixture control.
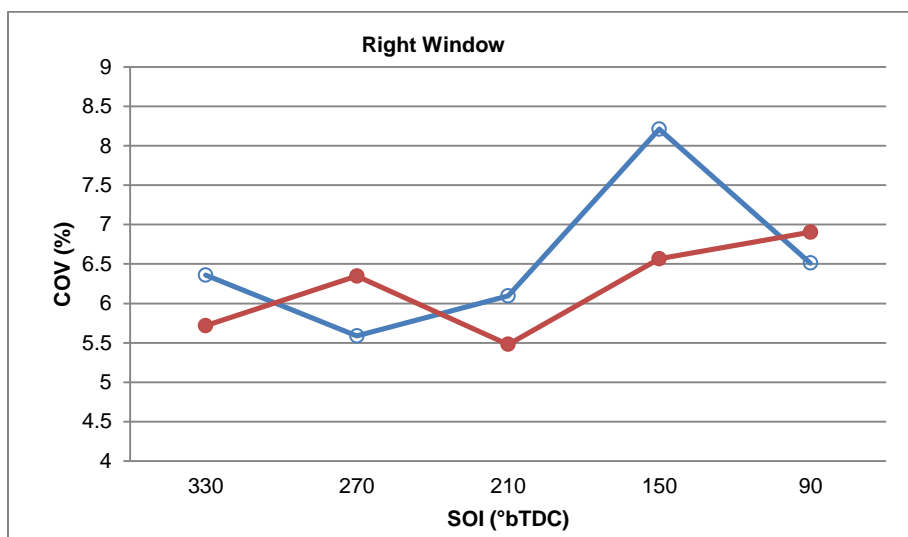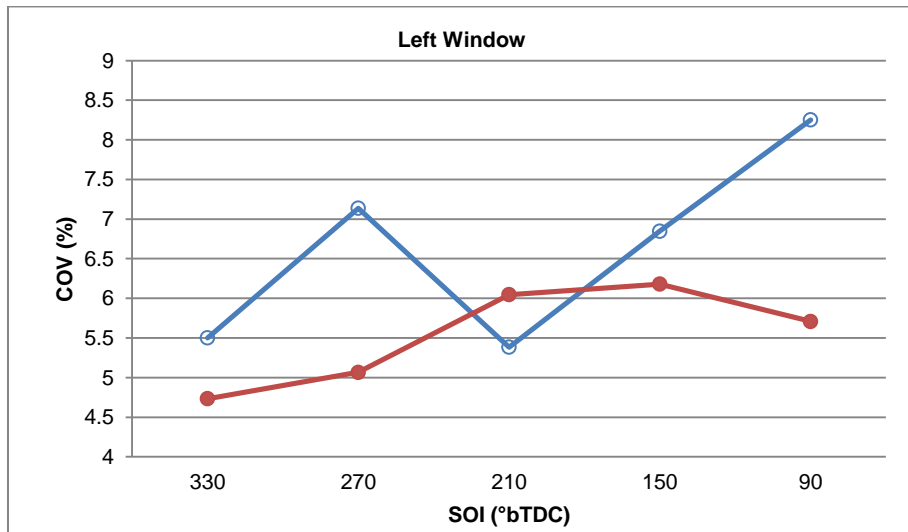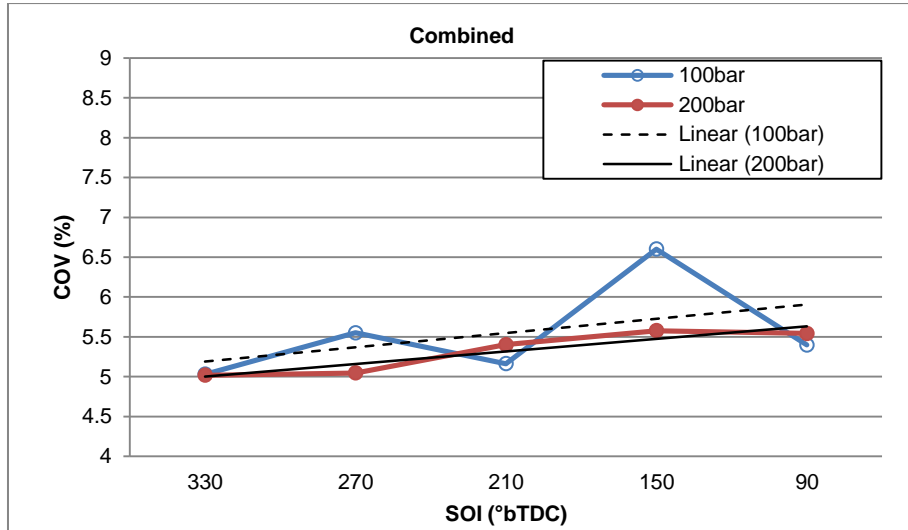
Figure 5-5: Fuel pressure repeatability effects (iso-octane)
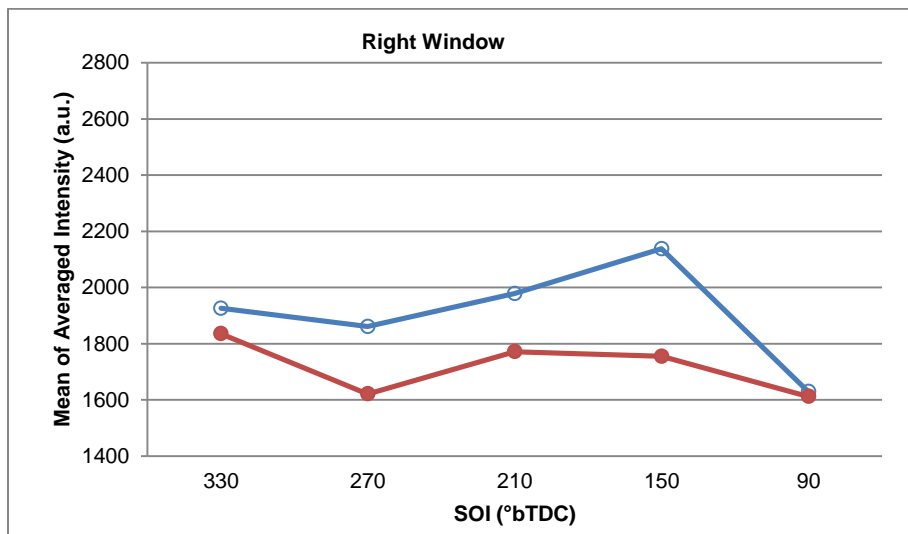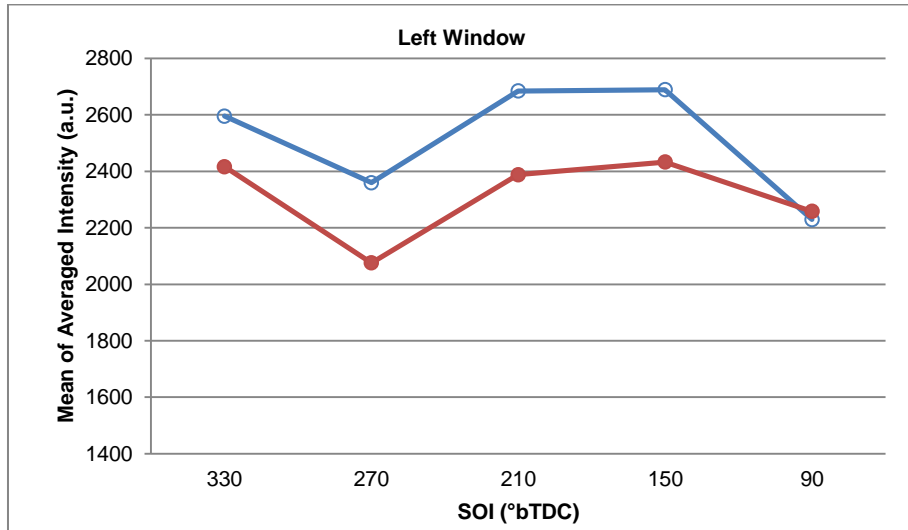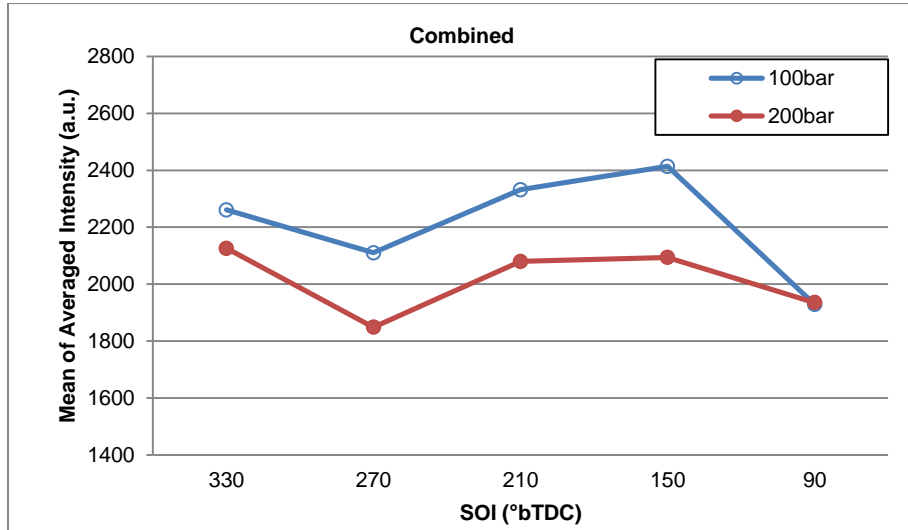
Figure 5-6: Mean of averaged intensity in each zone - fuel pressure repeatability effects (iso-octane)

5.1.3 Alcohol Repeatability Effects

Shown in Figure 5-7 and Figure 5-8 are equivalent results for the different fuels. From these results it would appear that at earlier injection timings the E10 performed similarly poorly to, if not worse than the E85 fuel and that both fuels generally experienced slightly greater variation than the single component iso-octane. Interestingly the high ethanol component fuel performed more consistently when the injection was later than 210°. This apparent improvement in repeatability may have been associated with higher charge temperatures later on in the cycle aiding the evaporation of the alcohol making up the bulk of the E85 fuel. In contrast, the E10 fuel still contained significant gasoline content, with a much wider range of boiling. This observation may have significant implications for repeatability in future stratified direct ethanol injection concepts, especially given the injector was installed to obey the manufacturers guidelines for such engines. The results indicate highly non-linear behaviour with varying ethanol content, which may also be a result of the known azeotropic behaviour of gasoline-ethanol blends and arising non-linear behaviour in terms of trends in engine performance and pollutant emissions [71].
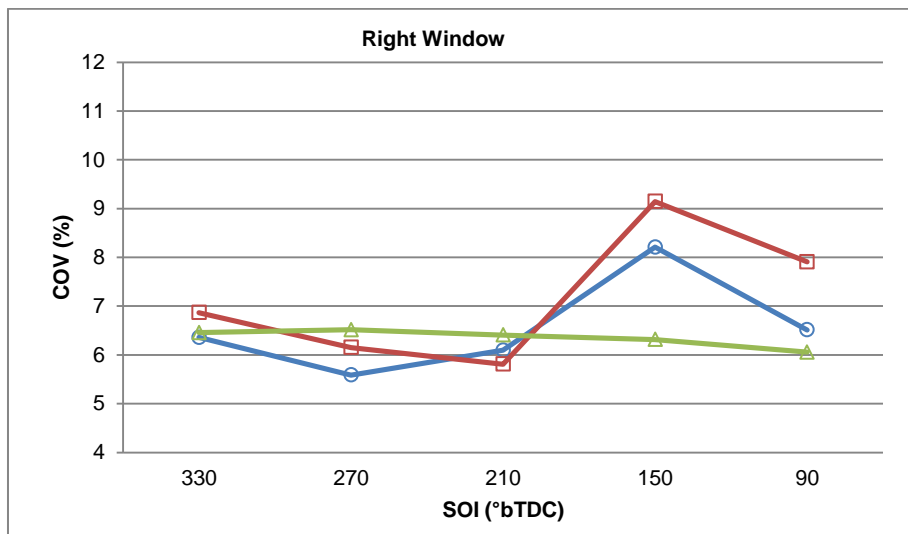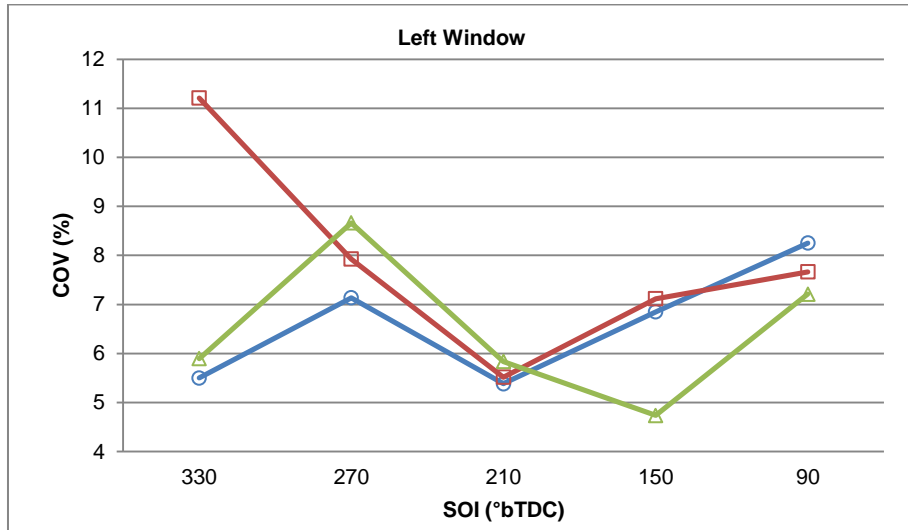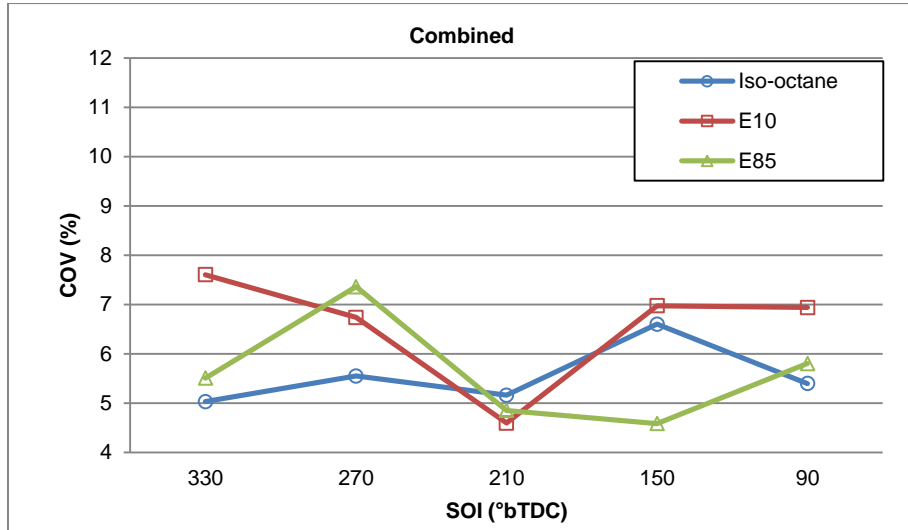
**Figure 5-7: Alcohol repeatability effects (100bar)**
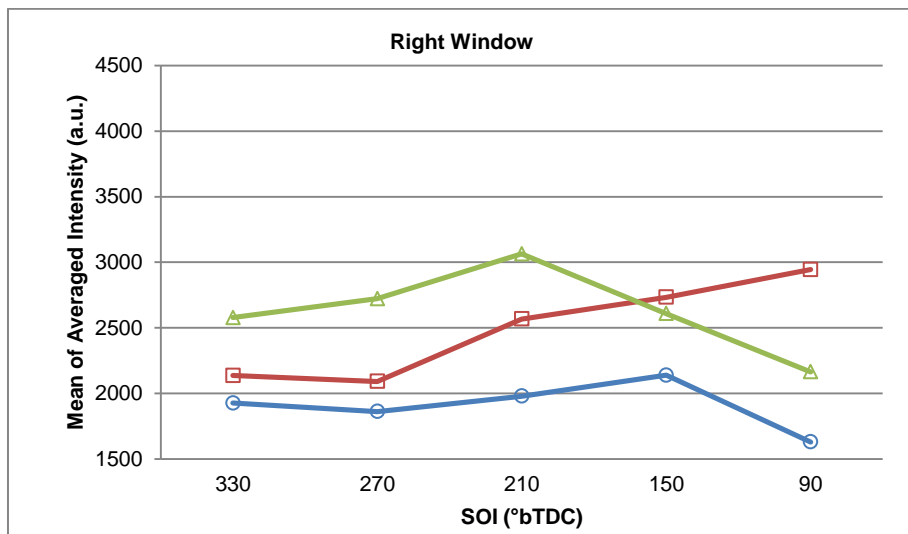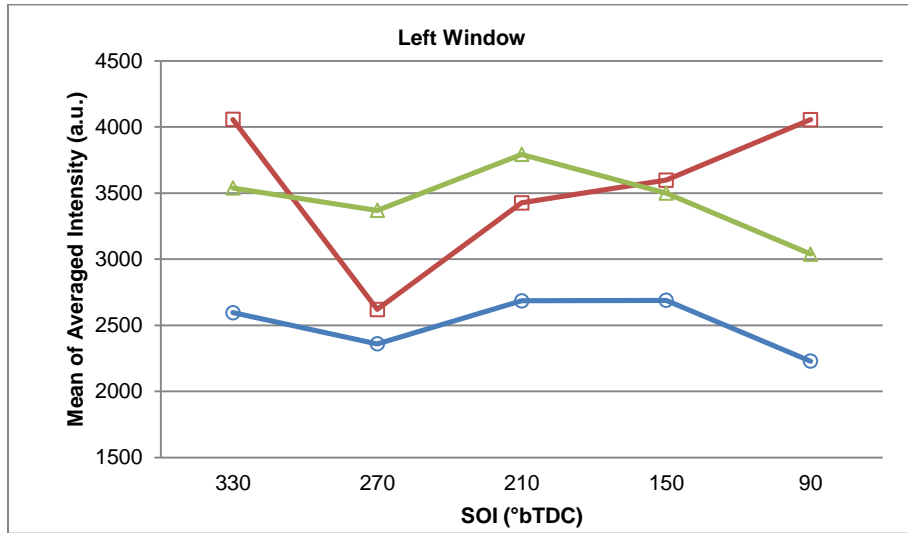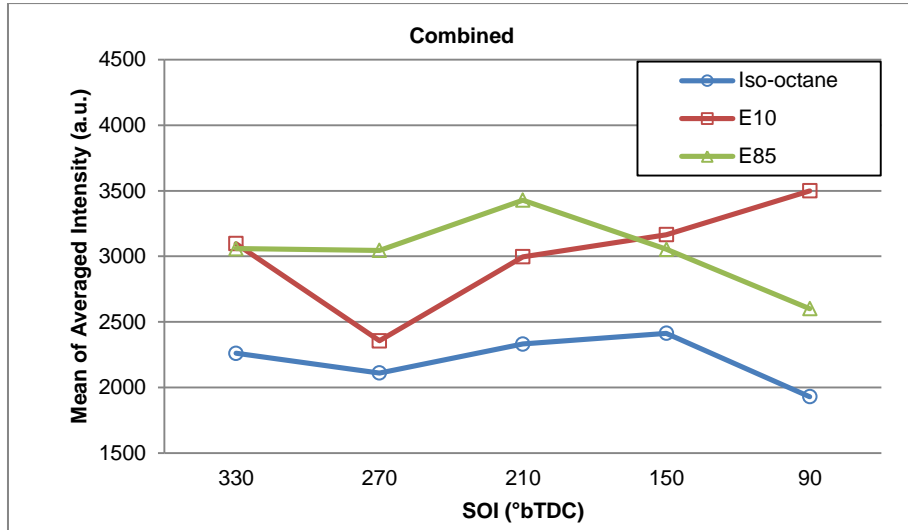
Figure 5-8: Mean of averaged intensity in each zone - alcohol repeatability effects (100bar)

5.1.4 Coolant Temperature Effects

In recent work at MAHLE Powertrain, Stansfield et al. [118] undertook New European Drive Cycle (NEDC) particulate emissions measurements in a MY2009 D-class passenger car fitted with a modern turbocharged DISI engine. A comparison of the particulate mass emissions recorded with "real" fuels is set out in Figure 5-9. These workers concluded that overall high ethanol content fuels led to a higher overall particulate mass over the full assessment. However the result with E10 fuel appeared contradictory, with the total particulate mass recorded lower than the baseline gasoline case.
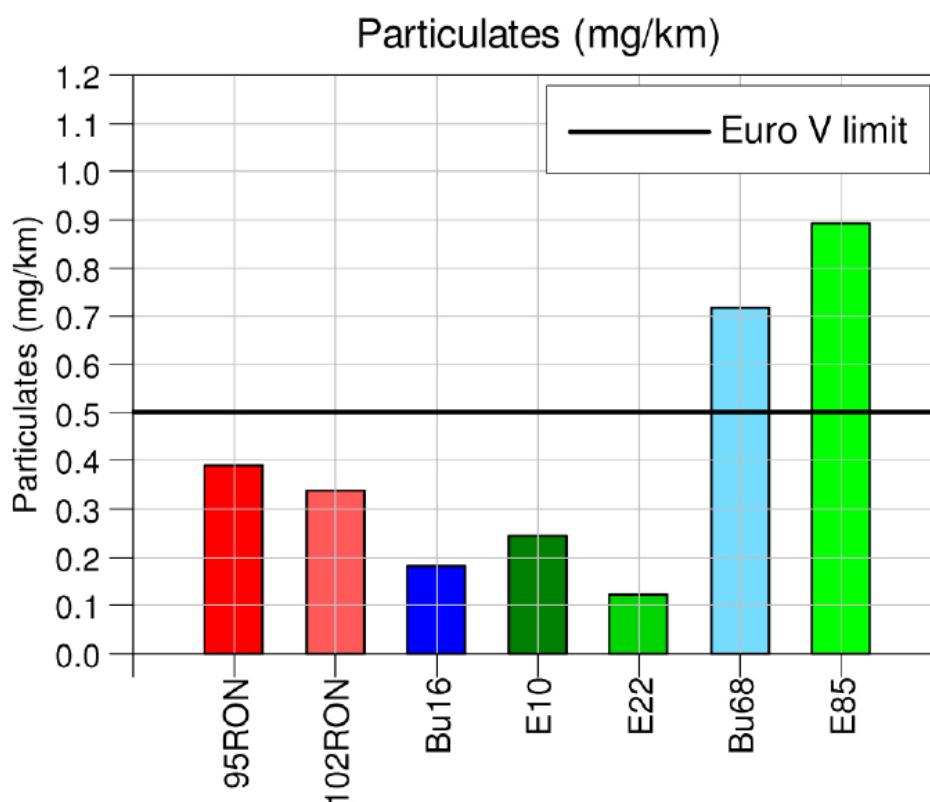
Figure 5-9: NEDC Particulate mass emissions [118]

More recently, Leach et al. [119] have evaluated the index (previously developed by Honda [33]) which links between the fuel composition and particulate matter emissions (as in PN index), model fuels with independent control of the double bond content and volatility were used in three different engines including a single-cylinder research engine, a V8 engine recently available in the market and

a current production supercharged V6 engine. Two particulate measurement instruments were employed, a Cambustion DMS500 and an AVL particle counter. Among the studies, the PN index was investigated in a Jaguar Land Rover V6 engine with five different fuels as listed in Table 5-2 over a simulated NEDC. Figure 5-10 and Figure 5-11 below show that the index trends are followed and the fuel composition is an important consideration when measuring the PN emissions over the drive cycle, nonetheless other factors can mask the effect of the PN index, particularly in the cold start phases.

Table 5-2: Driving cycle test fuel compositions [119]

	DBE + 1 % (v/v)	VP^a (kPa)	PN index (kPa^{-1})
Fuel 1	2.11	106.1	1.99
Fuel 2	1.98	92.9	2.15
Fuel 3	2.32	56.2	4.07
Fuel 4	2.28	47.8	4.77
Fuel 5	2.95	57.3	5.14

DBE: double-bond equivalent; VP: vapour pressure.
^{a}Either the DVPE or the RVP depending on fuel analysis method.
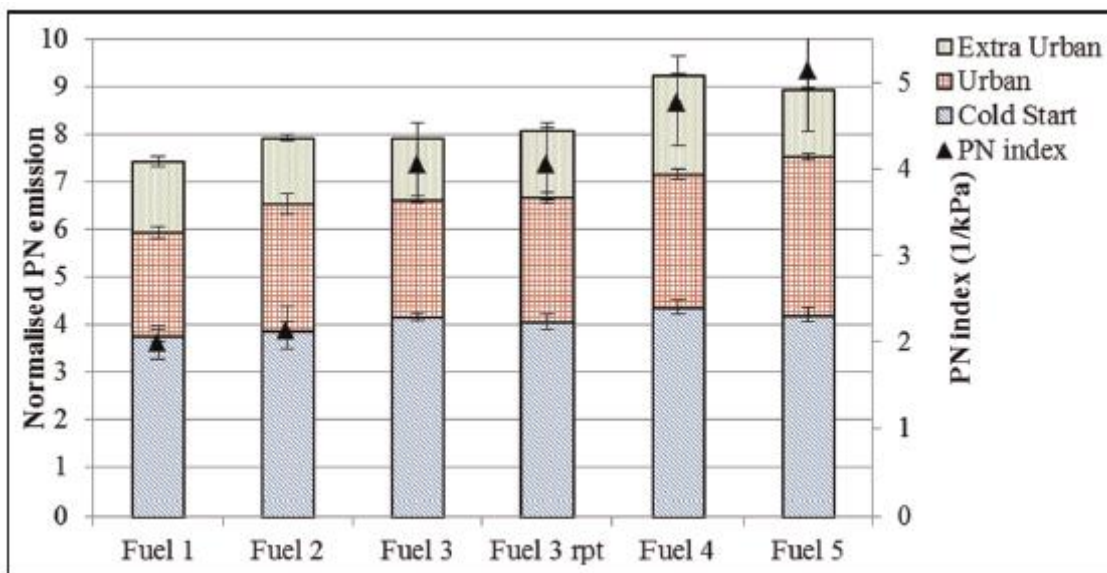
Figure 5-10: PN emissions over the NEDC [119]
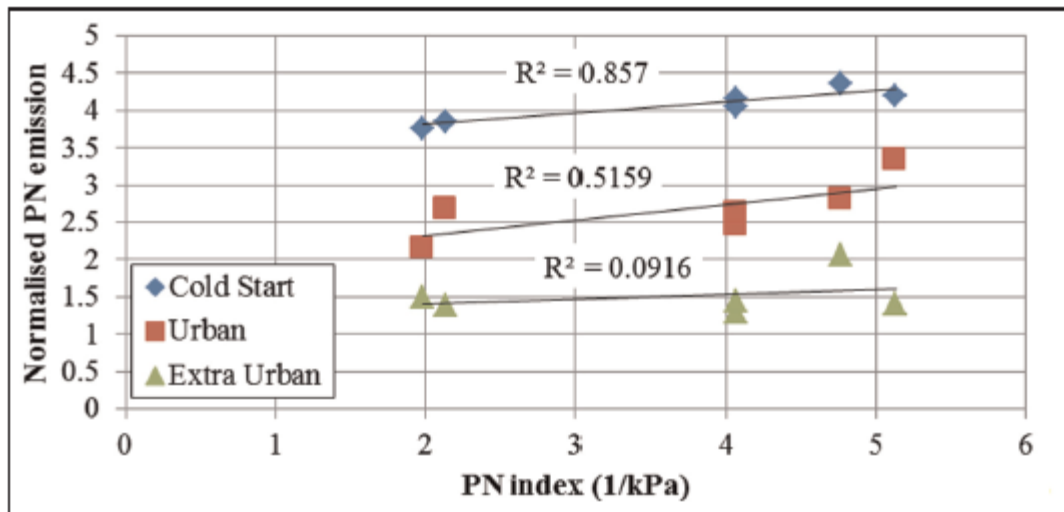
Figure 5-11: PN emissions plotted against PN index [119]

In the current work it was therefore decided to investigate the influence of varying coolant temperature on the visible fuel field with the current E10 fuel, with the coolant reduced in 30°C increments. The work was repeated at otherwise identical conditions to those employed during the fully warm tests (with the pulse width and throttle positions remaining fixed as above).

Set out in Figure 5-12 is the statistical analysis of coolant temperature effects based upon the repeatability analysis outlined above, the mean of averaged intensity values are shown in Figure 5-13. The 90°C recordings have not been repeated here as these were found to be very similar to those shown for 60°C. The results are only shown for iso-octane and E10, as E85 experienced severe evaporation issues throughout the low coolant temperature tests, but it can be seen that with 10% alcohol in the fuel the repeatability was much worse due to limited evaporation of the fuel. Where non-linearity was observed, especially for the iso-octane case at 30°C, this may be partly attributable to the data at 210°bTDC corresponding to the lowest piston position examined, where increased wall surface area may have influenced the heat transfer from the charge (albeit this remains speculative). This poor evaporation was clearly evident when reviewing the raw images as shown in Figure 5-14, with large droplets of liquid fuel clearly remaining within the chamber in the E10 case regardless of injection timing, even with the liner at elevated coolant temperatures.
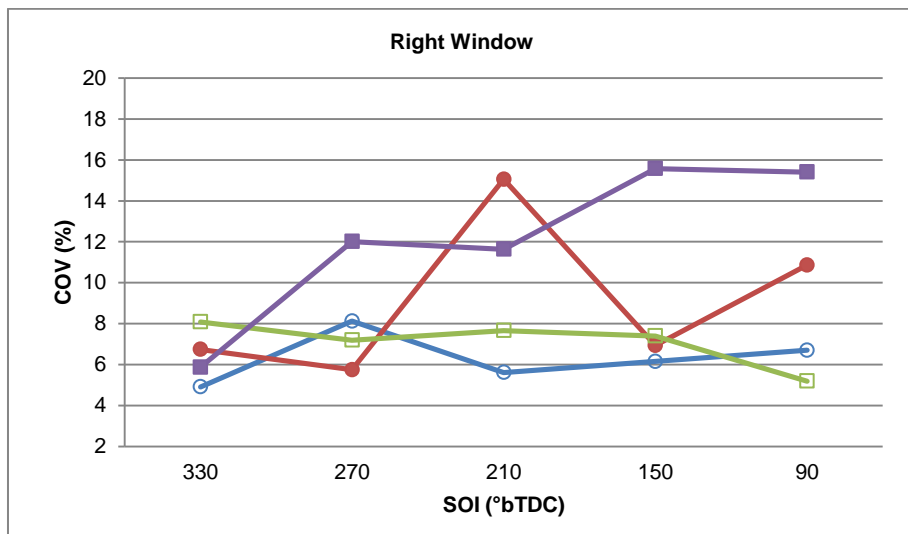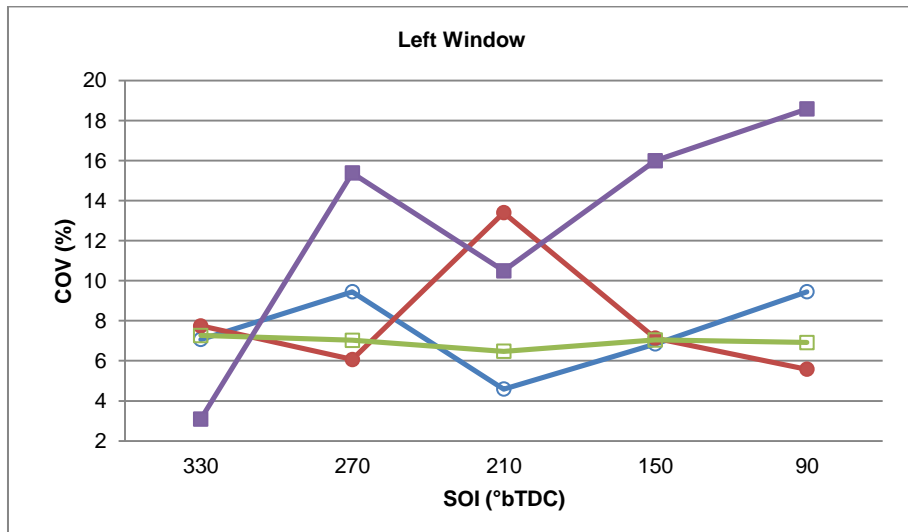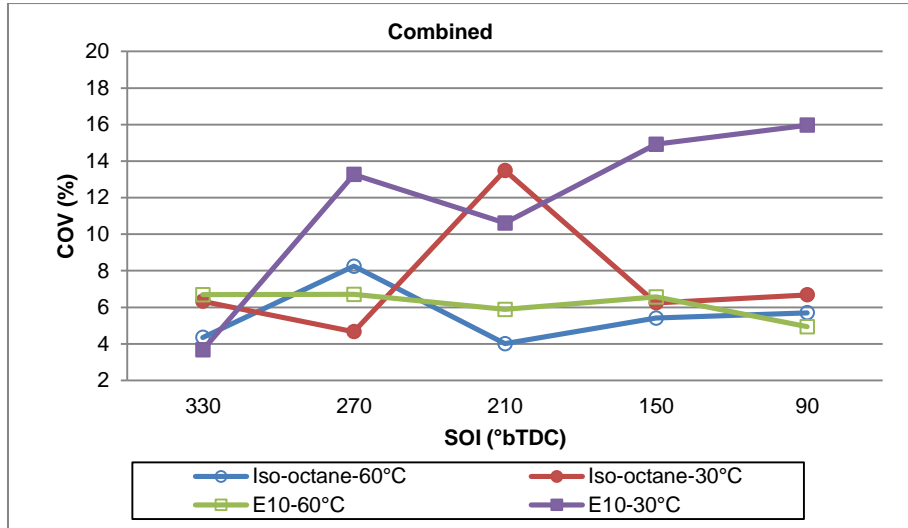
Figure 5-12: Coolant temperature effects (100bar)
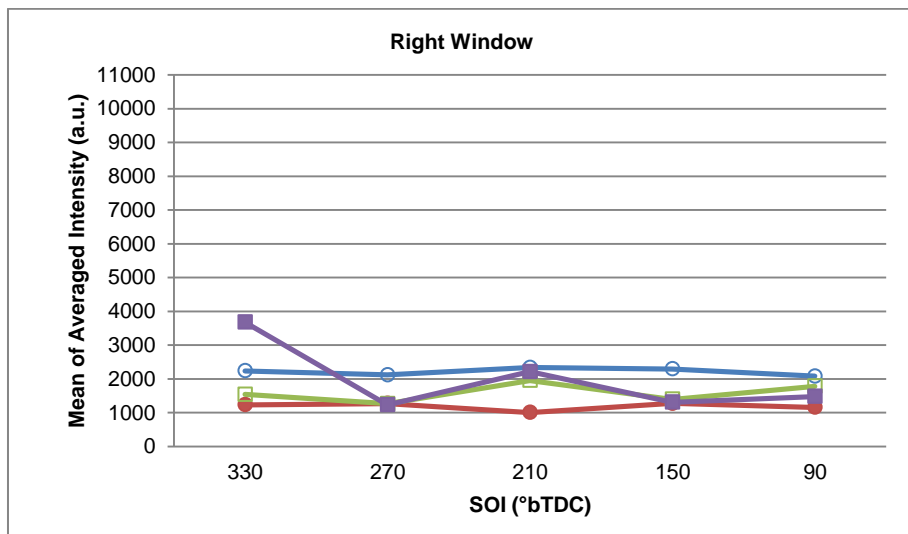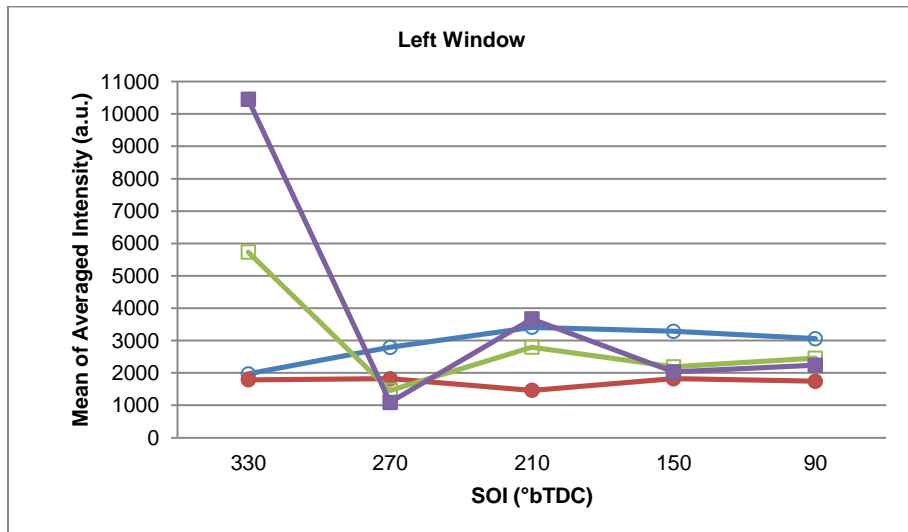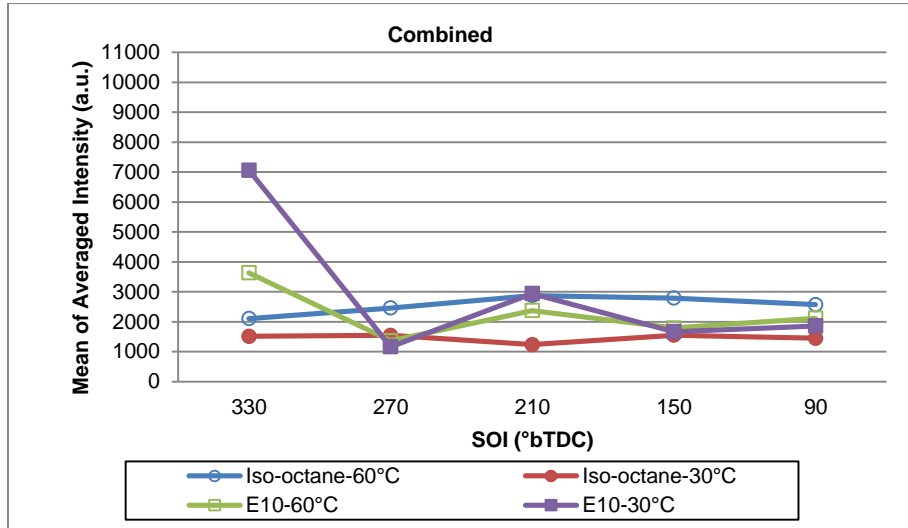
Figure 5-13: Mean of averaged intensity in each zone - coolant temperature effects (100bar)
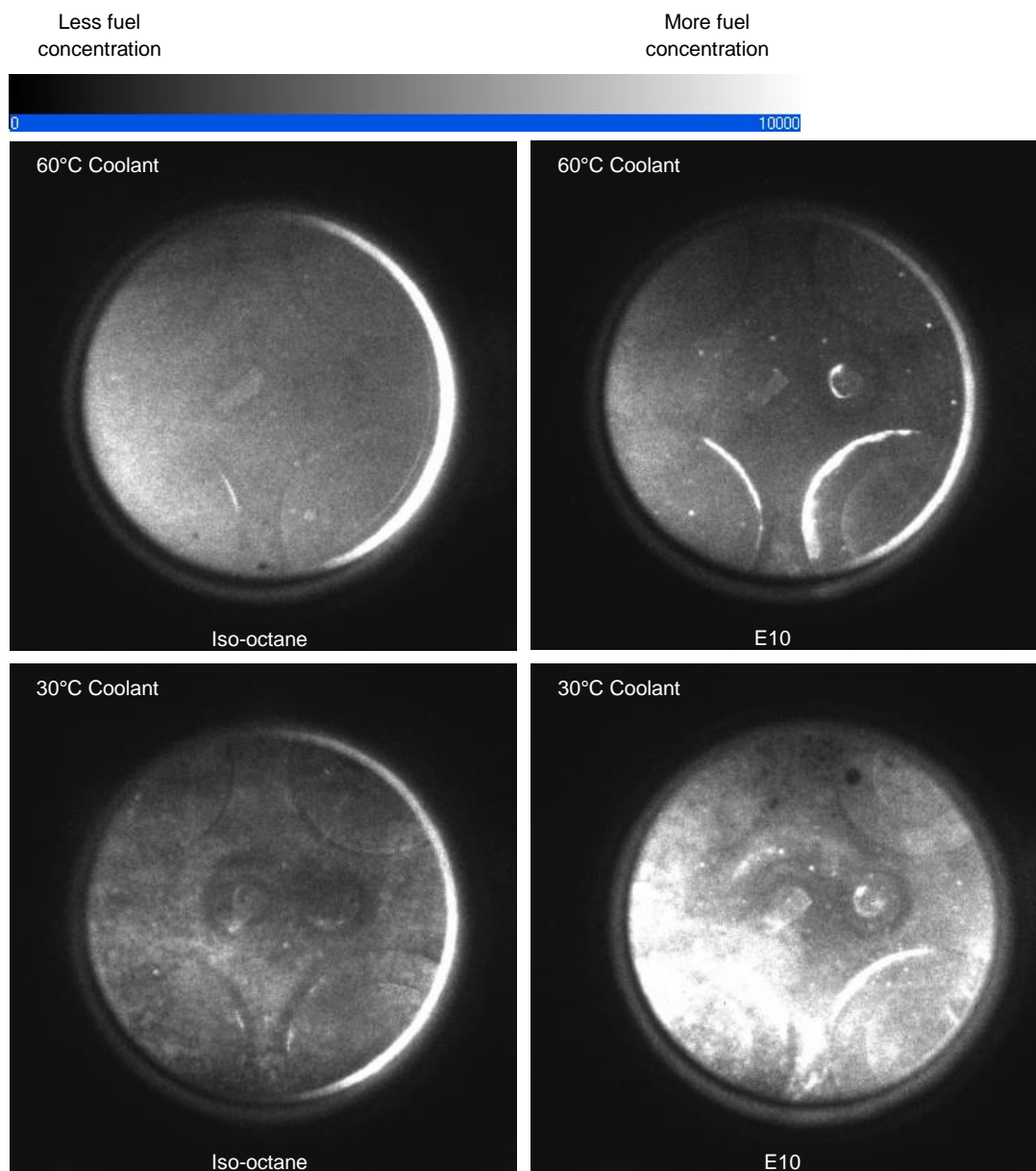
Figure 5-14: Raw images at varied coolant temperatures (100bar, SOI 270°bTDC)

5.2   Planar Gas Temperature Measurements (Charge Cooling Effects)

Following on from these tests it was decided to attempt to employ the two-line technique to evaluate the degree of charge cooling recorded but with the iso-octane fuel alone. Only iso-octane could be evaluated given the source of noise due to Mie scattering from fuel droplets with E10, as well as E85.

For the two-line PLIF experiments DIF was used to capture both images (308nm and 277nm) with a burst period (delay) of 30µs in succession. In consideration of 139µs duration for each crank angle degree at 1200rpm this delay was not considered to be significant. Three sets of 40 frames (20 for each laser) were captured as background, PFI (tracer) and PFI (tracer)+DI (fuel) images for iso-octane under motoring conditions, as illustrated in Table 5-3.

Table 5-3: Planar gas temperature measurements (Charge Cooling Effects)

Fuel	Iso-octane
Speed (rpm)	1200
IMEPn (bar)	3.5
λ	1
SOI (°bTDC)	330 → 90 (60°c.a. incr.)
Fuel Pressure (bar)	200
Injection Duration (ms)	0.41
Coolant Temperature (°C)	30 & 60 & 90
Camera Capture Timing (°bTDC)	30

Set out in Figure 5-15 is the corresponding changes in temperature (ΔT) recorded when the fuel was injected at different SOI timings under varied coolant temperatures. The values indicate the reduction in temperature measured with the piston at 30°bTDC (hence around ignition) relative to the motoring engine

case without fuel. Overall, when the liner was heated to the fully warm condition a similar change in charge temperature was noted regardless of fuel injection timing, with only ~7°C difference arguably indicating acceptable evaporation in either injection case. Such low sensitivity to injection timing was also apparent with 60°C coolant temperature. However, at 30°C the early injection process performed relatively poorly in terms of evaporation. This was also evident in the raw images shown in Figure 5-14, where droplets could be seen for the first time with this single component fuel. Given the wider range of boiling of the real fuels examined, it was clear that the iso-octane presented a best case scenario and that all fuels should still benefit from fast acting multiple injection strategies during the engine warm-up phase.
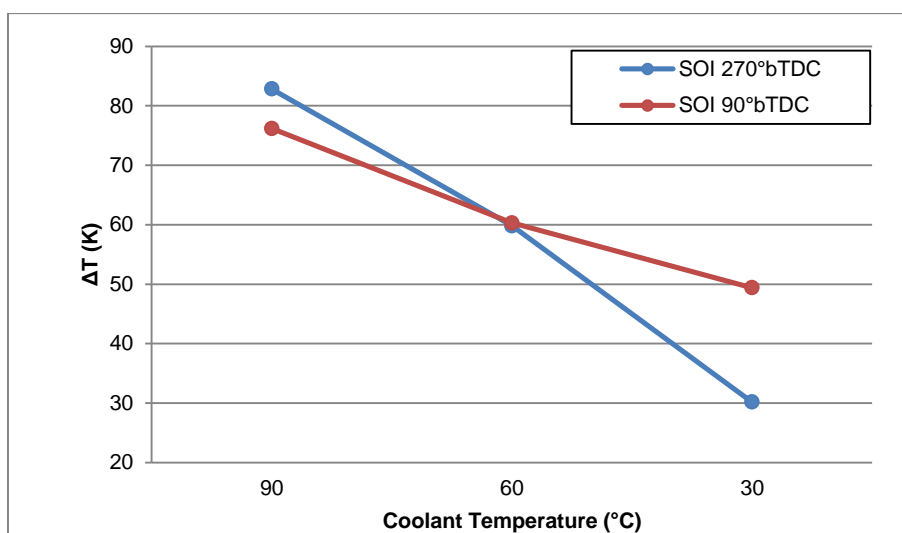
Figure 5-15: Charge cooling effects (iso-octane, 200bar)

5.3   Emissions

5.3.1   Fuel Pressure Versus SOI Effects (Iso-octane)

To bolster the observations made via the optical results a Horiba (MEXA-7170DEGR) motor exhaust gas analyser and AVL 415SE smoke meter were connected to the engine exhaust runner pipe (mounted mid-runner with each probe tip at the centre of the runner. Throughout the emissions sampling work the engine was operated under fully warm stoichiometric conditions (coolant temperature of 90°C, oil temperature of 50°C). The spark timing was also fixed at 30°bTDC firing throughout, which corresponded to Maximum Brake Torque (MBT) timing when the SOI was fixed at 360°bTDC when operating with iso-octane fuel at 1200rpm and ~3.6bar net IMEP. The throttle position was thereafter left fixed for all other conditions and the fuelling adjusted accordingly to maintain stoichiometry. The pegging method used for cylinder pressure was via polytropic index with 1 degree crank angle resolution. As a result the trends presented should be considered in the context of relative influence of the key parameter swept (as opposed to re-optimising the spark timing at each site to bring back the load and maintain MBT). During the mapping the side and piston crown glass windows remained fitted to the engine. It follows that the in-cylinder wall heat transfer characteristics were unrealistic, with the glass acting as an insulator and potentially elevating the gas temperatures above those otherwise incurred in full metal engines. This compounds the fact that the results presented should be viewed as qualitative. This was considered to be an acceptable limitation given the qualitative nature of the prior optical engine test work and associated observations. Furthermore, the current engine setup suffered from relatively poor low load throttle control, hence finite re-optimisation of spark and load at every fuel injection setting was not possible within the timeframe of the currently reported thesis (despite attempts to address this).

Set out in Figure 5-16 and Figure 5-17 are the thermodynamic results obtained when injecting pure iso-octane fuel at varied fuel rail injection pressures. The IMEP gross and net indicate the relative load achieved without and with the pumping loop being taken into account. The load fluctuated but only moderately across the majority of the sweep until the combustion stability deteriorated as the injection was retarded beyond 120°bTDC. A progressive "dip" in IMEP was

apparent in the middle of the sweep, with minimum IMEP at SOI=210°bTDC. This dip was not associated with fuel pressure or deteriorating combustion stability (such an increase in COV could have indicated poor relative mixing due to variation in the injection, bulk flow and/or turbulence). The Least Nominal Value (LNV) of net IMEP also confirms the robustness of the combustion across all 300 cycles logged, this lowest nominal value was calculated by dividing the minimum net IMEP by the average net IMEP and expressing as a percentage. Rather, this dip has been associated with variation in engine breathing, as reflected in the values of gas exchange efficiency (computed as the ratio of gross to net IMEP and expressed as a percentage), the gas exchange efficiency is also a relative measure of PMEP (Pumping Mean Effective Pressure). During engine breathing at typical part load conditions, as the intake valves open an expansion wave is usually generated in the engine intake runner that propagates back up the pipe at the local speed of sound. This wave is then reflected (usually via the plenum) back towards the engine. If the intake valves are timed appropriately and the intake runner is of optimal length for the engine speed, a compression wave approaches the engine cylinder as the intake valves close to restrict breathing. Ultimately, this wave may increase volumetric efficiency and hence engine output. However, the injection of the fuel during this period may also influence volumetric efficiency, with the interaction of the fuel with the flow and local charge cooling effects also influencing the density of the charge during the crucial period as the intake valves close. As the intake valves closed (with IVC at ~155°bTDC firing), the DI of the fuel as IVC was approached (and associated interaction with the bulk flow) could have obstructed the air filling during this crucial period. Another potential important factor to consider is backflow of charge into the intake system as the piston began to accelerate upwards with the intake valve still open, although this phenomenon occurs after the "dip". A final effect is dropping pressure as BDC is approached and the intake valves begin to restrict intake breathing. Such dropping pressure could have adversely influenced the interaction of the fuel and air at the start of injection. Such simple explanation neglects valve overlap effects, which may come into play due to exhaust tuning and exhaust-to-intake pressure differential across the engine. In the worst case this may reduce volumetric efficiency, due to residual gases being pushed back into the intake system upon inlet valve opening. Depending on the exhaust manifold design a compression wave in the exhaust may also return to the closing exhaust valves to the detriment of volumetric efficiency.

(a)

(a)
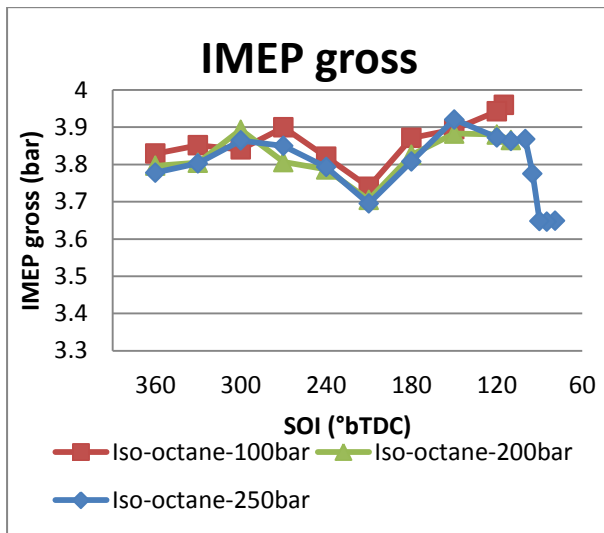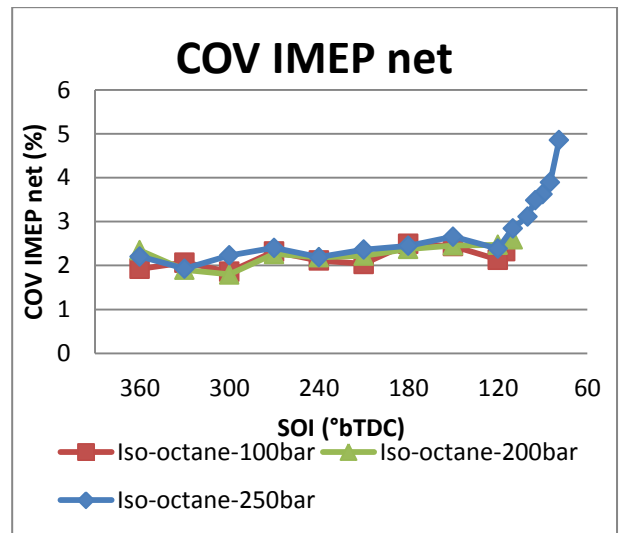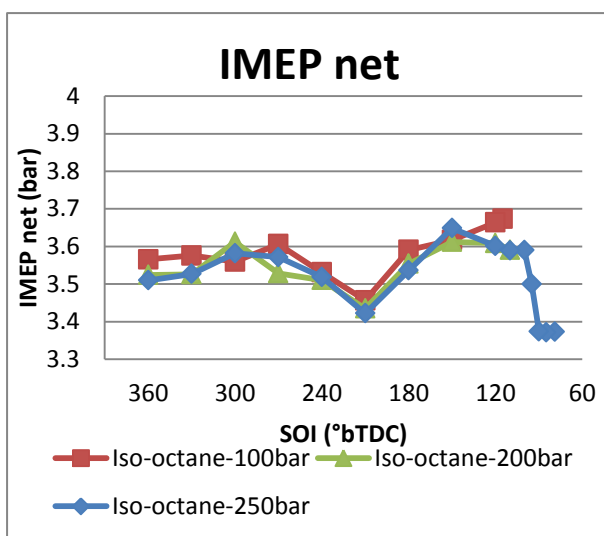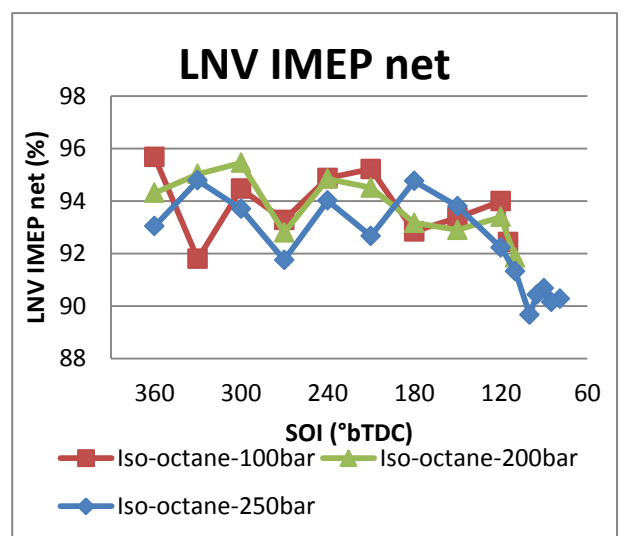
(b)

Figure 5-16: a) Gross IMEP and b) Net IMEP during SOI sweeps at varied injection pressure (iso-octane)

(b)
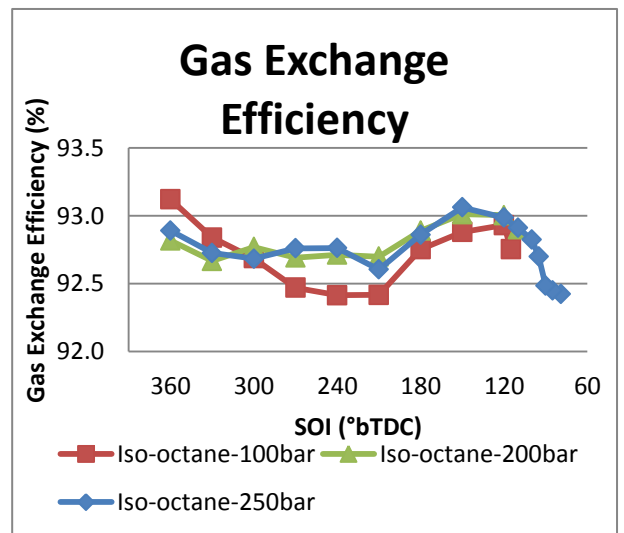
(c)

Figure 5-17: Values of a) COV b) LNV and c) Computed gas exchange efficiency during SOI sweeps at varied injection pressure (iso-octane)

Brunt and co-workers [120] performed an in-depth calculation on heat release energy from engine cylinder pressure data, the magnitude of analysis and measurement errors were also quantified using simulated and measured gasoline engine pressure data. The results revealed the calculated gross heat release was highly sensitive to the assumed ratio of specific heats (Gamma), charge to wall heat transfer as well as pressure data errors. An improved heat release model based on Rassweiler and Withrow (R&W) MFB model was developed among the work, using polytropic indices to include heat transfer and allowing the model to be better correlated with the measured data.
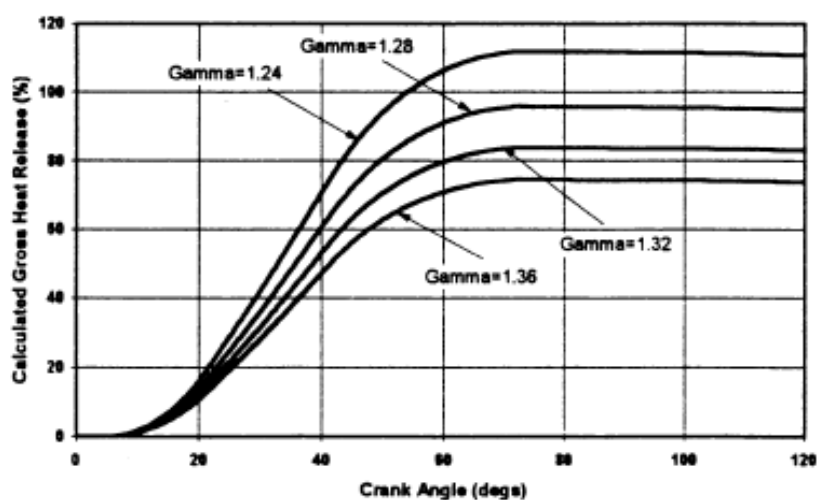
Figure 5-18: Effect of assumed Gamma on the cumulative gross heat release with a constant polytropic index of 1.35 [120]
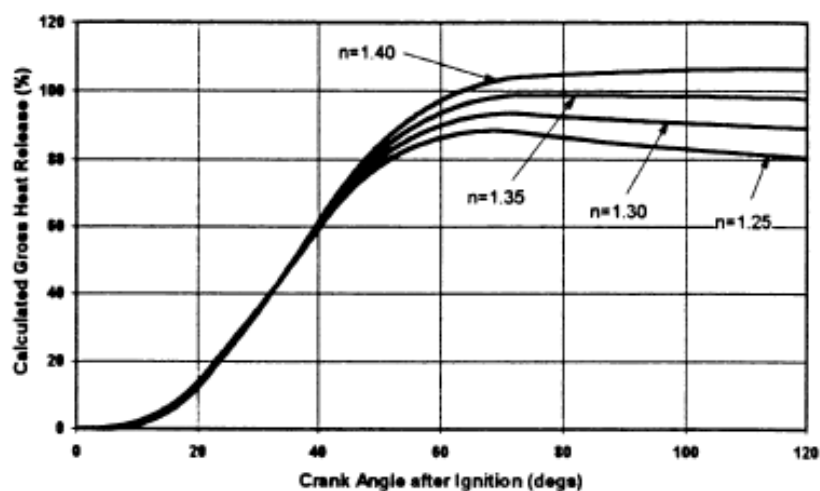
Figure 5-19: Effect of assumed polytropic index on the cumulative gross heat release with temperature dependent Gamma [120]

Figure 5-18 shows the effect of varying the assumed values of Gamma (with assumption of a constant value over the whole cycle) on the cumulative gross heat release for the case of an assumed fixed value of n=1.35. The gross heat release is near constant after combustion, as expected, irrespective of the value of Gamma assumed. Therefore the effect of Gamma is mainly of a scaling factor rather than affecting the shape of the heat release curves, the heat release is inversely proportional to Gamma. Figure 5-19 shows the effect of varying the assumed values of polytropic index (with assumption of a constant value over the whole cycle) on the cumulative gross heat release for the case of with temperature dependent Gamma. It can be derived that the polytropic index has a great effect on the heat release rate after the end of combustion, the polytropic index value is inversely proportional to thermodynamic losses (i.e. heat transfer and crevice models). The key advantage of this over the heat transfer prospective in the First Law equation is that the polytropic index can be estimated from the measured cylinder pressure data and thus the calculated values for each cycle can be used.

Shown in Figure 5-20 are corresponding mass fraction burned durations and timings. It is apparent that the optical engine suffered from a prolonged end of mass burning, particularly notable when comparing the 10-75% MFB with 10-90% MFB durations. In turn, it can be seen that the timing of the 50% MFB was relatively advanced (usually occurring at 8-10°aTDC for typical pent roof SI engines operating under stoichiometric conditions). The causes of this prolonged end-of-combustion could not be explicitly extracted from either the optical or thermodynamic data. The optical data (and above analysis of combustion stability) would insinuate that the issue is not associated with fuel-air charge stratification. One other often cited issue of optical engines is relative mass blow-by, where protection of the optical components often results in the need for relatively large piston top land and/or inter-ring volumes and/or low ring tensions. Another specific point to note is that the upper piston rings must be greased in this engine due to lack of direct continuous lubrication, which may also have adversely influenced the robustness of the sealing under some conditions. In order to qualify this effect attempts were made to operate the engine at higher loads (if higher load could not be reached then this may have indicated high blow-by/poor sealing/ring flutter due to inadequate tension or design). It was found that the engine could not be operated with Pmax above ~40 bar (IMEP

~5bar). The sealing of the engine intake system was eliminated as observed by monitoring the pressure data and spraying butane spray around the pipe connections at lower loads in an attempt to uncover uHC spikes. The above observations would indicate that the engine suffers from excessive blow-by, with considerable mass returning to the engine during the power stroke as the top land and inter-ring pressures equalised with the gas pressure in the main chamber. It is strongly recommended that the piston design be revisited in future work, with the rings potentially also changed to a material capable of running "dry" to eliminate this effect.

In accordance with the prolonged end of mass burning periods, it can be seen that the peak in-cylinder pressure dropped and retarded in timing as the SOI was retarded from 210 to 180°bTDC. As the SOI was retarded further it can be seen that fuel stratification effects came into play, with deteriorating combustion stability and load (IMEP). Overall, it can be generally concluded that elevating the fuel pressure above 100bar did not significantly influence the thermodynamic parameters determined from the in-cylinder pressure data, with similar trends observed as the injection timing was varied.
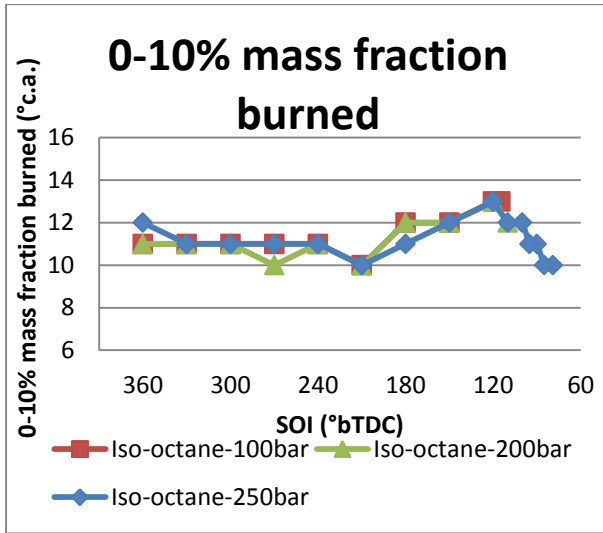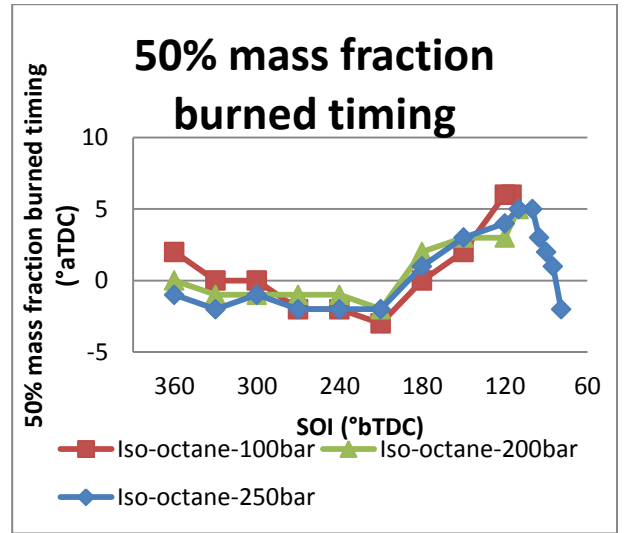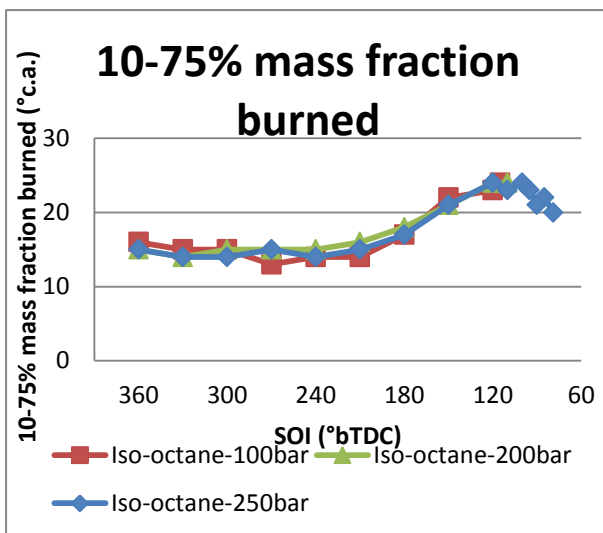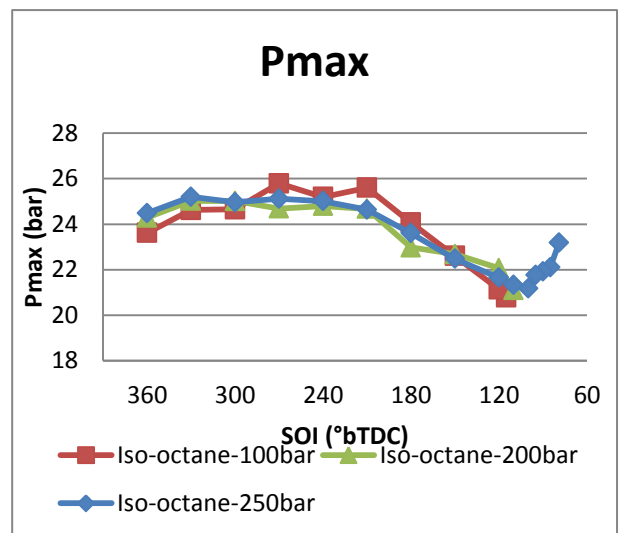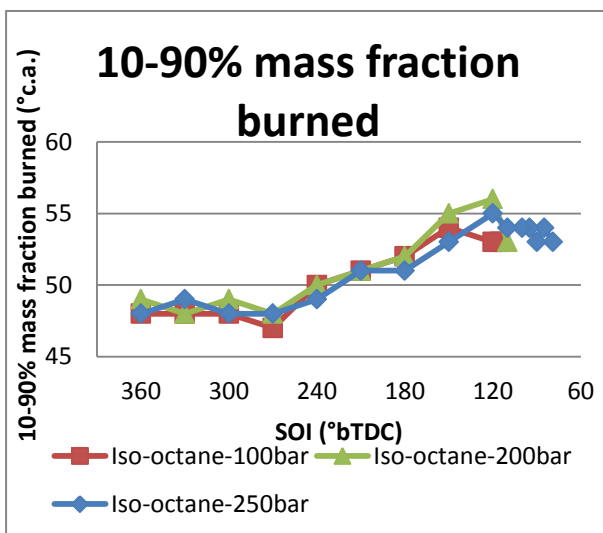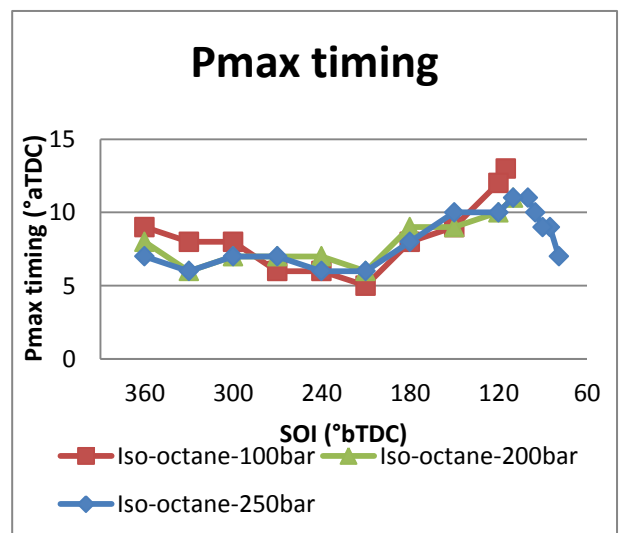
Figure 5-20: a) 0-10% MFB b) 10-75% MFB c) 10-90% MFB d) 50% MFB timing e) Pmax and f) Pmax timing during SOI sweeps at varied injection pressure (iso-octane)

Shown in Figure 5-21 are corresponding measured engine-out emissions. Prior to sampling the engine was allowed to stabilise at each site for a period of ~2 minutes. The NOx remained relatively flat until an injection timing of 210°bTDC, beyond which the values dropped off in agreement with the prolonged end of combustion discussed above. All else being equal, as the stratification of the fuel air charge increases the NOx may initially be expected to increase. However, with such prolonged end of combustion the peak burned gas temperatures will have reduced. This hypothesis is in good agreement with the increased CO emissions and ultimately higher uHC under highly retarded injection settings (both of which increase with reducing gas temperatures and increased stratification). Here, it can be concluded that the elevated fuel pressure served to reduce the rate of increase in CO and unburned hydrocarbons (uHC); with the uHC notably remaining flat throughout the sweep. This could be associated with improved atomisation of the fuel and or increased penetration into the flow field. During the compression stroke the bulk tumbling air motion spins-up as the height of the combustion chamber reduces (associated with conservation of angular momentum). Ideally this bulk tumbling air motion breaks down just prior to ignition into small scale turbulence homogeneously distributed across the bore. Such small scale turbulence is desired to wrinkle the flame early on, leading to increased unburned mass entrainment due to the high flame area. In reality some larger bulk air motions may persist (the flow inside the engine is rarely homogeneous as often treated to be so in averaged CFD simulations). If the large scale tumbling motion had not fully broken down at the time of injection but was still "spinning up" and/or breaking down, it is possible that higher injection pressure may have aided the dispersion of the fuel jets across the bulk air motion (acting in addition to the well reported influence of high injection pressure on improved fuel atomisation). Regardless, it can be concluded that the elevated pressure case serves to improve the control of the uHC under highly retarded injection conditions (despite relatively poor combustion as shown above).

Set out in Figure 5-22 are values of Filter Smoke Number (FSN) measured during the same emissions sweeps. It was concluded that the smoke is most consistently minimised with earliest injection timings. As the injection timing was retarded the smoke number generally increased slightly, with readings eventually becoming erratic at the most retarded injection timings (as the combustion stability deteriorated). In general the FSN numbers recorded are at the lower end

of the relative scale and indicate satisfactory performance of the injection targeting, with similar values reported in the literature in side DI multi-cylinder engines [71]. Overall, compared to the optical results, the mapping data is in good agreement with the prior observations, with an optimum injection timing in the range of 300-270°bTDC an acceptable setting in terms of pollutant emissions. However, in terms of thermodynamic performance (neglecting the adverse blow-by effects) the peak gas exchange efficiency was achieved with early start of injection (360°bTDC) when both the intake and exhaust valves were open. Such observations highlight the dangers in considering optical engine results alone.
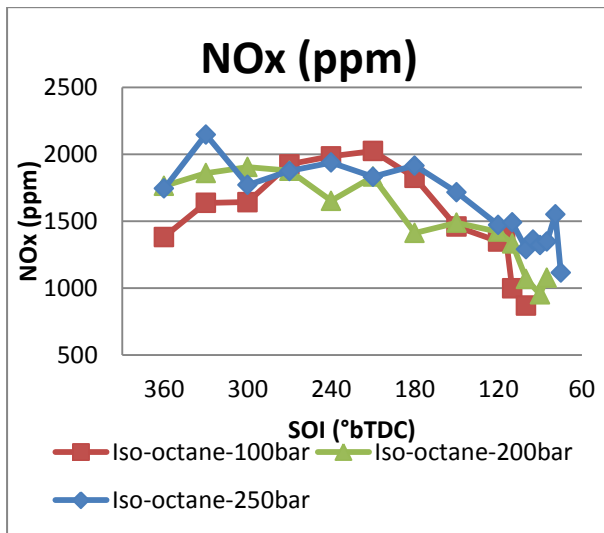
(a)
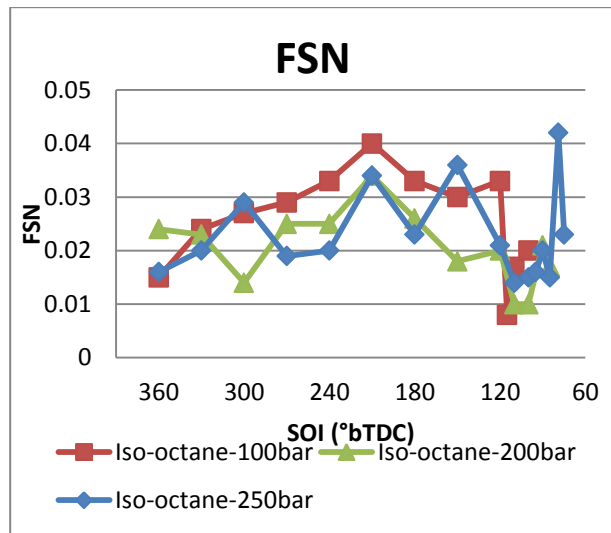
Figure 5-22: Filter Smoke Number (FSN) during SOI sweeps at varied injection pressure (iso-octane)
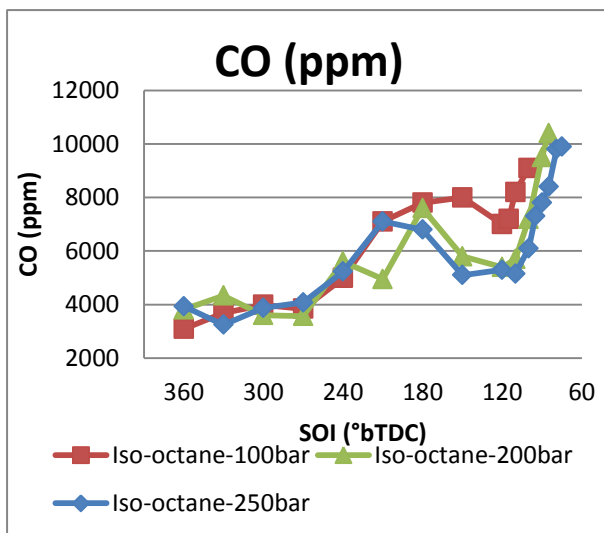
(b)
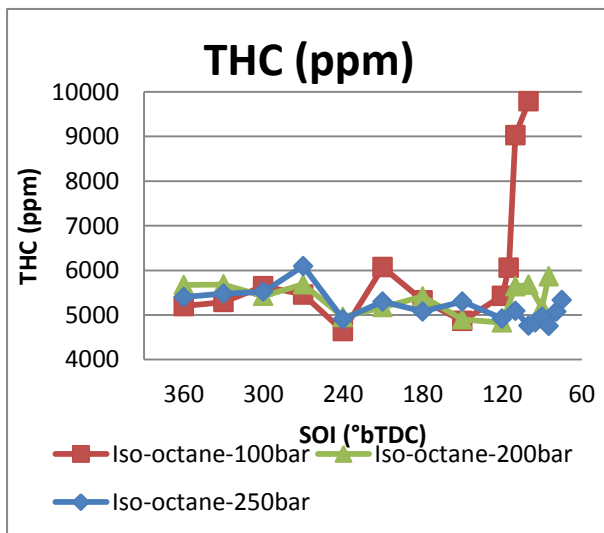
(c)

Figure 5-21: Engine-out emissions a) NOx b) CO and c) THC during SOI sweeps at varied injection pressure (iso-octane)

5.3.2 Fuel Blend Effects (100bar)

Shown in Figure 5-23, Figure 5-24 and Figure 5-25 are the results of equivalent analysis of the in-cylinder pressure data for three fuel blends with the SOI varied as before but with a fixed fuel rail injection pressure of 100bar. During these tests the spark timing was again held at 30°bTDC. For each fuel the throttle was set to achieve the target load of 3.5bar net IMEP with the fuel injection timing set to 360°bTDC. During each fuel injection timing sweep the throttle position thereafter remained fixed, with stoichiometry maintained by finite adjustment of the injector pulse width. All other engine conditions remained fixed as per the iso-octane-only experiments presented above. The IMEP and COV of IMEP values show marginal differences between the fuel blends, with initial target load met in all cases at 360°bTDC. The E10 fuel appears to be the worst performer in terms of maintaining load. Gasoline-ethanol blends are known to exhibit azeotropic behaviour, with profound effects on the vaporisation and thermodynamic properties of the blend. For example, Kar and co-workers [82] performed cycle resolved in-cylinder temperature measurements and reported that blends with less ethanol content (0-30%) tended to evaporate more readily while higher concentrations (>50%) with reduced vapour pressure did not and hence exhibited reduced "evaporative power". In IC engines varying ethanol blends exhibit highly non-linear trends in combustion, performance and emissions [71], [121]. Such trends are again observed here, with differences under the limited part-load conditions examined. Observing the gas exchange efficiency values in Figure 5-24, it is interesting to note increased performance with E85, which cannot be directly explained from the limited thermodynamic data available. During injection, the lower calorific value of ethanol leads to longer injection pulse width, with prolonged interaction with the gas exchange. The injection duration pulse widths for all three fuels under three different fuel pressures are illustrated in Table 5-4. Nonetheless it is important to emphasize that the differences observed in gas exchange were very small.

Table 5-4: Thermodynamic mapping (engine-out emissions)

Fuel	Iso-octane	E10	E85
Speed (rpm)	1200	1200	1200
IMEPn (bar)	~3.5	~3.5	~3.5
λ	1	1	1
SOI (°bTDC)	360 → 75 (30°c.a. incr. major)	360 → 75 (30°c.a. incr. major)	360 → 60 (30°c.a. incr. major)
Fuel Pressure (bar)	100 & 200 & 250	100 & 200 & 250	100 & 200 & 250
Injection Duration (ms)	0.51 & 0.40 & 0.38	0.56 & 0.42 & 0.41	0.74 & 0.59 & 0.57
Coolant Temperature (°C)	90	90	90
Oil Temperature (°C)	50	50	50
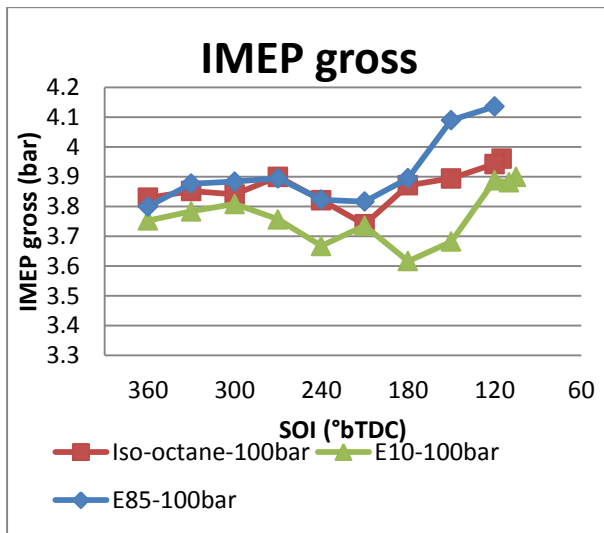
(a)
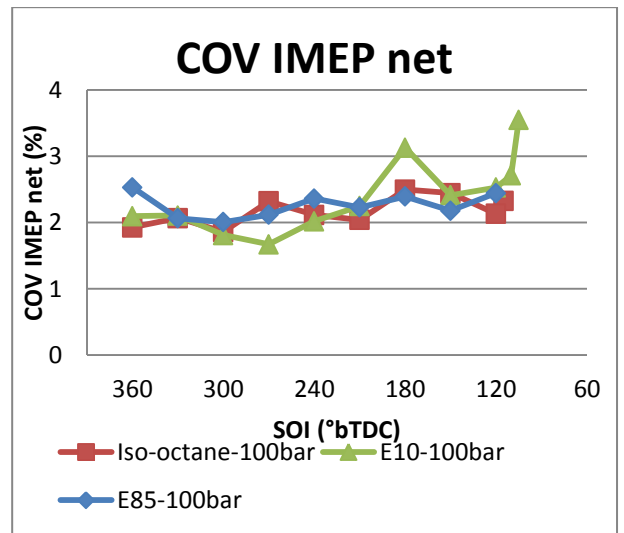
(a)
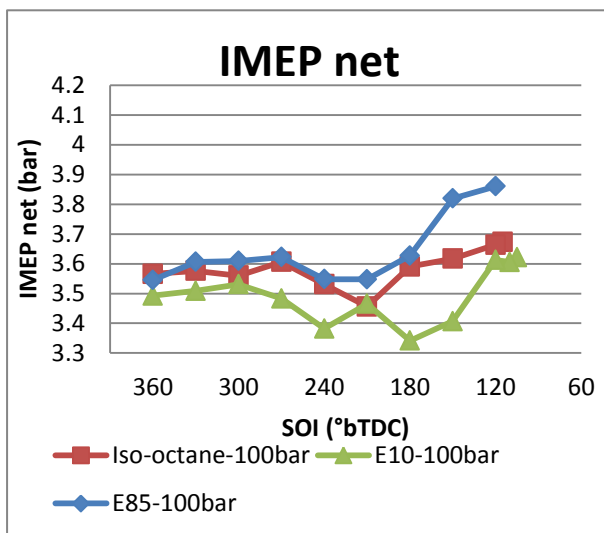
(b)
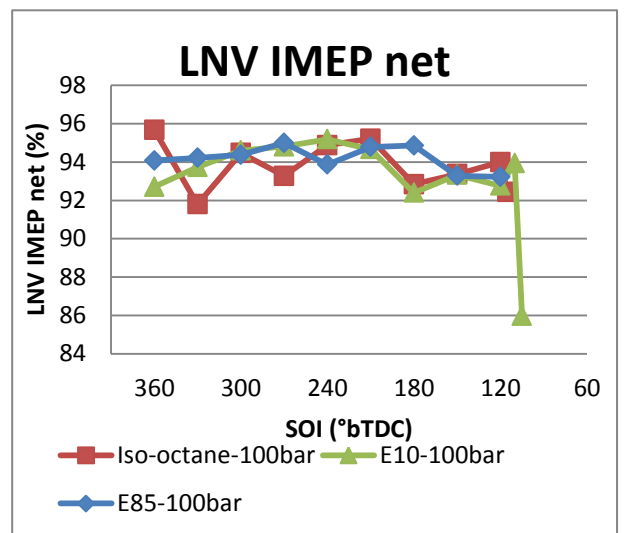
(b)

Figure 5-23: a) Gross IMEP and b) Net IMEP during SOI sweeps using different fuels (100bar)
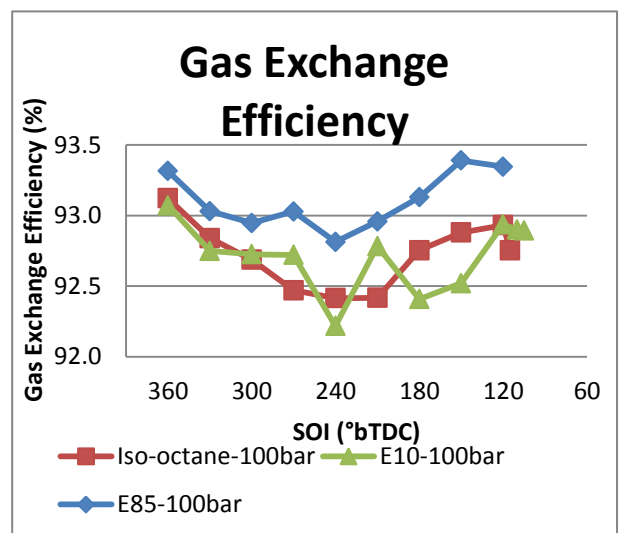
(c)

Figure 5-24: Values of a) COV b) LNV and c) Computed gas exchange efficiency during SOI sweeps using different fuels (100bar)
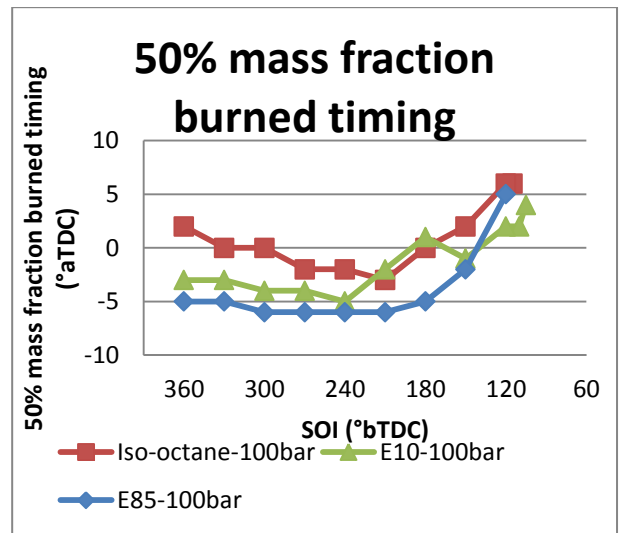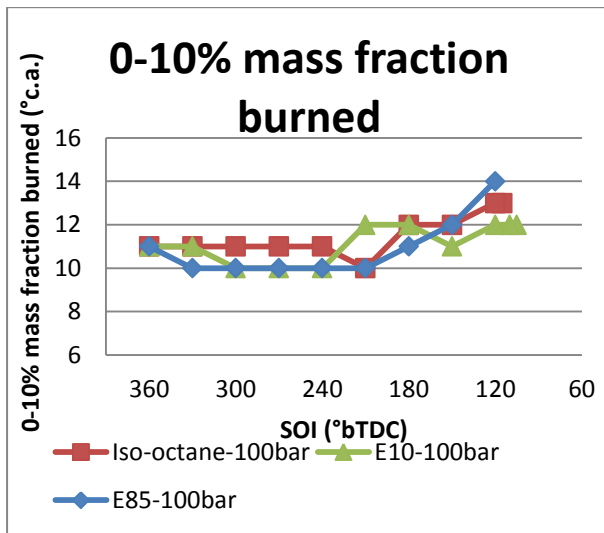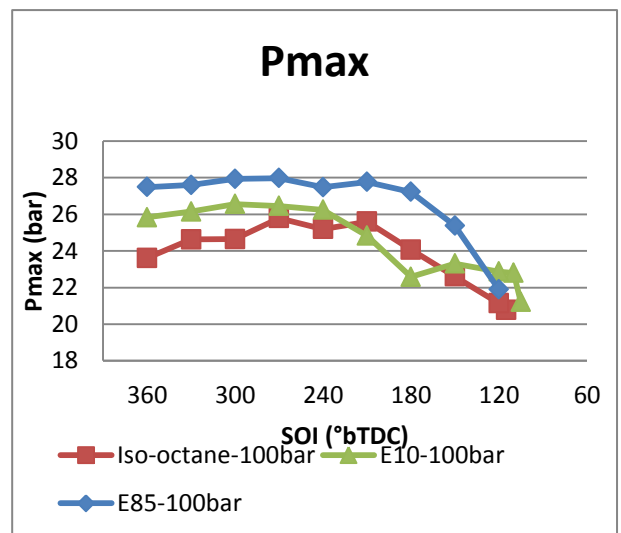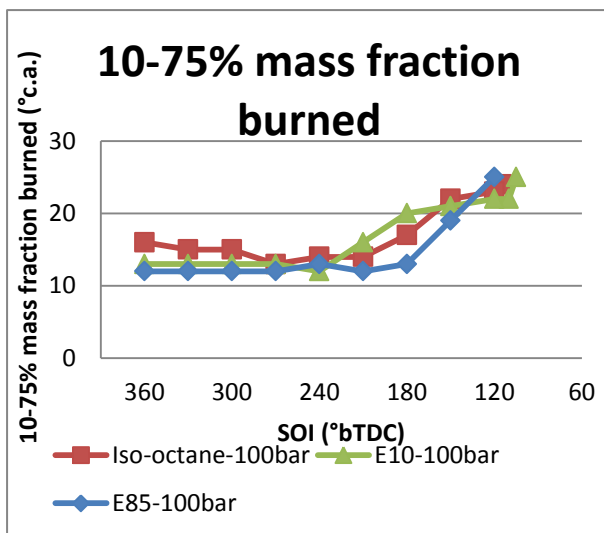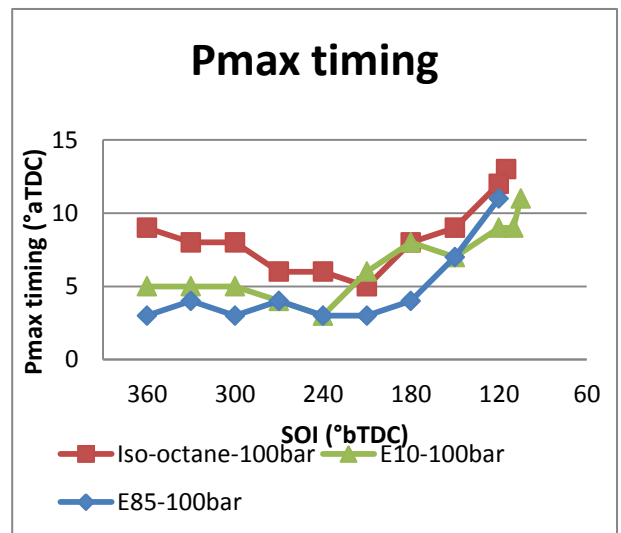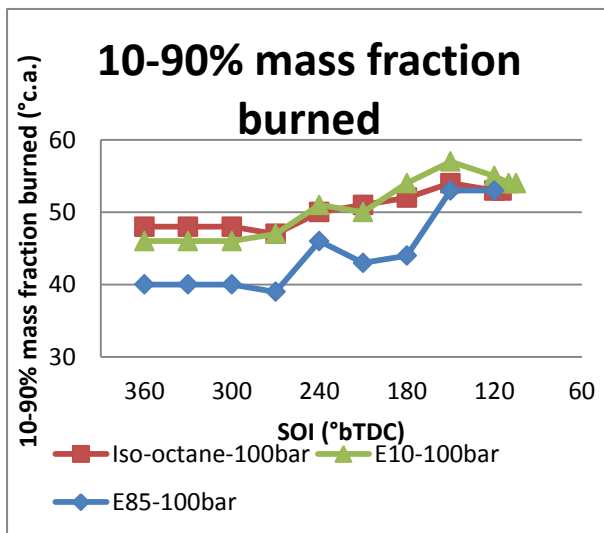
Figure 5-25: a) 0-10% MFB b) 10-75% MFB c) 10-90% MFB d) 50% MFB timing e) Pmax and f) Pmax timing during SOI sweeps using different fuels (100bar)

The 10-90% MFB duration is often referred to as the "combustion duration" and is associated with the burning period after the flame front has approached the walls (with significant entrained but unburned mass behind the flame front). Observing the mass fraction burned timings in Figure 5-25, the E85 blend exhibits a relatively fast combustion duration despite the above noted issues with blow-by. Ethanol is known to incur a higher laminar burning velocity under otherwise fixed stoichiometric conditions. In recent work at Brunel, Moxey [121] compared iso-octane, gasoline and ethanol fuels in a full bore overhead optical engine at similar part-load conditions to those employed in this study (1500rpm, 4bar IMEP, λ=1.0, MBT) albeit with port fuel injection. In his work, Moxey adopted reverse mode thermodynamic analysis to compute the unburned gas temperatures for each "average" pressure cycle. This unburned gas temperature could then be used to compute the laminar burning velocity during each "average" cycle via the burning velocity correlations of Metghalchi and Keck [122] or those of Gülder for ethanol [123]. These laminar burning velocity correlations were measured in constant volume combustion chambers over a wide range of engine-like conditions and are widely cited to be the most robust correlations available for these fuels in terms of covering a wide enough range of pressure, temperature, mixture strength and residual fraction. The predictions obtained by Moxey are set out in Figure 5-26. It was clear that ethanol exhibited the higher laminar burning velocity. It was also noted that the iso-octane exhibited a very similar laminar burning velocity profile to gasoline, which Moxey argued helped justify the use of this fuel as a pure surrogate for pump gasoline. In SI engines the burning up of the entrained mass does not occur under laminar conditions due to lack of time, where the turbulence serves to aid entrainment and mixing of the burned and unburned gases. However, the laminar burning velocity can be considered as a relative measure of the global chemical reaction rate. If the laminar burning velocity is higher, it follows that the turbulent burning will incur faster chemistry. The results for pure ethanol are in good agreement with the faster combustion observed with E85 in the currently reported thesis; where the faster chemistry of the ethanol results in a faster burn up of the mass entrained. In turn this results in advanced combustion phasing and elevated in-cylinder pressure, as evident in Figure 5-25.
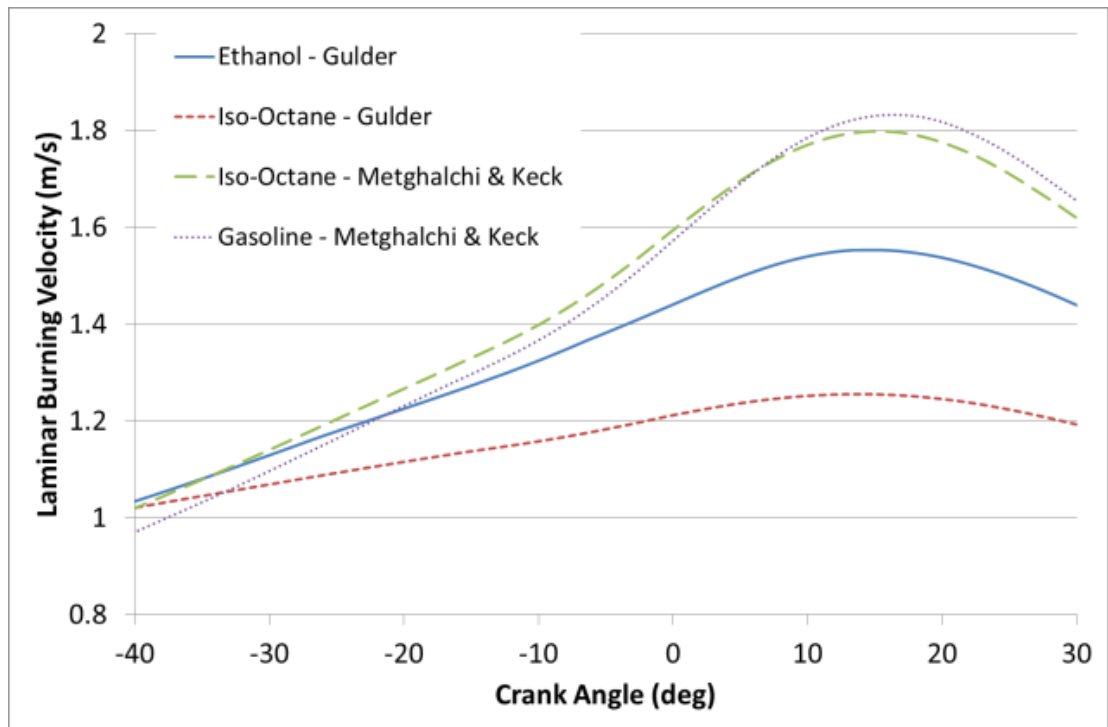
Figure 5-26: Laminar Burning Velocities for the three pure fuels [121]

Set out in Figure 5-27 and Figure 5-28 are the corresponding measurements of engine-out emissions. While NOx and uHC emissions were similar for each fuel, the E10 blend was clearly the worst performer in terms of CO, with lower combustion efficiency apparent. In terms of smoke, the observation of worse FSN with E10 but lower FSN with E85 is in good agreement with the prior observations made by Cairns and co-workers in a multi-cylinder DI engine [71]; where again the smoke was associated with the azeotropic behaviour of ethanol. Overall the results highlight the care that must be taken to ensure robust calibration in flex fuelled SI engines exposed to significant variations in ethanol content. The above observations are in good agreement with the optical work, where at earlier injection timings typical of current homogeneous DI operation, the E10 fuel performed similarly poorly if not worse than the E85 fuel. With late injection timing beyond 210°bTDC the PLIF images also indicated that the E85 fuel performed more consistently than E10.
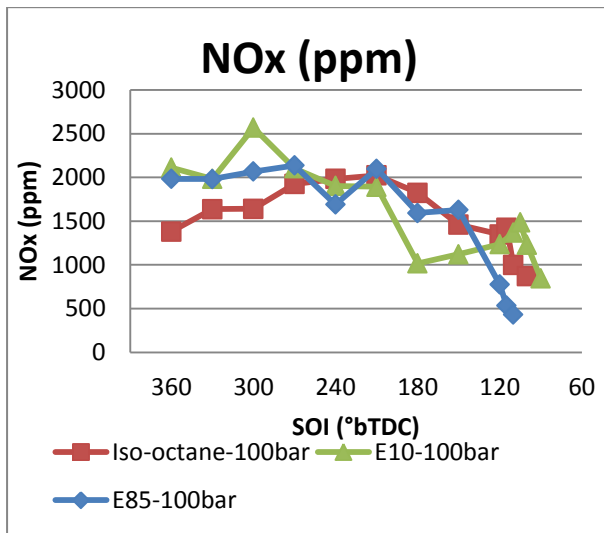
(a)
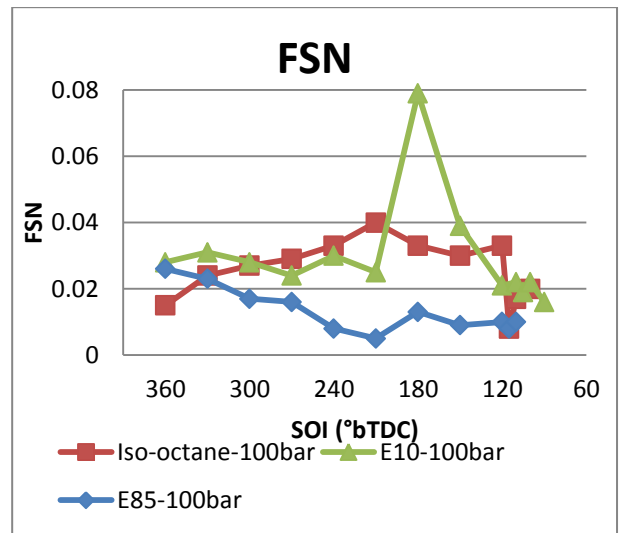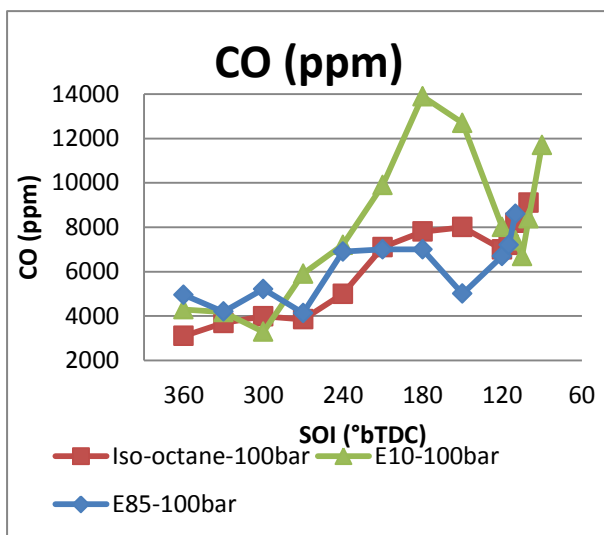
(b)
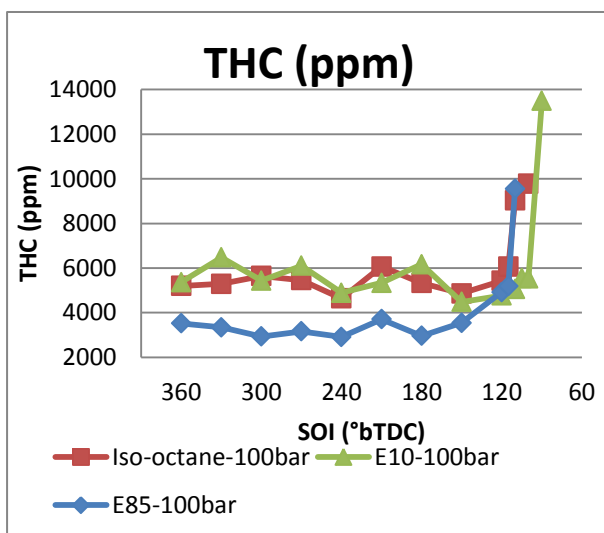
(c)

Figure 5-27: Engine-out emissions a) NOx b) CO and c) THC during SOI sweeps using different fuels (100bar)

5.3.3 Elevated Fuel Pressure Versus SOI Effects

To study the influence of elevated fuel injection pressure, the experiments were repeated at elevated fuel injection pressures of 200 and 250 bar respectively. The approach was identical to that taken above when comparing fuels. The corresponding thermodynamic results are set out in Appendix A; discounted from inclusion here for brevity given the trends are identical to those observed at 100bar. The main observed benefit was a slight reduction in CO for E10, as shown below in Figure 5-29; where the elevated fuel pressure may help to overcome the relatively poor mixture preparation with this fuel as observed in the optical work. The other engine-out emissions remained relatively insensitive to pressure, as shown below in Figure 5-29 and Figure 5-30.

Note: For complete thermodynamic data analysis and emission data of Section 5.3, please refer to Appendix A, B, C and D.
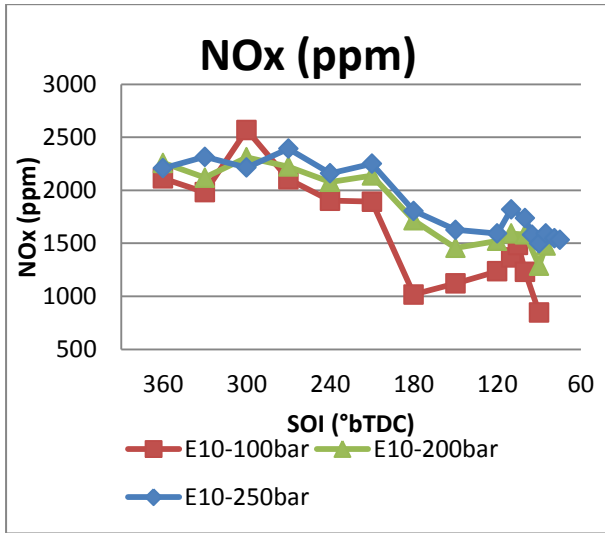
(a)
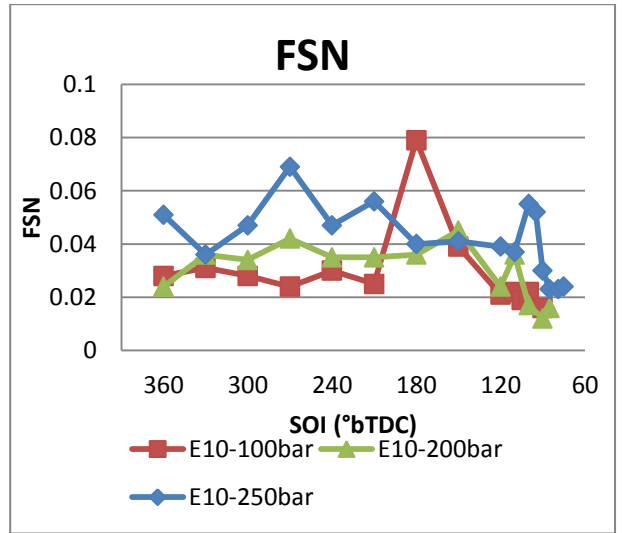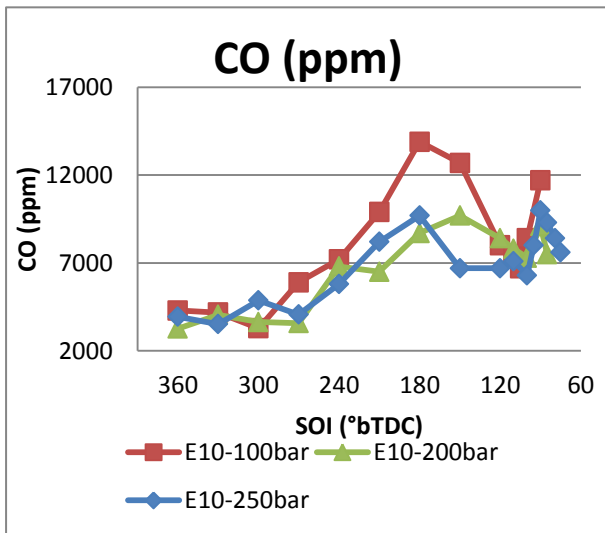
(b)
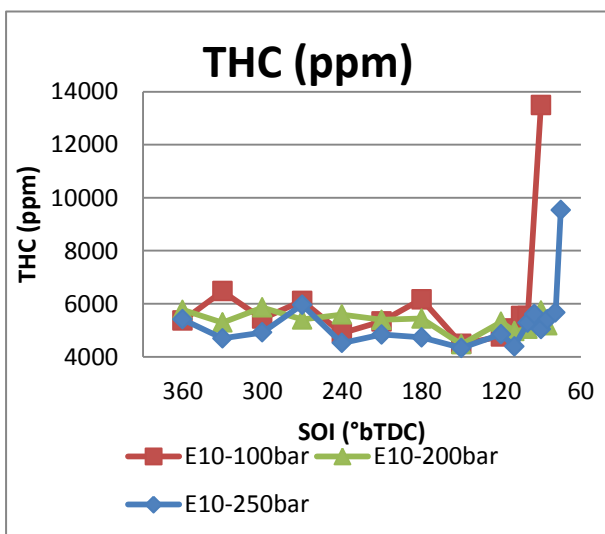
(c)

Figure 5-29: Engine-out emissions a) NOx b) CO and c) THC during SOI sweeps at varied injection pressure (E10)

Chapter 6 Conclusions & Future Work

The aim of the currently reported thesis was to improve fundamental understanding of the interactions between modern fuels and fuel injection systems in future homogeneous DISI engines, with emphasis on the potential influence of relative charge homogeneity on engine combustion, performance and emissions. The work made use of an in-house optical single cylinder engine, upgraded in this work to incorporate a new piezo DI system with geometry following injector manufacturer guidelines. Due to the apparent limitations of the optical engine design the study was limited to part-load operating conditions, typical of those encountered during cruising conditions. Optical PLIF imaging was undertaken to understand differences in the charge preparation with varying fuel injection settings and timings, with a suite of "modern" ethanol blended fuels considered. In order to corroborate these results a series of fired tests were undertaken, with in-cylinder pressure thermodynamic analysis and engine-out emissions sampling used to corroborate the findings made during the optical work.

6.1 Conclusions

The aim of the initial optical PLIF testing was to evaluate stratification in the charge in a plane below the spark plug during typical individual cycles at varied fuel injection timings and pressures with modern fuels. The three fuels examined were iso-octane, E10 and E85, all of which were all evaluated at both 100 and 200bar rail pressure over a wide range of injection timings. The following conclusions were made:

- The iso-octane baseline case presented the most homogeneous appearing charge for the typical cycles selected, with an optimum injection timing of around ~270°bTDC in good agreement with the low COV of IMEPn (~2%) observed at this timing during prior initial firing tests.

- Both E10 and E85 exhibited a higher degree of stratification, although the E10 case appeared much improved and very similar to iso-octane at the mutually (visible) optimum injection timing of 270°bTDC.

- Increasing the rail pressure from 100 to 200bar appeared to generally improve the degree of stratification for all injection timings and fuels. This elevated rail pressure resulted in reduced size of the fuel droplets hence added kinetic energy to the turbulent mixing, as droplet size is a function of pressure, the higher the fuel pressure the smaller the droplet size.

Additional statistical analysis was employed to evaluate the repeatability of these observations across 20 optical cycles captured for each fixed condition. The following additional conclusions were drawn:

- At earlier injection timings typical of current homogeneous DI operation, the E10 fuel performed similarly poorly if not worse than the E85 fuel. This was associated with the previously well reported azeotropic nature of gasoline-ethanol blends (as discussed on Page 100).

- With late injection timing beyond 210°bTDC the E85 fuel performed more consistently than E10. This improvement in repeatability of the fuel field may have been associated with higher charge temperatures aiding the evaporation of the main mass of alcohol (occurring at a fixed temperature below the vaporisation temperature of some of the constituent elements of the gasoline). This observation may have significant implications for repeatability in future stratified direct injection flex fuel concepts.

In final optical tests the effects of varying coolant temperature on fuel field repeatability were evaluated and the following conclusions made:

- Comparing iso-octane and E10, the repeatability of E10 was much worse at lower coolant temperatures due to relatively poor evaporation of the E10 fuel.

- The poorer evaporation was clearly evident when reviewing the raw images, with large droplets of liquid fuel clearly remaining within the chamber in the E10 case regardless of injection timing and all coolant temperatures measured (including fully warm).

In final work a suite of thermodynamic mapping tests were undertaken with engine-out emissions and Filter Smoke Number recorded over the same range of conditions as the optical engine tests. The glass windows were left fitted to the engine hence the results could only be considered in qualitative terms. Nonetheless, the following conclusions were made:

- During thermodynamic mapping it was noted that the combustion duration was unacceptably prolonged due to very slow end of mass burning, as evident when comparing the 10-75% and 10-90% mass fraction burned periods. This prolonged combustion was not believed to be the result of charge stratification and has been associated with relatively high blow-by in this optical engine, with considerable mass trapped within the top-land and ring pack during the main combustion event and some of this mass returning to the chamber during the power stroke. This issue limited the mapping to relatively low engine loads (<5 bar IMEP). In addition, the real time temperature can be calculated via a function of the ratio of specific heats (Gamma). In real time the calculation is too slow thus it can only be fixed by post processing, but it causes a very long calculated 90-100% burn time.

- In terms of the measured pollutant emissions, the thermodynamic mapping and emissions data were generally in good agreement with the above optical findings, with minimum CO and uHC (and therefore highest combustion efficiency) recorded in the fuel injection timing range of 300-270°bTDC.

- In terms of thermodynamic performance, a more advanced injection timing of 360-300°bTDC avoided issues with interaction with gas exchange, with a dip in IMEP noted to occur around 240-180°bTDC that was associated with reducing gas exchange efficiency. This observation highlights the dangers in considering optical results alone.

- The E10 fuel was again noted to incur slower burning and relatively poor thermodynamic performance compared to the E85 blend, which was in good agreement with prior studies of laminar burning velocity correlations for these fuels. In turn this resulted in higher CO emissions under some conditions, which were partially alleviated when the fuel injection pressure was elevated from 100 to 200bar.

- It was apparent that elevated fuel injection pressure (200bar) served to improve the control of the uHC under highly retarded injection conditions, despite deteriorating combustion stability.

6.2 Recommendations for Future Work

The currently reported thesis has provided additional insights in to some of the potential effects of ethanol blending on charge homogeneity and repeatability in DISI engines. However some issues were apparent with the experimental apparatus that prevented higher load running; originally desired to study downsized engine operation. It is strongly recommended that the optical piston design be revisited, with the reasons for apparent high blow-by investigated and resolved. This may require a new piston to be designed including reduced top-land and inter-ring volumes. The ring pack may also require revision, with higher ring tensions and or new materials adopted to allow "dry" running (albeit likely leading to the rings needing to be regarded as a consumable in line with typical dry materials such as PEEK). The current design is also limited in terms of the degree of side optical access, restricting the laser imaging plane to an area some way below the spark plug. In future work it would be ideal to fit the dry running piston to a new full optical engine liner, allowing full characterisation of the flow and fuel injection interactions from the side. An additional hardware issue was noted with poor throttle control at lower loads, with the minimum load far too high to achieve typical idle conditions. This may be associated with the intake volume downstream of the throttle and/or inability to adequately suck down the intake due to lack of a suitable enlarged plenum after the throttle. This should be revised in future work to allow a wider suite of loads to be examined.

Given the evolving nature of automotive IC engine emissions legislation and the increasing attention to particulate emissions notably linked to direct injection, future experimental work should involve particulate number measurements at key sites, with high speed fuel spray imaging also employed to better qualify the apparent poor vaporisation with "real" gasoline-ethanol blends. The work should also be repeated under full metal conditions at higher loads and comparisons made with existing multi-hole fuel injector (also designed but not adopted in this work) and port fuel injection as a baseline. It would also then be useful to consider the impact of alternative alcohols including so-called "tri-blends" of gasoline, ethanol and methanol or butanol, which could become more widely adopted if alcohol fuels can be produced more widely in the future by efficient and politically acceptable means.

References

[1]   Louis, J., "Well-to-Wheel Energy Use and Greenhouse Gas Emissions for Various Vehicle Technologies," SAE Technical Paper 2001-01-1343, 2001, doi:10.4271/2001-01-1343.

[2]   Regulation (EC) No 443/2009 of the European Parliament and of the Council of 23 April 2009, "setting emission performance standards for new passenger cars as part of the Community's integrated approach to reduce CO2 emissions from light-duty vehicles," OJ L 140, 5.6.2009, p. 1–15.

[3]   Ryan, L., Ferreira, S., Convery, F., "The impact of fiscal and other measures on new passenger car sales and CO2 emissions intensity: Evidence from Europe," *Energy Economics*, Volume 31, Issue 3, May 2009, Pages 365-374, ISSN 0140-9883, http://dx.doi.org/10.1016/j.eneco.2008.11.011.

[4]   Hao H, Liu Z, Zhao F, et al. Scenario analysis of energy consumption and greenhouse gas emissions from China's passenger vehicles [J]. Energy, 2015, 91: 151-159.

[5]   Zhao, H. (ed), "Advanced Direct Injection Combustion Engine Technologies and Development," Vol.1: Gasoline and Gas Engines, Woodhead Publishing, 2010.

[6]   Fraser, N., Blaxill, H., Lumsden, G., and Bassett, M., "Challenges for Increased Efficiency through Gasoline Engine Downsizing," SAE Int. J. Engines 2(1):991-1008, 2009, doi:10.4271/2009-01-1053.

[7]   Lecointe, B. and Monnier, G., "Downsizing a Gasoline Engine Using Turbocharging with Direct Injection," SAE Technical Paper 2003-01-0542, 2003, doi:10.4271/2003-01-0542.

[8]   Schäfer, J. and Balko, J., "High Performance Electric Camshaft Phasing System," SAE Technical Paper 2007-01-1294, 2007, doi:10.4271/2007-01-1294.

[9]   Hannibal, W., Flierl, R., Stiegler, L., and Meyer, R., "Overview of Current Continuously Variable Valve Lift Systems for Four-Stroke Spark-Ignition Engines and the Criteria for their Design Ratings," SAE Technical Paper 2004-01-1263, 2004, doi:10.4271/2004-01-1263.

[10] Sellnau, M., Kunz, T., Sinnamon, J., and Burkhard, J., "2-step Variable Valve Actuation: System Optimization and Integration on an SI Engine," SAE Technical Paper 2006-01-0040, 2006, doi:10.4271/2006-01-0040.

[11] Shimizu, K., Fuwa, N., Yoshihara, Y. and Hori, K., "The New Toyota variable Valve Timing and Lift System," Aachener Kolloquium Fahrzeug und Motorentechnik, 2007.

[12] Sandoval, D. and Heywood, J., "An Improved Friction Model for Spark-Ignition Engines," SAE Technical Paper 2003-01-0725, 2003, doi:10.4271/2003-01-0725.

[13] Blaxill, H., Reader, S., Mackay, S., Lerch, B. et al., "Development of a Friction Optimized Engine," SAE Technical Paper 2009-01-1052, 2009, doi:10.4271/2009-01-1052.

[14] Fraser, N. and Blaxill, H., "Engine Downsizing and the Application of Gasoline Direct Injection to a High Specific Output Turbocharged Engine," IMechE Fuel Economy and Engine Downsizing Conference, 2004.

[15] Lumsden, G., OudeNijeweme, D., Fraser, N., and Blaxill, H., "Development of a Turbocharged Direct Injection Downsizing Demonstrator Engine," SAE Int. J. Engines 2(1):1420-1432, 2009, doi:10.4271/2009-01-1503.

[16] Turner, J., Patel, R. and Jeffcoat, L., "Ultraboost – Improving the Fuel Economy of a Spark-Ignition Engine by 35% through Aggressive Downsizing," IMechE Downsizing Seminar, 2013.

[17] Fuerhapter, A., Piock, W., and Fraidl, G., "CSI - Controlled Auto Ignition - the Best Solution for the Fuel Consumption - Versus Emission Trade-Off?," SAE Technical Paper 2003-01-0754, 2003, doi:10.4271/2003-01-0754.

[18] Zhao, H., "Homogeneous Charge Compression Ignition (HCCI) and Controlled Auto Ignition (CAI) Combustion Engines for Automotive Industry," Woodhead Publishing Ltd & CRC Press, ISBN 184569 128 8 [ISBN-13:978 184569 128 8], 2007.

[19] Cairns, A. and Blaxill, H., "The Effects of Combined Internal and External Exhaust Gas Recirculation on Gasoline Controlled Auto-Ignition," SAE Technical Paper 2005-01-0133, 2005, doi:10.4271/2005-01-0133.

[20] Guzzella, L., Wenger, U., and Martin, R., "IC-Engine Downsizing and Pressure-Wave Supercharging for Fuel Economy," SAE Technical Paper 2000-01-1019, 2000, doi:10.4271/2000-01-1019.

[21] Wirth, M., Mayerhofer, U., Piock, W., and Fraidl, G., "Turbocharging the DI Gasoline Engine," SAE Technical Paper 2000-01-0251, 2000, doi:10.4271/2000-01-0251.

[22] Andriesse, D., "The New 1.8 1 DI Turbo-Jet Gasoline Engine from Fiat Powertrain Technologies," 17th Aachener Kolloquium Fahrzeug und Motorentechnik, 2008.

[23] Krebs, R., "The New Audi 2,0l T-FSI Motor – The First Direct Injection Turbo Gasoline Engine at Audi," 25th International Vienna Motor Symposium, 2004.

[24] Yi, J., Wooldridge, S., Coulson, G., Hilditch, J. et al., "Development and Optimization of the Ford 3.5L V6 EcoBoost Combustion System," *SAE Int. J. Engines* 2(1):1388-1407, 2009, doi:10.4271/2009-01-1494.

[25] Wieske, P., Lüddecke, B., Ewert, S., Elsäßer, A. et al., "New Concepts for Optimising Transient Torque Response and Fuel Economy of Turbocharged Gasoline Engines," 18th Aachener Kolloquium Fahrzeug und Motorentechnik, 2009.

[26] Lang, O., Geiger, J., Habermann, K., and Wittler, M., "Boosting and Direct Injection -Synergies for Future Gasoline Engines," SAE Technical Paper 2005-01-1144, 2005, doi:10.4271/2005-01-1144.

[27] Fraidl, G., Kapus, P., Prevedel, K., Fuerhapter, A., "GDI Turbo: The next Steps," 28th International Vienna Motor Symposium, 2007.

[28] Hall, D., King, D., Morgan, T., Baverstock, S. et al., "A Review of Recent Literature Investigating the Measurement of Automotive Particulate; The Relationship with Environmental Aerosol, Air Quality and Health Effects," SAE Technical Paper 982602, 1998, doi:10.4271/982602.

[29] Ericsson, P., Holmström, M., Amberntsson-Carlsson, A., Ohlson, C. et al., "Characterization of Particulate Emissions and Methodology for Oxidation of Particulates from Non-Diesel Combustion Systems," SAE Technical Paper 2008-01-1746, 2008, doi:10.4271/2008-01-1746.

[30] Price, P., Stone, R., Collier, T., and Davies, M., "Particulate Matter and Hydrocarbon Emissions Measurements: Comparing First and Second Generation DISI with PFI in Single Cylinder Optical Engines," SAE Technical Paper 2006-01-1263, 2006, doi:10.4271/2006-01-1263.

[31] Kittelson, D.B., "Engines and nanoparticles: a review," Journal of Aerosol Science, Volume 29, Issues 5–6, 1 June 1998, Pages 575-588, ISSN 0021-8502, http://dx.doi.org/10.1016/S0021-8502(97)10037-4.

[32] "Emission Standards, Cars and Light Trucks," http://www.dieselnet.com/standards/eu/ld.php, Sep. 2013.

[33] Aikawa, K., Sakurai, T., and Jetter, J., "Development of a Predictive Model for Gasoline Vehicle Particulate Matter Emissions," SAE Int. J. Fuels Lubr. 3(2):610-622, 2010, doi:10.4271/2010-01-2115.

[34] Larsen U., Johansen T., Schramm J., "Ethanol as a fuel for road transportation. Main Report, EFP06, IEA implementing Agreement on Advanced motor Fuels," 2009.

[35] Hill J., Polasky S., Nelson E., Tilman D. et al., "Climate change and health costs of air emissions from biofuels and gasoline," *Proceedings of the National Academy of Sciences of the United States of America*, vol. 106, no. 6, pp. 2077-82, Feb. 2009, doi: 10.1073/pnas.0812835106.

[36] Griffin, W., Lave, L., and MacLean, H., "Promise and Cost of Cellulosic Ethanol for the U.S. Light-Duty Fleet," SAE Technical Paper 2001-01-2474, 2001, doi:10.4271/2001-01-2474.

[37] Pearson, R., Turner, J., Eisaman, M., and Littau, K., "Extending the Supply of Alcohol Fuels for Energy Security and Carbon Reduction," SAE Technical Paper 2009-01-2764, 2009, doi:10.4271/2009-01-2764.

[38] Heywood, J. B., "Internal Combustion Engine Fundamentals," New York: McGraw-Hill, 1988.

[39] Wade, W. and Jones, C., "Current and Future Light Duty Diesel Engines and Their Fuels," SAE Technical Paper 840105, 1984, doi:10.4271/840105.

[40] Stone, R., "Introduction to Internal Combustion Engines", 4th Edition, Palgrave MacMillan, (2012)

[41] UCL WIKI, "Gas Power Cycles, Otto cycle," https://wiki.ucl.ac.uk/display/MechEngThermodyn/Gas+Power+Cycles, accessed Sep. 2015.

[42] Mechadyne International, "Part Load Pumping Losses in an SI Engine," http://www.mechadyne-int.com/vva-reference/part-load-pumping-losses-si-engine, accessed Sep. 2015.

[43] Bech, A., Shayler, P., and McGhee, M., "The Effects of Cylinder Deactivation on the Thermal Behaviour and Performance of a Three Cylinder Spark Ignition Engine," SAE Int. J. Engines 9(4):1999-2009, 2016, doi:10.4271/2016-01-2160.

[44] B.B. Dally, E. Riesmeier, N. Peters, Effect of fuel mixture on moderate and intense low oxygen dilution combustion, Combustion and Flame, Volume 137, Issue 4, June 2004, Pages 418-431, ISSN 0010-2180

[45] Nose, H., Inoue, T., Katagiri, S., Sakai, A. et al., "Fuel Enrichment Control System by Catalyst Temperature Estimation to Enable Frequent Stoichiometric Operation at High Engine Speed/Load Condition," SAE Technical Paper 2013-01-0341, 2013, doi:10.4271/2013-01-0341.

[46] Taylor, J., Fraser, N., and Wieske, P., "Water Cooled Exhaust Manifold and Full Load EGR Technology Applied to a Downsized Direct Injection Spark Ignition Engine," SAE Int. J. Engines 3(1):225-240, 2010, doi:10.4271/2010-01-0356.

[47] König, G., Maly, R., Bradley, D., Lau, A. et al., "Role of Exothermic Centres on Knock Initiation and Knock Damage," SAE Technical Paper 902136, (1990)

[48] Pan, J. and Sheppard, C., "A Theoretical and Experimental Study of the Modes of End Gas Auto-Ignition Leading to Knock in SI Engines," SAE Technical Paper 942060, (1994)

[49] Dahnz, C., Han, K., Spicher, U., Magar, M. et al., "Investigations on Pre-Ignition in Highly Supercharged SI Engines," SAE Int. J. Engines 3(1):214-224, (2010)

[50] G.T. Kalghatgi, D. Bradley, "Pre-ignition and 'Super-Knock' in turbo-charged spark-ignition engines," Int J Engine Res, 13 (4) (2012), pp. 399–414

[51] Kulzer, A., Christ, A., Rauscher, M., Sauer, C. et al., "Thermodynamic Analysis and Benchmark of Various Gasoline Combustion Concepts," SAE Technical Paper 2006-01-0231, 2006, doi:10.4271/2006-01-0231.

[52] Cairns, A. , Fraser, N. , Lumsden, G. , Irlam, G. and Blaxill, H. :   'Low Cost Solutions for Improved Fuel Economy in Gasoline Engines' , GLOBAL POWERTRAIN CONGRESS. DETROIT, (2005).

[53] Kramer, U. and Phlips, P., "Phasing Strategy for an Engine with Twin Variable Cam Timing," SAE Technical Paper 2002-01-1101, 2002, doi:10.4271/2002-01-1101.

[54] Crawford, A., Ellis, G., Fraser, N., Steeples, B. et al., "Combining High Performance with Euro IV Capability in a Naturally Aspirated Production Engine," SAE Technical Paper 2002-01-0335, 2002, doi:10.4271/2002-01-0335.

[55] Shayler, P. and Alger, L., "Experimental Investigations of Intake and Exhaust Valve Timing Effects on Charge Dilution by Residuals, Fuel Consumption and Emissions at Part Load," SAE Technical Paper 2007-01-0478, 2007, doi:10.4271/2007-01-0478.

[56] Cairns, A., Blaxill, H., and Irlam, G., "Exhaust Gas Recirculation for Improved Part and Full Load Fuel Economy in a Turbocharged Gasoline Engine," SAE Technical Paper 2006-01-0047, 2006, doi:10.4271/2006-01-0047.

[57] Cairns, A., Fraser, N., and Blaxill, H., "Pre Versus Post Compressor Supply of Cooled EGR for Full Load Fuel Economy in Turbocharged Gasoline Engines," SAE Technical Paper 2008-01-0425, 2008, doi:10.4271/2008-01-0425.

[58] Wirth, M., Zimmermann, D., Friedfeldt, R., Caine, J., Schamel, A., Davies, M., Peirce, G., Storch, A., Riese-Muller, K., Gansert, K.P., Pilgram, G., Ortmann, R., Wurfel, G. and Gerhardt, J.:"A Cost Optimised Spray Guided Direct Injection System for Improved Fuel Economy", IMechE Fuel Economy and Engine Downsizing Conference, (2004).

[59] Cairns, A. and Sheppard, C., "Cyclically Resolved Simultaneous Flame and Flow Imaging in a SI Engine," SAE Technical Paper 2000-01-2832, 2000, doi:10.4271/2000-01-2832.

[60] Gillespie, L., Lawes, M., Sheppard, C., and Woolley, R., "Aspects of Laminar and Turbulent Burning Velocity Relevant to SI Engines," SAE Technical Paper 2000-01-0192, 2000, doi:10.4271/2000-01-0192.

[61] Schmidt, L., Seabrook, J., Stokes, J., Ahmad Zuhdi, M. et al., "Multiple Injection Strategies for Improved Combustion Stability under Stratified Part Load Conditions in a Spray Guided Gasoline Direct Injection (SGDI) Engine," SAE Technical Paper 2011-01-1228, 2011, doi:10.4271/2011-01-1228.

[62] Huber, R., Klumpp, P., and Ulbrich, H., "Dynamic Analysis of the Audi Valvelift System," *SAE Int. J. Engines* 3(1):839-849, 2010, doi:10.4271/2010-01-1195.

[63] Gottschalk, W., Lezius, U., and Mathusall, L., "Investigations on the Potential of a Variable Miller Cycle for SI Knock Control," SAE Technical Paper 2013-01-1122, 2013, doi:10.4271/2013-01-1122.

[64] Schamel, A., Ford Forschungszentrum, Aachen; Dr. M. Scheidt, Schaeffler AG, Herzogenaurach; Dipl.-Ing. C. Weber, Ford Werke GmbH, Cologne; Dr.

H. Faust, LuK GmbH & Co. KG, Bühl. "Is Cylinder Deactivation a Viable Option for a Downsized 3-Cylinder Engine?" 36th International Vienna Motor Symposium, (2015)

[65] Price, C., Hamzehloo, A., Aleiferis, P., and Richardson, D., "Aspects of Numerical Modelling of Flash-Boiling Fuel Sprays," SAE Technical Paper 2015-24-2463, 2015, doi:10.4271/2015-24-2463.

[66] Zhao, F., Lai, M., and Harrington, D., "A Review of Mixture Preparation and Combustion Control Strategies for Spark-Ignited Direct-Injection Gasoline Engines," SAE Technical Paper 970627, 1997, doi:10.4271/970627.

[67] Price, P., Twiney, B., Stone, R., Kar, K. et al., "Particulate and Hydrocarbon Emissions from a Spray Guided Direct Injection Spark Ignition Engine with Oxygenate Fuel Blends," SAE Technical Paper 2007-01-0472, 2007, doi:10.4271/2007-01-0472.

[68] Graskow, B., Kittelson, D., Abdul-Khalek, I., Ahmadi, M. et al., "Characterization of Exhaust Particulate Emissions from a Spark Ignition Engine," SAE Technical Paper 980528, 1998, doi:10.4271/980528.

[69] Kittelson, D.B., "Ultrafine Particle Formation Mechanisms," SCAQMD Conference on Ultrafine Particles: The Science, Technology and Policy Issues, April 30-May 2, 2006.

[70] Li, W., Collins, J., Norbeck, J., Cocker, D. et al., "Assessment of Particulate Matter Emissions from a Sample of In-Use ULEV and SULEV Vehicles," SAE Technical Paper 2006-01-1076, 2006, doi:10.4271/2006-01-1076.

[71] Cairns, A., Stansfield, P., Fraser, N., Blaxill, H. et al., "A Study of Gasoline-Alcohol Blended Fuels in an Advanced Turbocharged DISI Engine," SAE Int. J. Fuels Lubr. 2(1):41-57, 2009, doi:10.4271/2009-01-0138.

[72] Allocca, L., Catapano, F., Montanaro, A., Sementa, P. et al., "Study of E10 and E85 Effect on Air Fuel Mixing and Combustion Process in Optical Multicylinder GDI Engine and in a Spray Imaging Chamber," SAE Technical Paper 2013-01-0249, 2013, doi:10.4271/2013-01-0249.

[73] Storey, J., Barone, T., Norman, K., and Lewis, S., "Ethanol Blend Effects On Direct Injection Spark-Ignition Gasoline Vehicle Particulate Matter Emissions," SAE Int. J. Fuels Lubr. 3(2):650-659, 2010, doi:10.4271/2010-01-2129.

[74] He, X., Ireland, J., Zigler, B., Ratcliff, M. et al., "The Impacts of Mid-level Biofuel Content in Gasoline on SIDI Engine-out and Tailpipe Particulate

Matter Emissions," SAE Technical Paper 2010-01-2125, 2010, doi:10.4271/2010-01-2125.

[75] de Francqueville, L., "Effects of Ethanol Addition in RON 95 Gasoline on GDI Stratified Combustion," SAE Technical Paper 2011-24-0055, 2011, doi:10.4271/2011-24-0055.

[76] Chen L., Stone R., and Richardson D., "A study of mixture preparation and PM emissions using a direct injection engine fuelled with stoichiometric gasoline / ethanol blends," Fuel, vol. 96, pp. 120-130, 2012, doi: 10.1016/j.fuel.2011.12.070.

[77] Tongroon, M., "Combustion characteristics and in-cylinder process of CAI combustion with alcohol fuels," Ph.D. thesis, School of Engineering and Design, Brunel University, 2010.

[78] Anbari Attar, M., "Development and optimisation of two-line planar laser induced fluorescence technique for combustion measurements," Ph.D. thesis, School of Engineering and Design, Brunel University, 2012.

[79] Coates, B., "Investigation of engine design parameters on the efficiency and performance of the high specific power downsized SI engine," Ph.D. thesis, School of Engineering and Design, Brunel University, 2012.

[80] Skogsberg, M., Dahlander, P., and Denbratt, I., "Spray Shape and Atomization Quality of an Outward-Opening Piezo Gasoline DI Injector," SAE Technical Paper 2007-01-1409, 2007, doi:10.4271/2007-01-1409.

[81] Rothamer, D., Snyder, J., Hanson, R., and Steeper, R., "Two-Wavelength PLIF Diagnostic for Temperature and Composition," SAE Int. J. Fuels Lubr. 1(1):520-533, 2009, doi:10.4271/2008-01-1067.

[82] Kar, K., Last, T., Haywood, C., and Raine, R., "Measurement of Vapor Pressures and Enthalpies of Vaporization of Gasoline and Ethanol Blends and Their Effects on Mixture Preparation in an SI Engine," *SAE Int. J. Fuels Lubr.* 1(1):132-144, 2009, doi:10.4271/2008-01-0317.

[83] Measures, R., M. (1984) Laser Remote Sensing. New York: John Wiley.

[84] Long, D., A. (1977) Raman Spectroscopy. New York: McGraw-Hill.

[85] Bechtel, J., H. (1979) 'Temperature Measurements of the Hydroxyl Radical and Molecular Nitrogen in Premixed, Laminar Flames by Laser Techniques' Applied Optics 18:2100.

[86] Anderson, W., R., Decker, L., J., Kotlar, A., J. (1982) 'Temperature profile of a Stoichiometric CH4/N2O Flame from Laser Excited Fluorescence Measurements on OH', Combustion and Flame 48: 179.

[87] Roller, A., Paul, A., Decker, M., Sick, V. et al. (1995) 'Non-intrusive Temperature Measurements during the Compression Phase of a DI Diesel Engine', SAE Technical Paper 952461.

[88] Laurendeau, N., M. (1988) 'Temperature Measurements by Light-scattering Methods', Progress in Energy and Combustion Science, Vol. 14, Issue 2, pp. 147-170.

[89] Kaminski, C., F., Engström, J., Aldén, M. (1998) 'Quasi-instantaneous Two-Dimensional Temperature Measurements in a Spark Ignition Engine Using 2-line Atomic Fluorescence', Proc. Comb Inst., 27:85-93.

[90] Engström, J., Kaminski, C., Aldén, M., Josefsson, G. et al. (1999) 'Experimental Investigations of Flow and Temperature Fields in an SI Engine and Comparison with Numerical Analysis', SAE Technical Paper 1999-01-3541.

[91] Felton, P., G., Mantzaras, J., Bomse, D., S., Woodin, R., L. (1988) 'Initial Two-Dimensional Laser Induced Fluorescence Measurements of OH Radicals in an Internal Combustion Engine', SAE paper 881633.

[92] Schipperijn, F., W., Nagasaka, R., Sawyer, R., F., Green, R., M. (1988) 'Imaging of Engine Flow and Combustion Processes', SAE paper 881631.

[93] Fansler, T., D., French, D., T., Drake, M., C. (1995) 'Fuel Distributions in a Firing Direct-Injection Spark-Ignition Engine Using Laser-Induced Fluorescence Imaging', SAE Paper 950110.

[94] Winklhofer, E., Philipp, H., Fraidl, G., Fuchs, H. (1993) 'Fuel and Flame Imaging in SI Engines', SAE Paper 930871.

[95] Reboux, J., Puechberty, D. (1994) 'A New Approach of PLIF Applied to Fuel/Air Ratio Measurement in the Compressive Stroke of an Optical SI Engine' SAE technical paper series No. 941988.

[96] Lozano, A. (1992) 'Laser-Excited Luminescent Tracers for Planar Concentration Measurements in Gaseous Jets', Ph.D. dissertation, Stanford University.

[97] Lozano, A., Yip, B., Hanson, R., K. (1992) 'Acetone - a Tracer For Concentration Measurements in Gaseous Flows by Planar Laser-induced Fluorescence', Experiments In Fluids, 13(6):369-376.

[98] Bazile, R., Stepowski, D. (1995) 'Measurements of Vaporized and Liquid Fuel Concentration Fields in a Burning Spray Jet of Acetone Using Planar Laser-induced Fluorescence', Experiments in Fluids, 20(1):1-9.

[99] King, G., F., Lucht, R., P., Dutton, J., C. (1997) 'Quantitative Dual-tracer Planar Laser-induced Fluorescence Measurements of Molecular Mixing', Optics Letters, 22(9):633-5.

[100] Marro, M., A., T., Miller, J., H. (1998) 'Acetone Fluorescence as a Conserved Scalar Marker in a Laminar Methane Air Diffusion Flame', Combustion Science and Technology, 140(1-6):13.

[101] Su, L., K., Clemens, N., T., (1999) 'Planar Measurements of the Full Three-Dimensional Scalar Dissipation Rate in Gas-phase Turbulent Flows', Experiments in Fluids, 27(6):507-21.

[102] Barreras, F., Lozano, A., Yates, A., J., Dopazo, C. (1999) 'The Structure of Subsonic Air Wakes Behind a Flat Plate', Experiments in Fluids, 26(5):478-80.

[103] Bryant, R., Driscoll, J., F. (2000) 'Acetone Laser Induced Fluorescence for Low Pressure, Low Temperature Flow Visualization', Experiments in Fluids, 28:417-476.

[104] A. Arnold, A. Buschmann, B Cousyn, M. Decker, F. Vannobel, V. Sick and J. Wolfrum, Simultaneous Imaging of Fuel and Hydroxyl Radicals in an In-Line Four Cylinder SI Engine, SAE Technical paper 932696, 1993.

[105] M. Berckmüller, N. P. Tait, R. D. Lockett, D. A. Greenhalgh, K. Ishii, Y. Urata, H. Umiyama and K. Yoshida, In-Cylinder Crank-Angle-Resolved Imaging of Fuel Concentration in a Firing Spark-Ignition Engine Using Planar Laser-Induced Fluorescence, Twenty-Fifth Symposium (International) on Combustion, pp. 151-156, 1994.

[106] Lide D., R. (ed.) (1999) CRC Handbook of Chemistry and Physics, 80th ed., CRC Press.

[107] Grossmann, F., Monkhouse, P., Ridder, M., Sick, V., Wolfrum, J. (1996) 'Temperature and Pressure Dependences of the Laser-Induced Fluorescence of Gas-Phase Acetone and 3-Pentanone', Applied Physics B 62, 249-253.

[108] Einecke S., Sick., V. (1998) 'Two-Dimensional Temperature Measurements in an SI Engine Using Two-line Tracer LIF', SAE Technical Paper, 982468.

[109] Einecke, S., Schulz, C, Sick, V. (2000) 'Measurement of Temperature, Fuel Concentration and Equivalence Ratio Fields Using Tracer LIF in IC Engine Combustion', Applied Physics B-Lasers and Optics, 71(5):717-723.

[110] Strand, T., E., Rothamer, D., A., Ghandhi, J., B. (2001) 'Flame Structure Visualization of Stratified Combustion in a DISI Engine via PLIF', SAE Paper 2001-01-3649.

[111] Kakuho, A., Nagamine, M., Amenomori, Y., Urushihara, T., Itoh, T. (2006) 'In-cylinder Temperature Distribution Measurement and its Application to HCCI Combustion', SAE Paper 2006-01-1202.

[112] Rothamer, D., A., Snyder, J., A., Hanson, R., K., Steeper, R., R. (2010) 'Optimization of a tracer-based PLIF diagnostic for simultaneous imaging of EGR and temperature in IC engines', Applied Physics B 99: 371-384.

[113] Snyder, J., A., Hanson, R., K., Fitzgerald, R., P., Steeper, R., R. (2009) 'Dual-Wavelength PLIF Measurements of Temperature and Composition in an Optical HCCI Engine with Negative Valve Overlap', SAE Int. J. Engines, 2009-01-0661.

[114] Rothamer, D., A., Snyder, J., A., Hanson, R., K., Steeper, R., R., Fitzgerald, R., P. (2009) 'Simultaneous Imaging of Exhaust Gas Residuals and Temperature During HCCI Combustion', Proceedings of Combustion Institute 32 2869-2876.

[115] Snyder, J., Dronniou, N., Dec J., Hanson, R., K. (2011) 'PLIF Measurements of Thermal Stratification in an HCCI Engine under Fired Operation', SAE Int. J. Engines, 2011-01-1291.

[116] Dronniou, N., Dec, J. (2012) 'Investigating the Development of Thermal Stratification from the Near-Wall Regions to the Bulk-Gas in an HCCI Engine with Planar Imaging Thermometry', SAE Int. J. Engines 5(3):1046-1074.

[117] Johansson, B., Neij, H., Aid,n, M., and Juhlin, G., "Investigations of the Influence of Mixture Preparation on Cyclic Variations in a SI-Engine, Using Laser Induced Fluorescence," SAE Technical Paper 950108, 1995, doi:10.4271/950108.

[118] Stansfield, P., Bisordi, A., OudeNijeweme, D., Williams, J. et al., "The Performance of a Modern Vehicle on a Variety of Alcohol-Gasoline Fuel Blends," SAE Int. J. Fuels Lubr. 5(2):813-822, 2012, doi:10.4271/2012-01-1272.

[119] Leach, F., Stone, R., Fennell, D., Hayden, D., Richardson, D., & Wicks, N. (2017). Predicting the particulate matter emissions from spray-guided gasoline direct-injection spark ignition engines. *Proceedings of the*

Institution of Mechanical Engineers, Part D: Journal of Automobile Engineering, *231*(6), 717-730.

[120] Brunt, M., Rai, H., and Emtage, A., "The Calculation of Heat Release Energy from Engine Cylinder Pressure Data," SAE Technical Paper 981052, 1998, doi:10.4271/981052.

[121] Moxey, B., Cairns, A., and Zhao, H., "A Study of Turbulent Flame Development with Ethanol Fuels in an Optical Spark Ignition Engine," SAE Technical Paper 2014-01-2622, 2014, doi:10.4271/2014-01-2622.

[122] Metghalchi, M. and Keck, J. C., "Burning Velocities of Mixtures of Air with Methanol, Iso-Octane and Indolene at High Temperature and Pressure," Combustion and Flame, Vol. 48, pp. 191-210, 1982.

[123] Gülder, Ö. L., "Burning Velocities of Ethanol-Isooctane Blends," Combustion and Flame, Vol. 56, pp. 261-168, 1984.

Appendix A   Fuel Pressure Versus SOI Effects (E10)

(a)

(a)
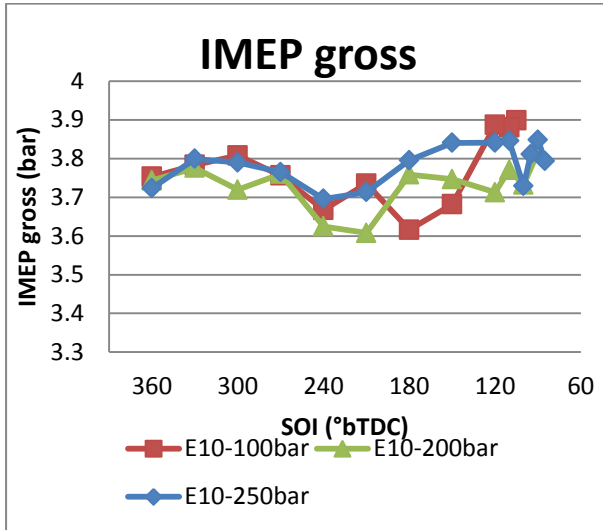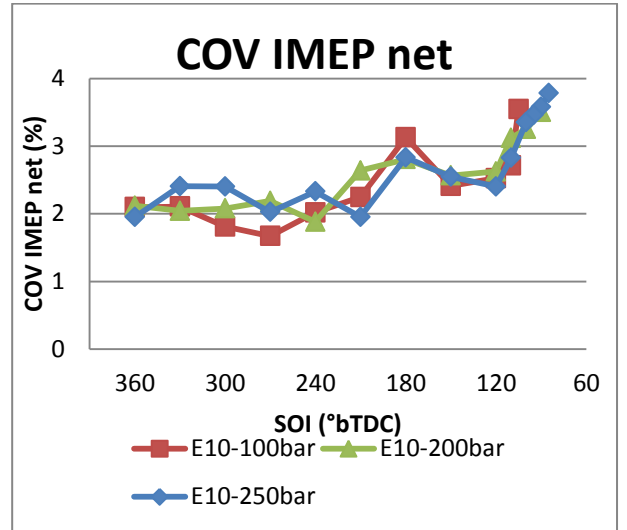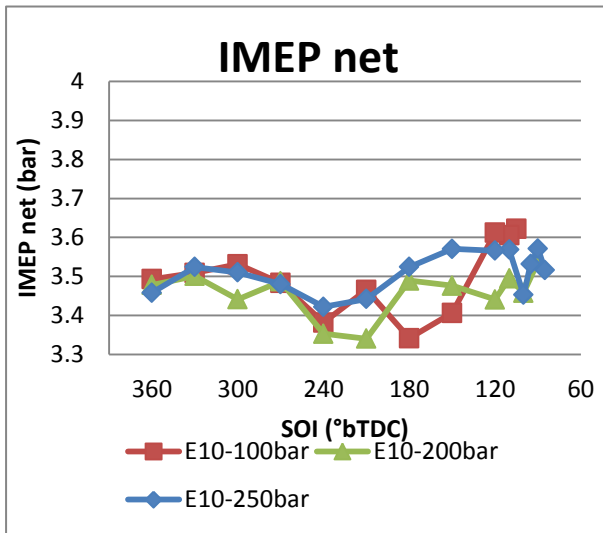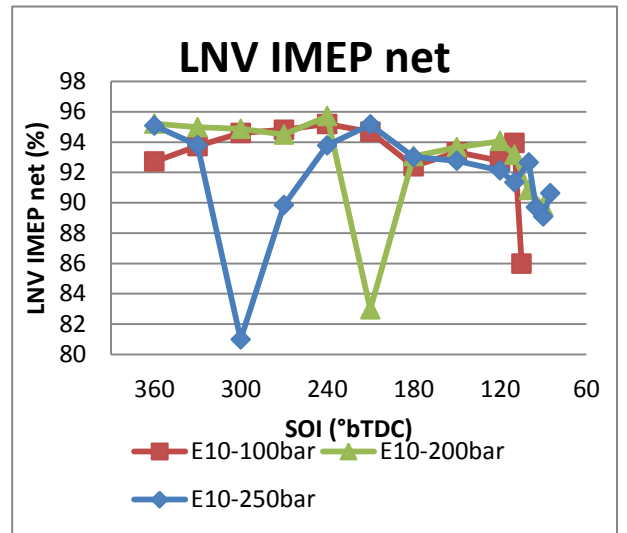
(b)

Figure A 1: a) Gross IMEP and b) Net IMEP during SOI sweeps at varied injection pressure (E10)

(b)
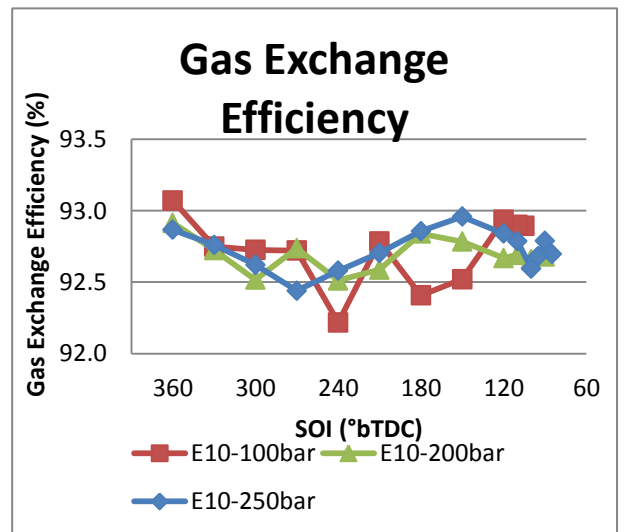
(c)

Figure A 2: Values of a) COV b) LNV and c) Computed gas exchange efficiency during SOI sweeps at varied injection pressure (E10)
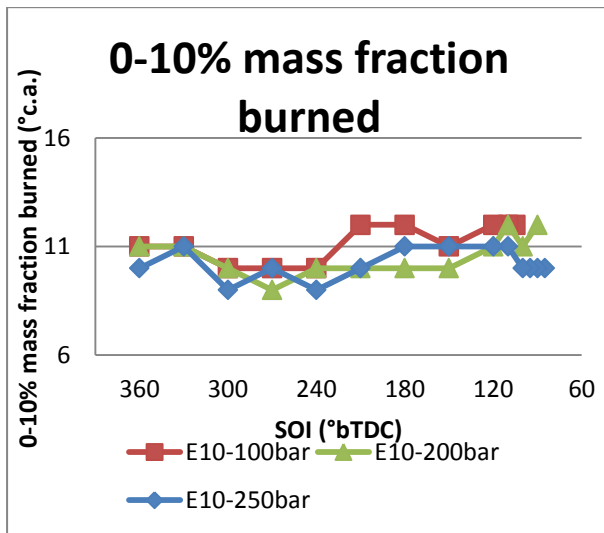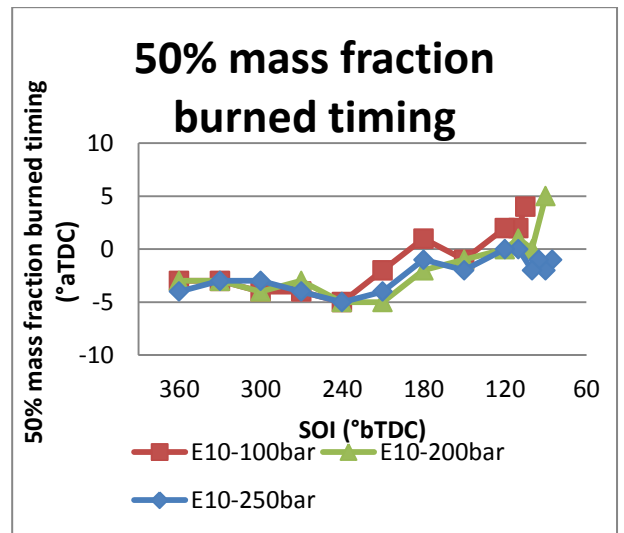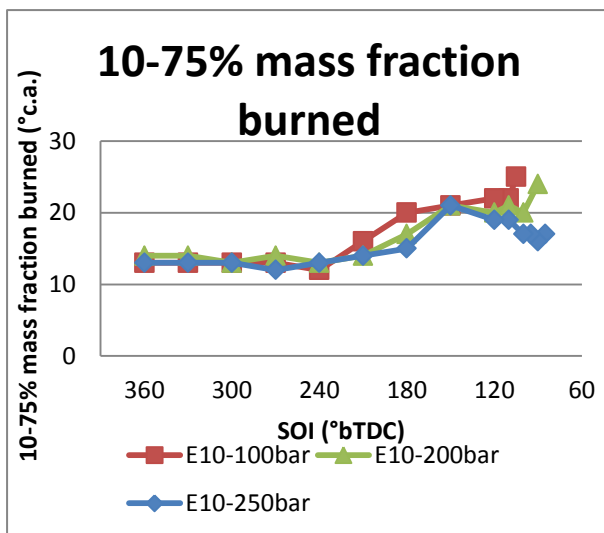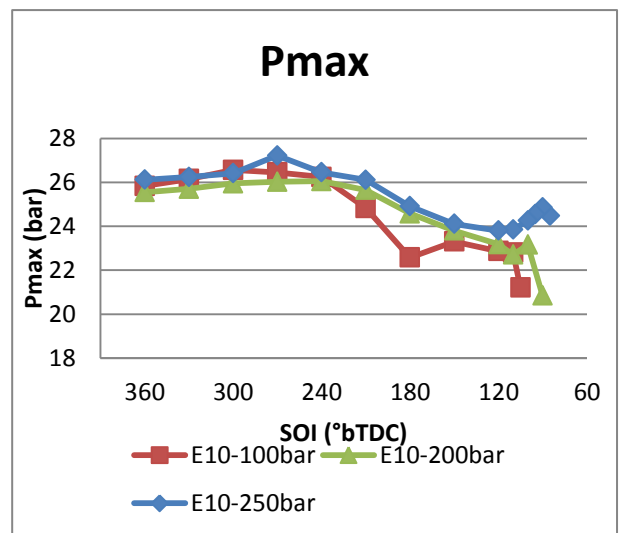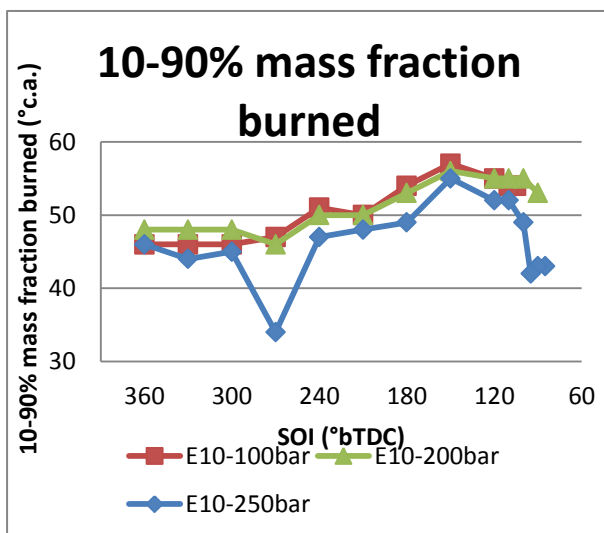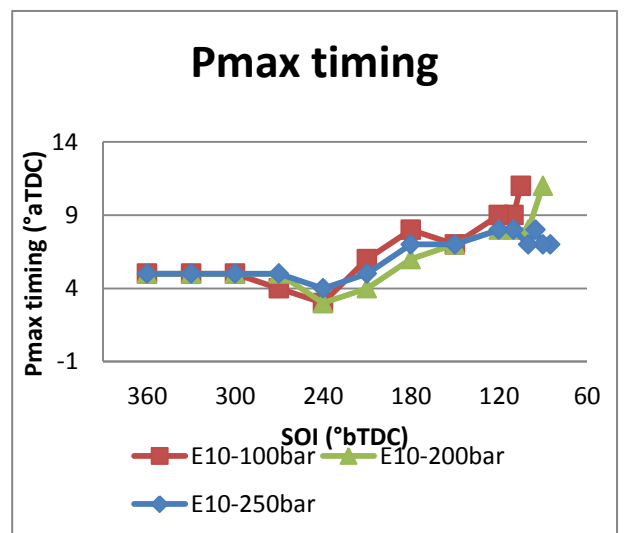
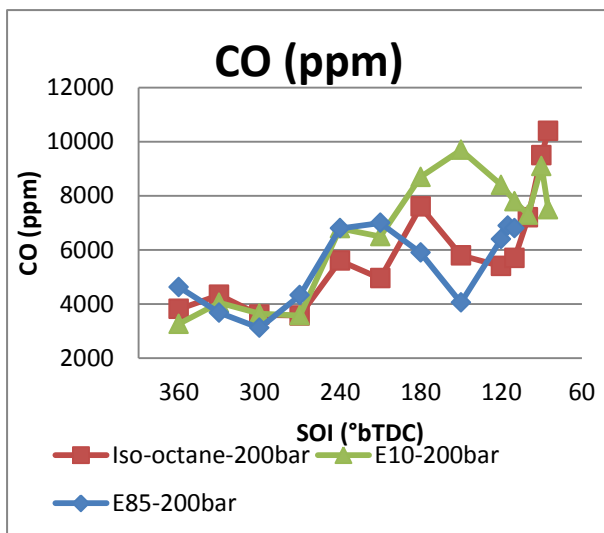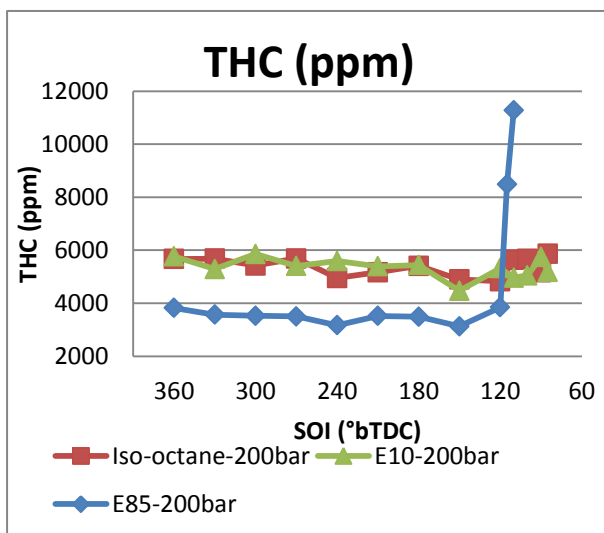Figure A 3: a) 0-10% MFB b) 10-75% MFB c) 10-90% MFB d) 50% MFB timing e) Pmax and f) Pmax timing during SOI sweeps at varied injection pressure (E10)
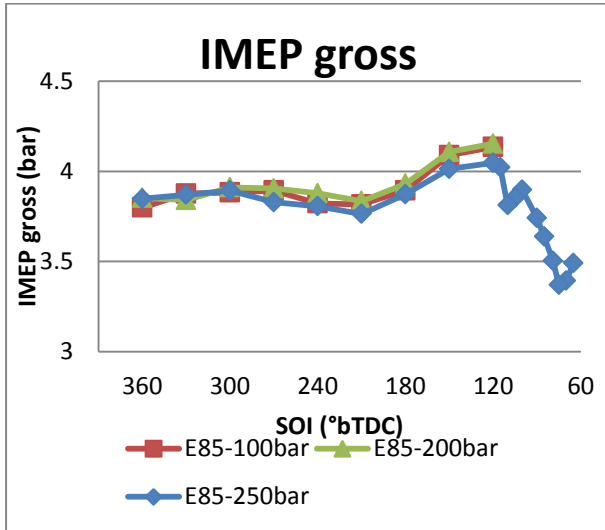
(a)
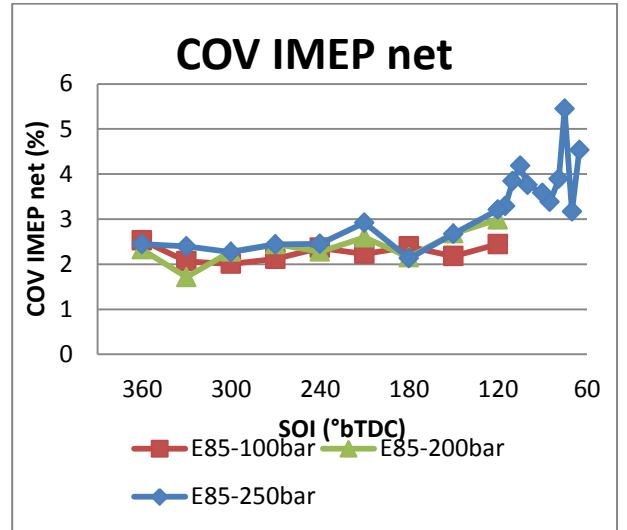
(a)
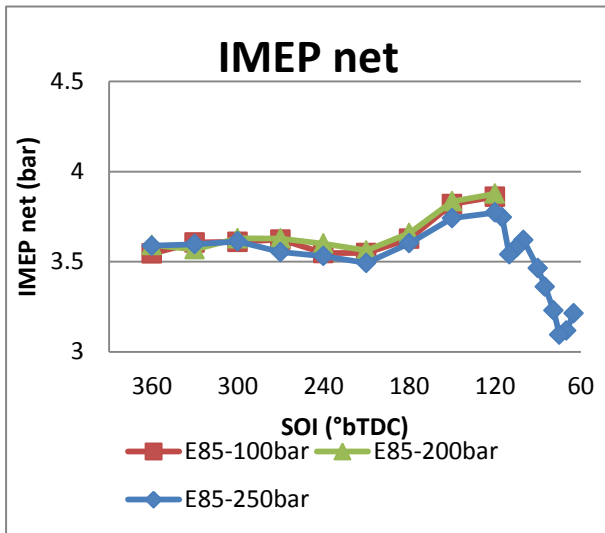
(b)
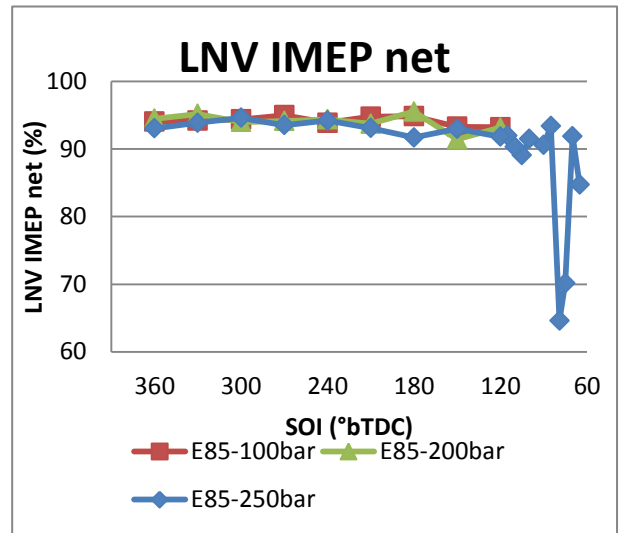
(b)

Figure B 1: a) Gross IMEP and b) Net IMEP during SOI sweeps at varied injection pressure (E85)
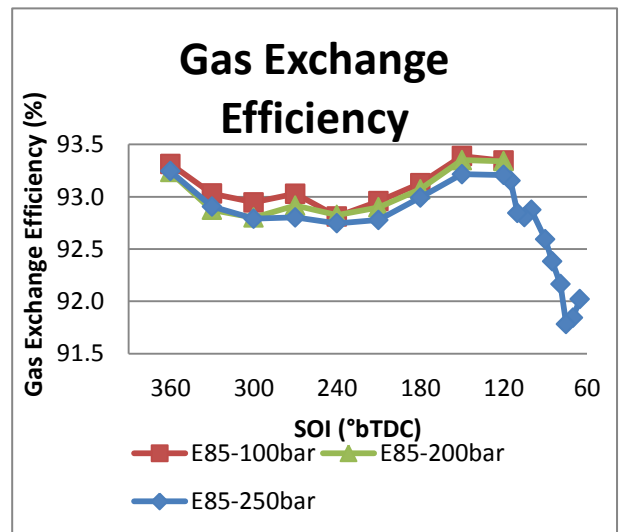
(c)

Figure B 2: Values of a) COV b) LNV and c) Computed gas exchange efficiency during SOI sweeps at varied injection pressure (E85)

127

(a)

(b)

(c)

(d)

(e)
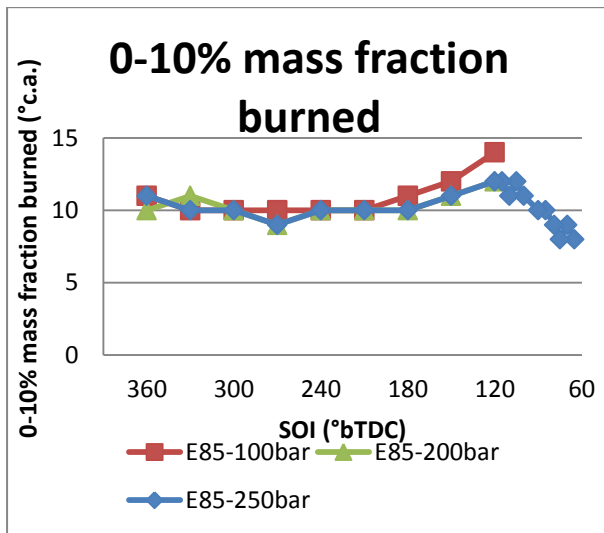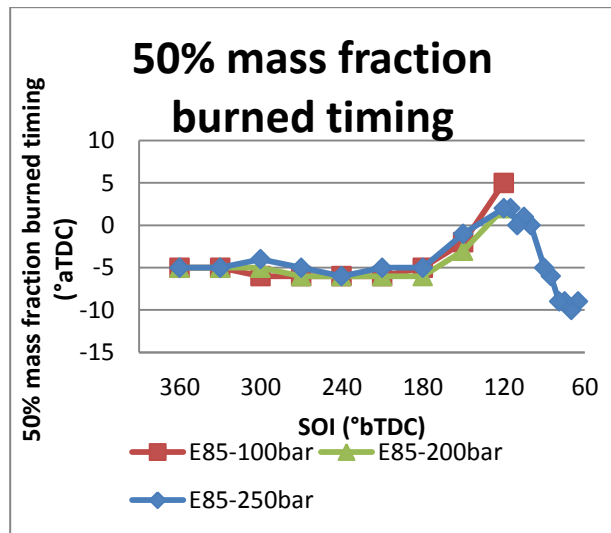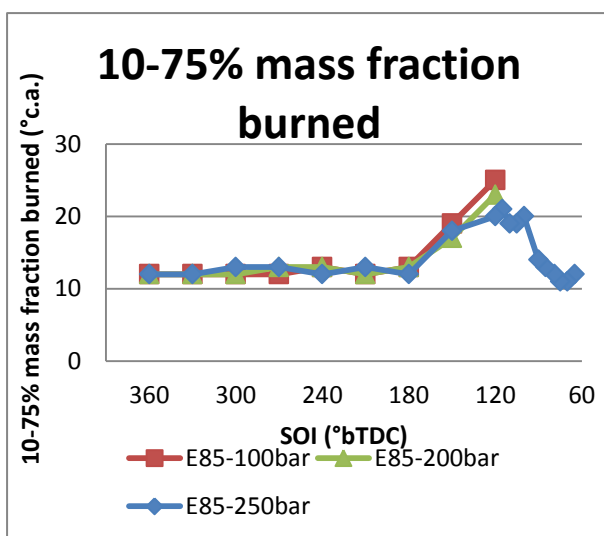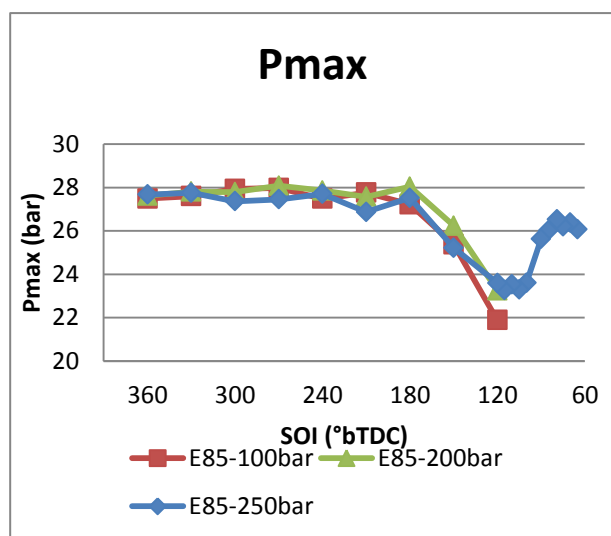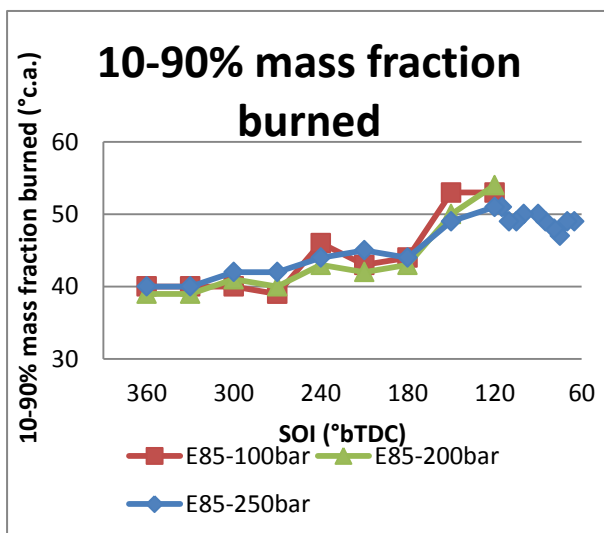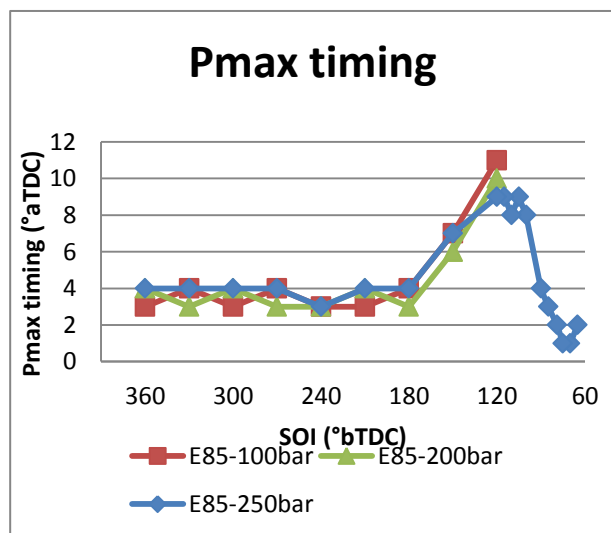
(f)

Figure B 3: a) 0-10% MFB b) 10-75% MFB c) 10-90% MFB d) 50% MFB timing e) Pmax and f) Pmax timing during SOI sweeps at varied injection pressure (E85)
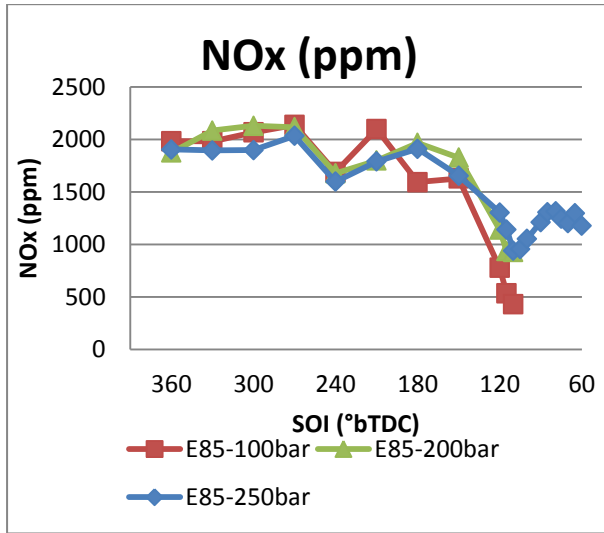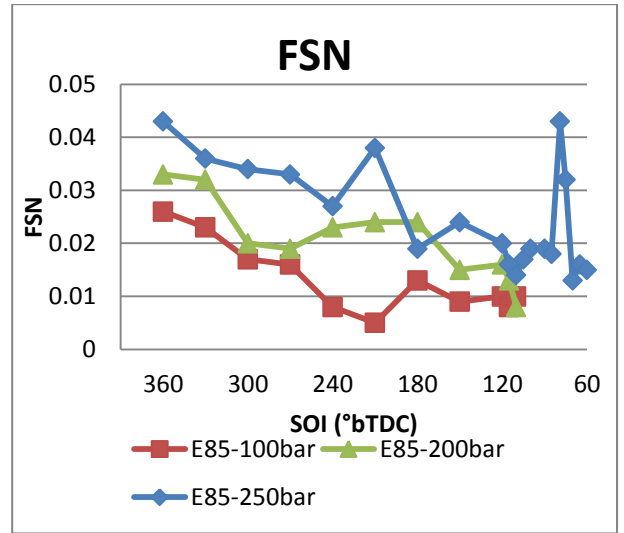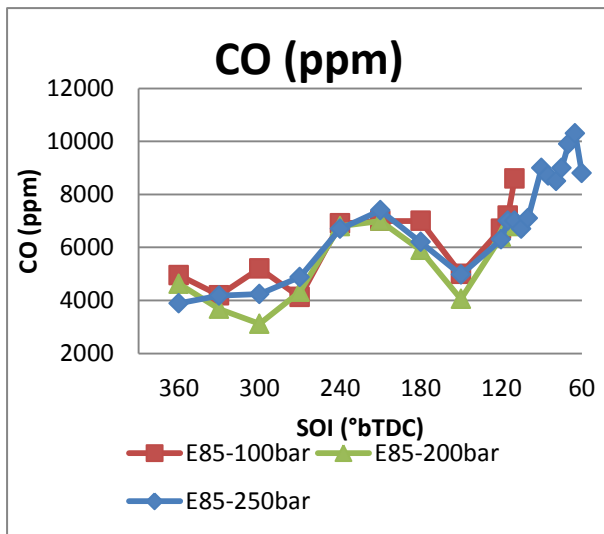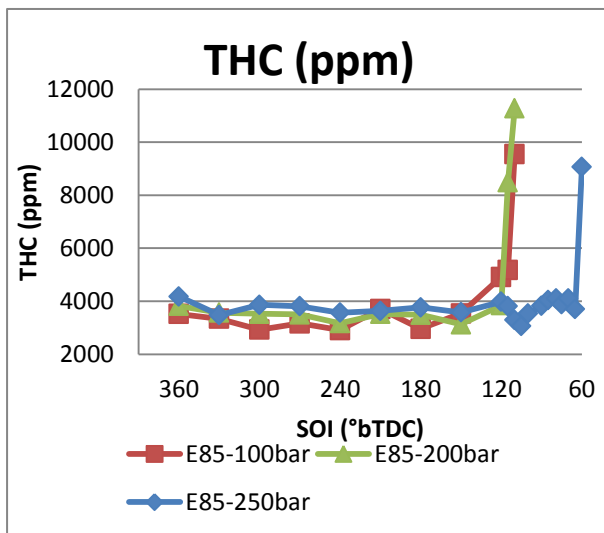
(a)

(b)

(c)

Appendix C   Fuel Blend Effects (200bar)

(a)

(a)
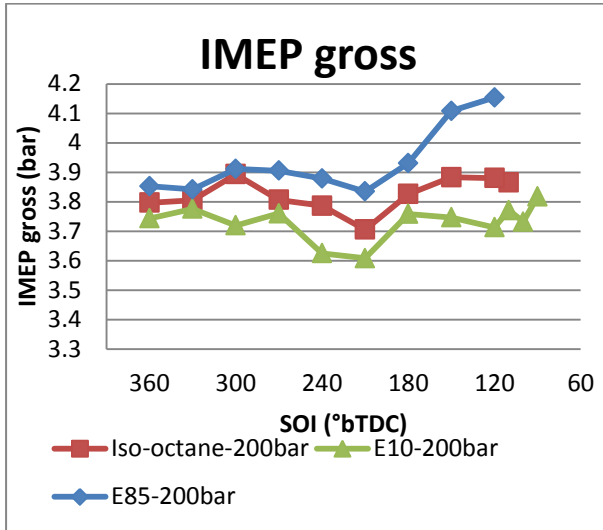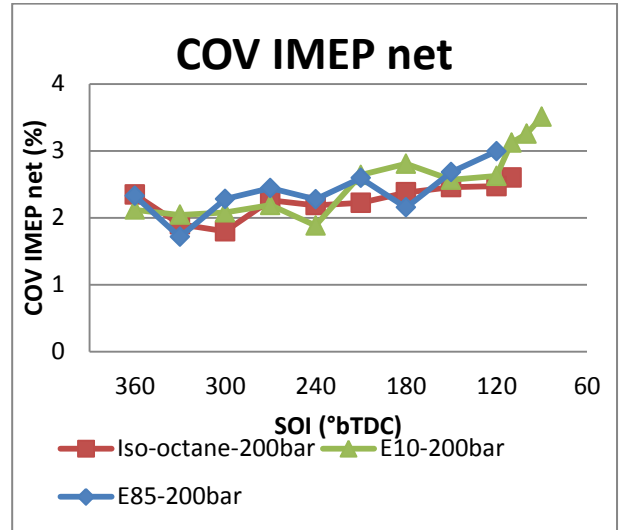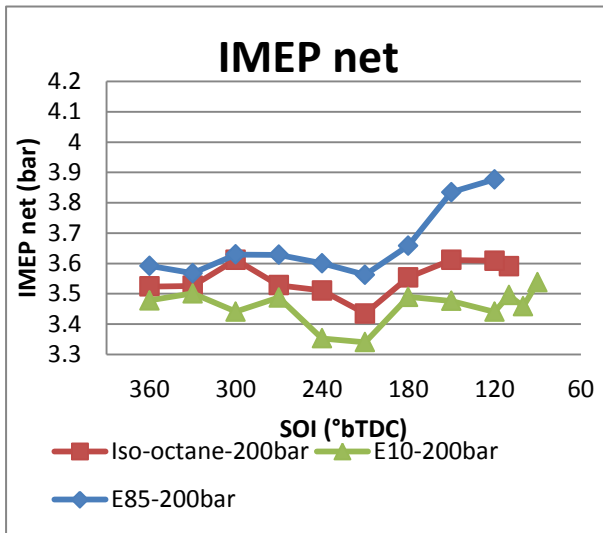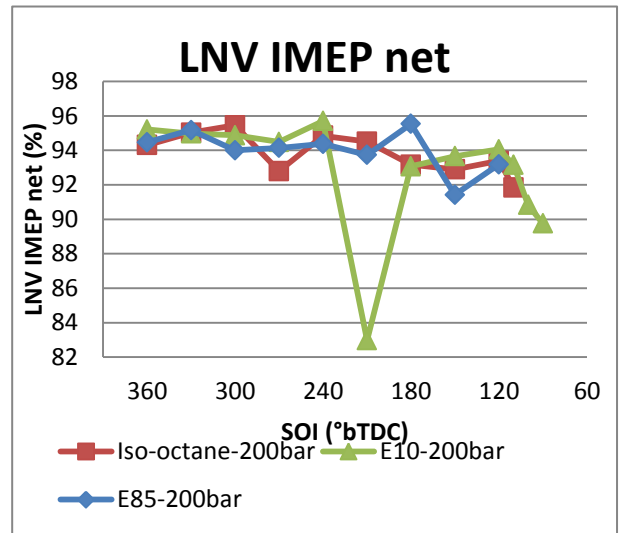
(b)

Figure C 1: a) Gross IMEP and b) Net IMEP during SOI sweeps using different fuels (200bar)


(b)
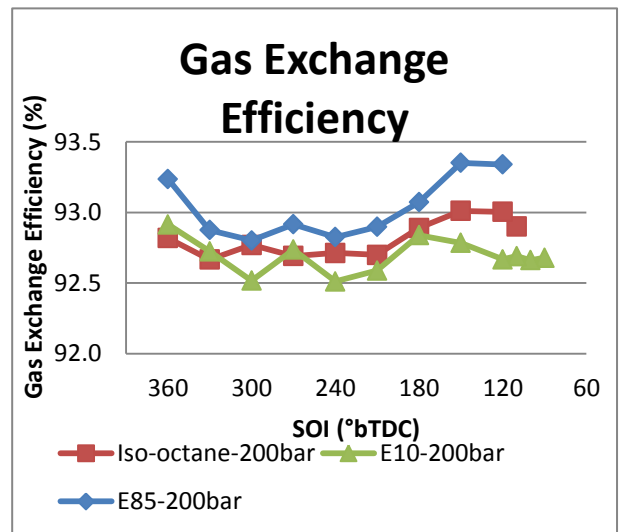
(c)

Figure C 2: Values of a) COV b) LNV and c) Computed gas exchange efficiency during SOI sweeps using different fuels (200bar)
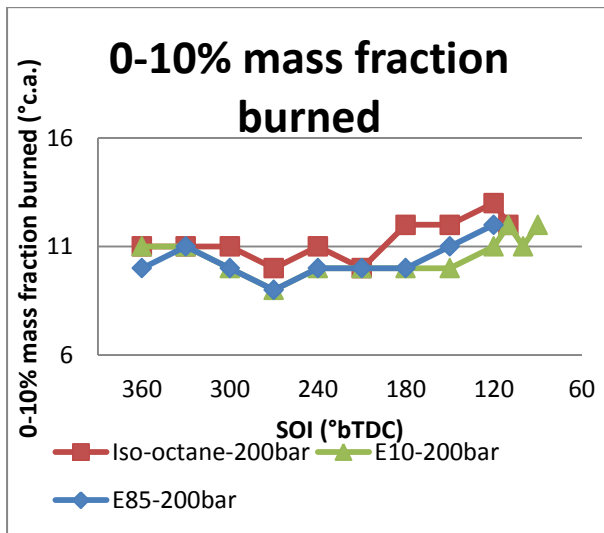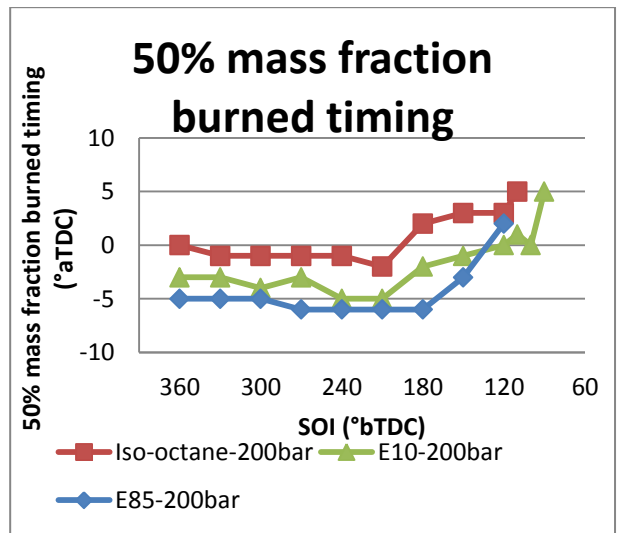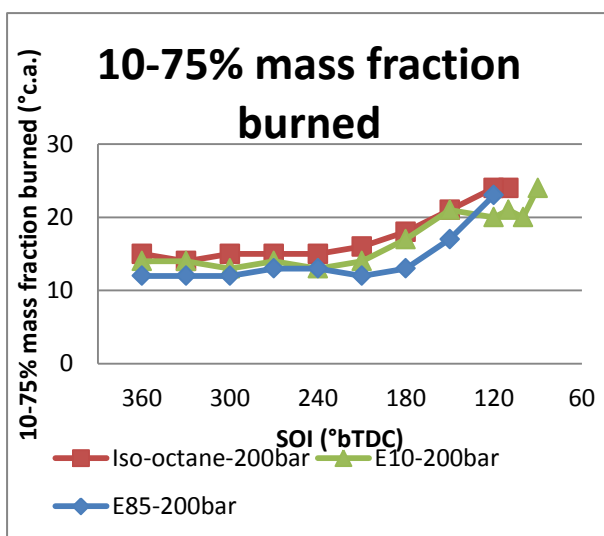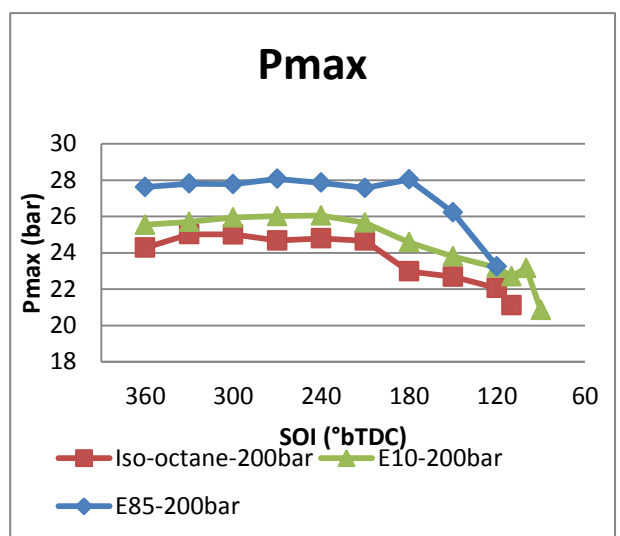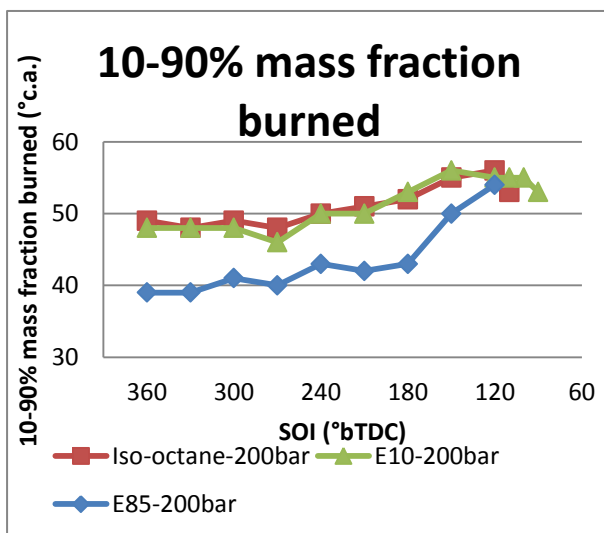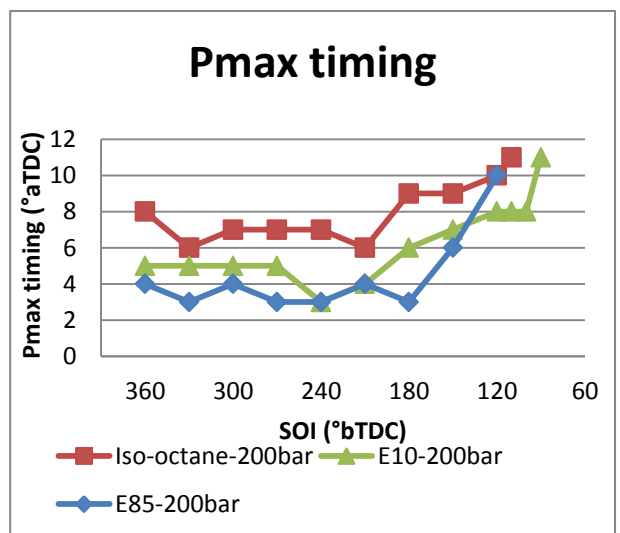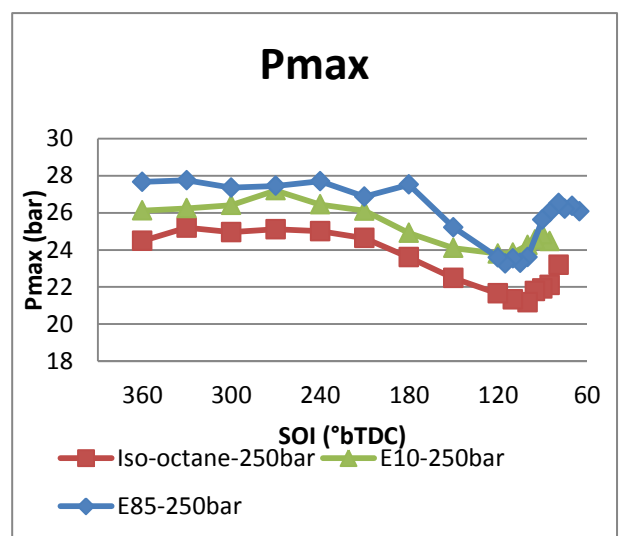
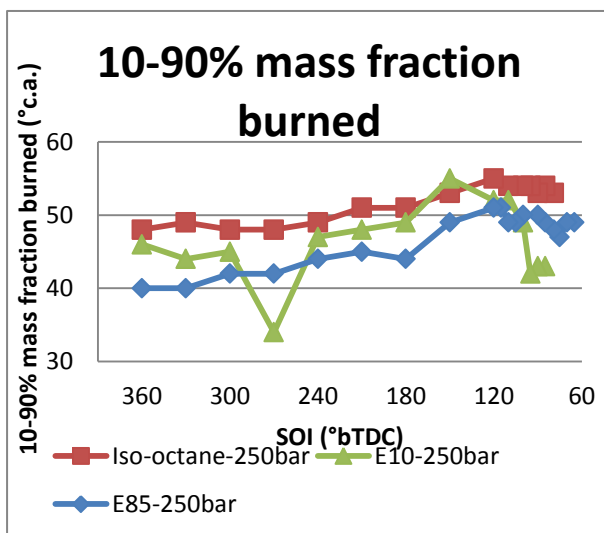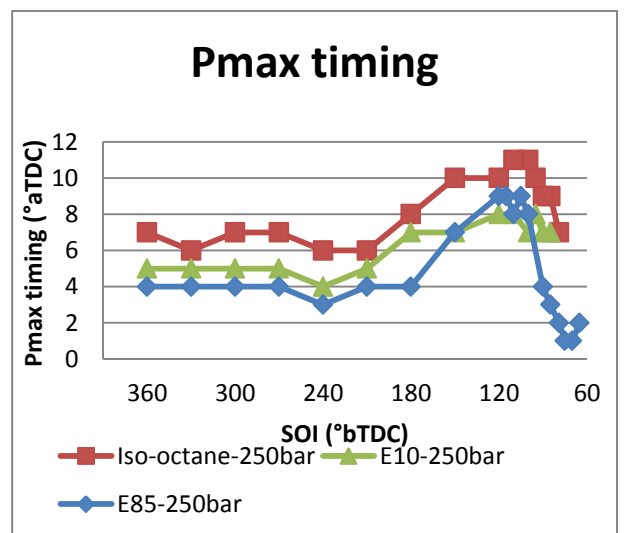**Figure C 3: a) 0-10% MFB b) 10-75% MFB c) 10-90% MFB d) 50% MFB timing e) Pmax and f) Pmax timing during SOI sweeps using different fuels (200bar)**
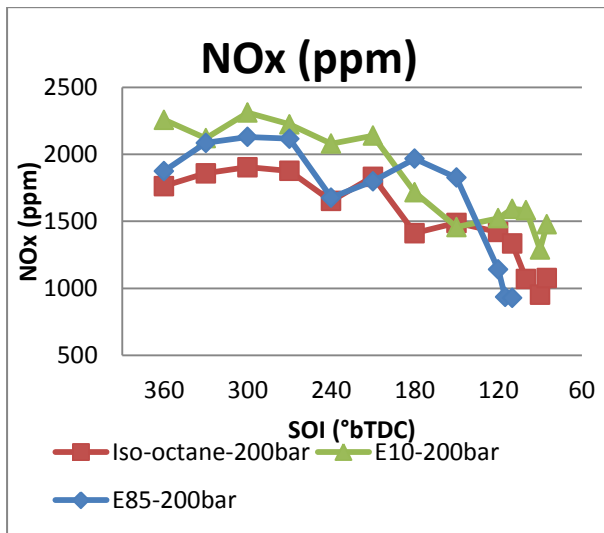
(a)
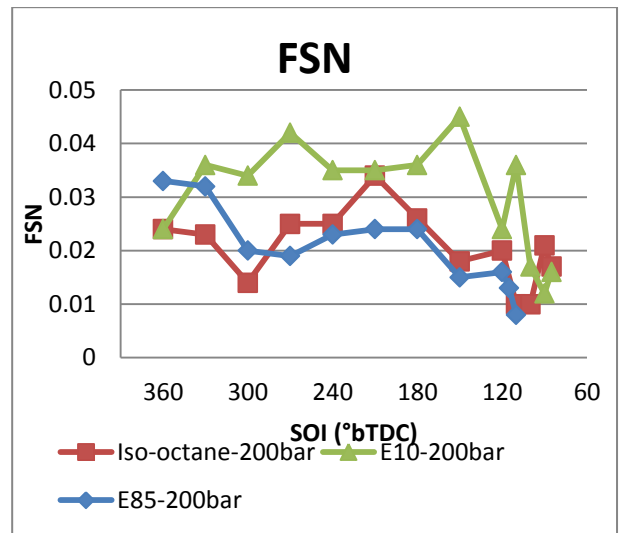
Figure C 5: Filter Smoke Number (FSN) during SOI sweeps using different fuels (200bar)

(b)

(c)

Figure C 4: Engine-out emissions a) NOx b) CO and c) THC during SOI sweeps using different fuels (200bar)

IMEP gross

(a)

COV IMEP net

(a)

IMEP net
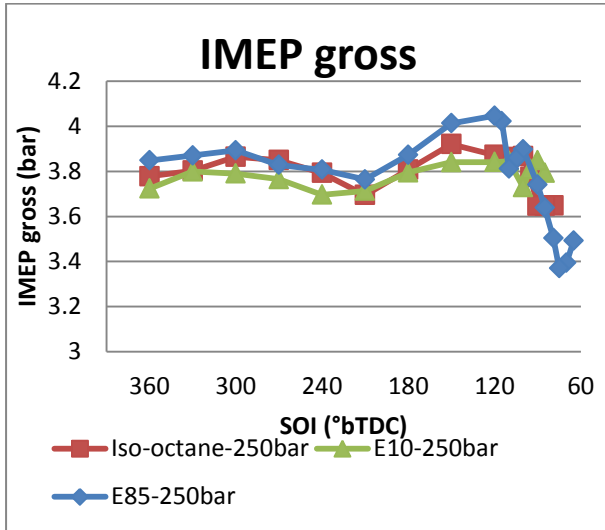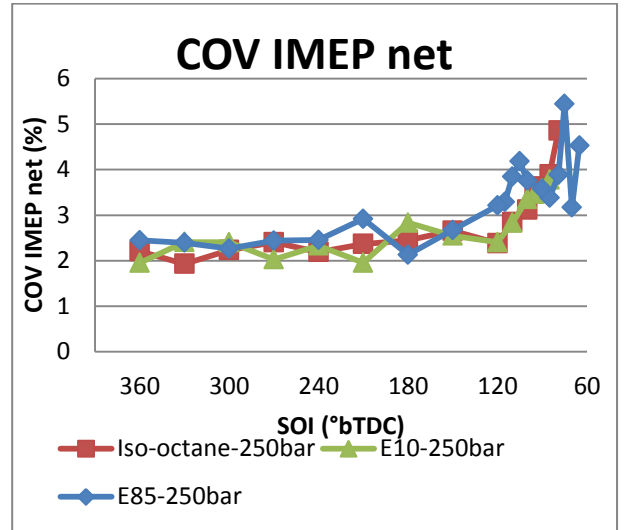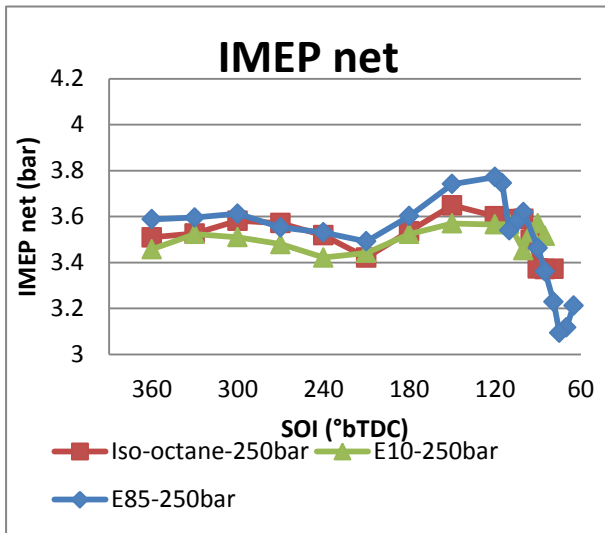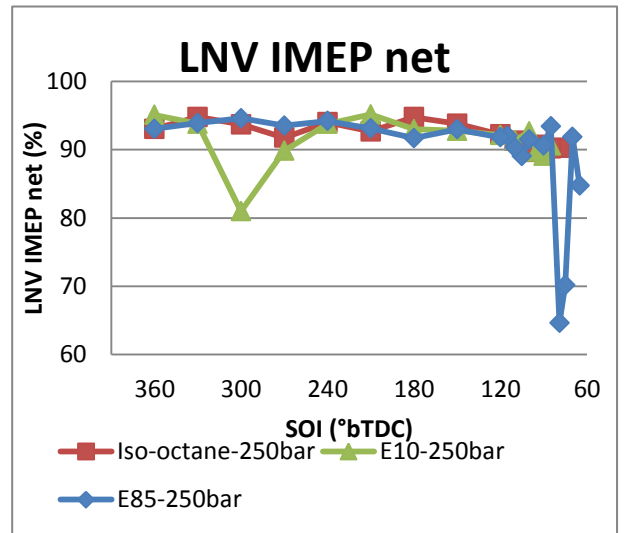
(b)

Figure D 1: a) Gross IMEP and b) Net IMEP during SOI sweeps using different fuels (250bar)

LNV IMEP net

(b)

Gas Exchange Efficiency
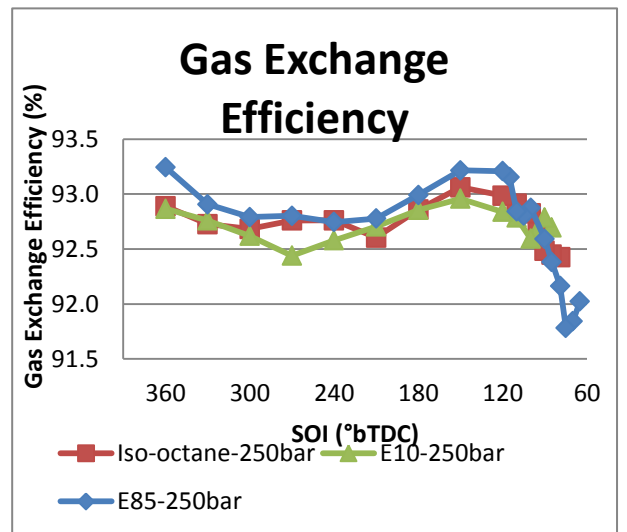
(c)

Figure D 2: Values of a) COV b) LNV and c) Computed gas exchange efficiency during SOI sweeps using different fuels (250bar)
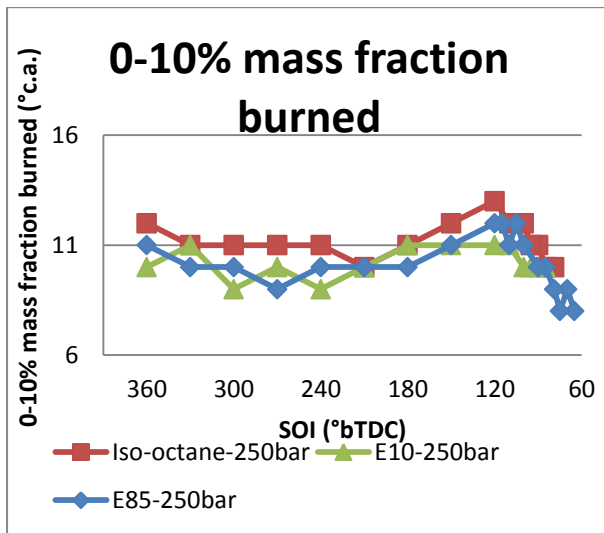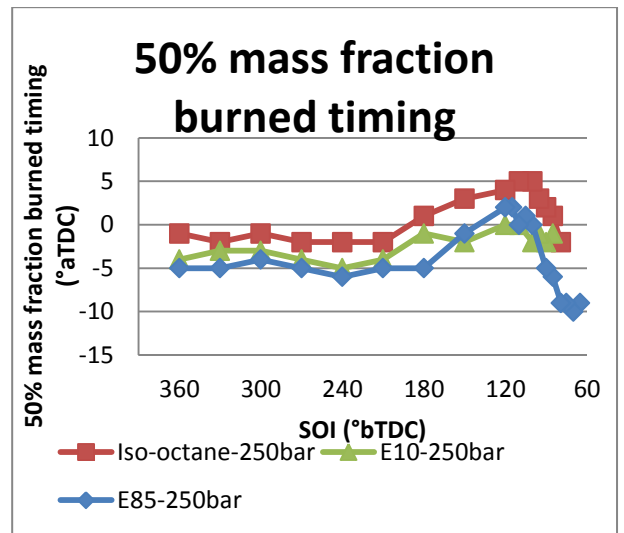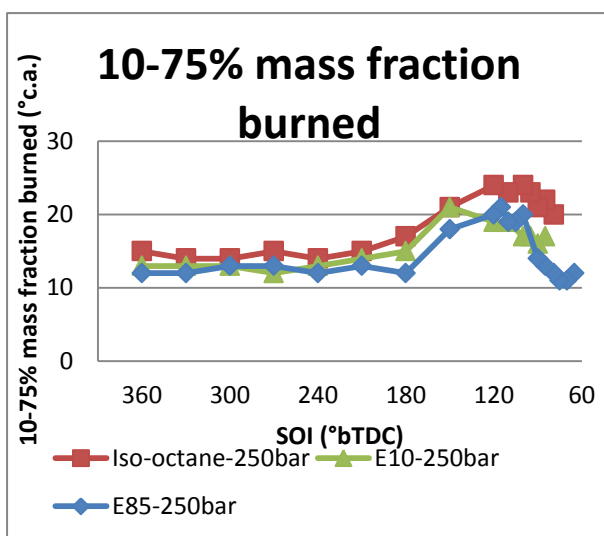
Figure D 3: a) 0-10% MFB b) 10-75% MFB c) 10-90% MFB d) 50% MFB timing e) Pmax and f) Pmax timing during SOI sweeps using different fuels (250bar)
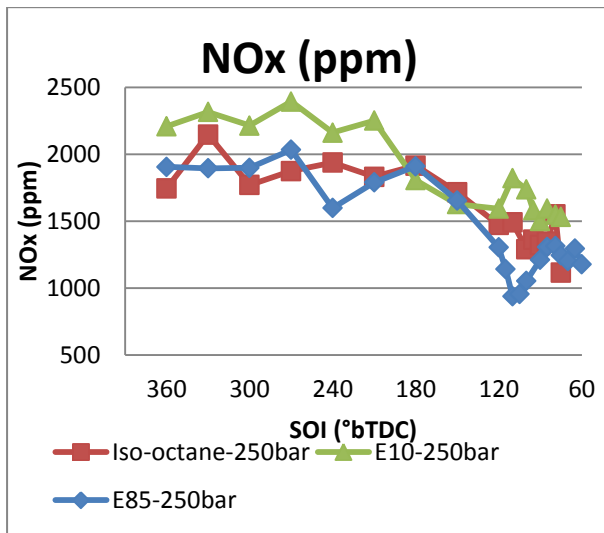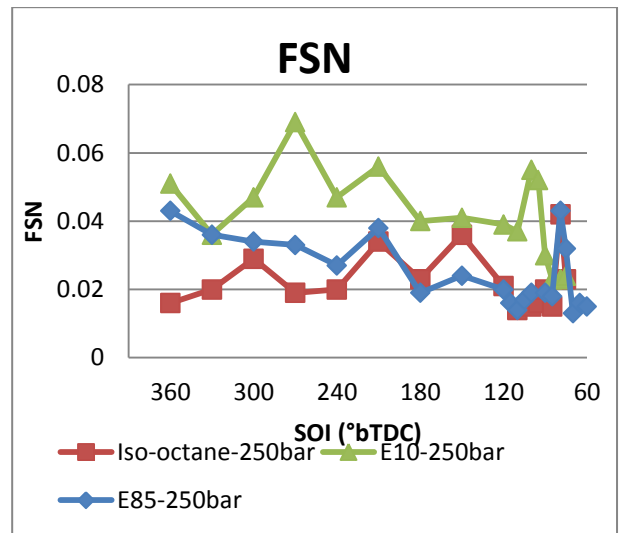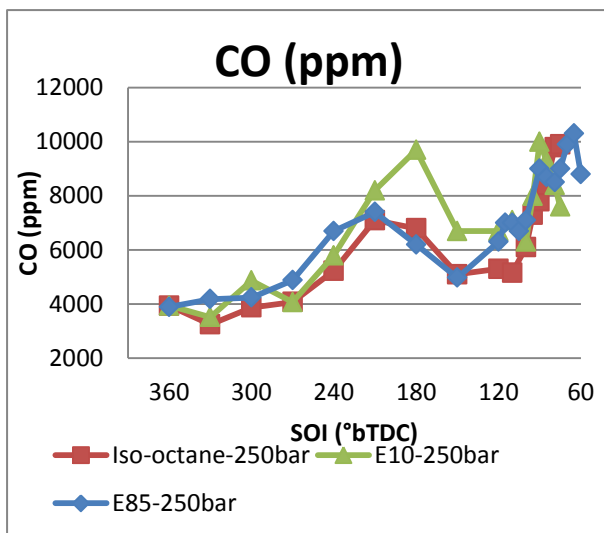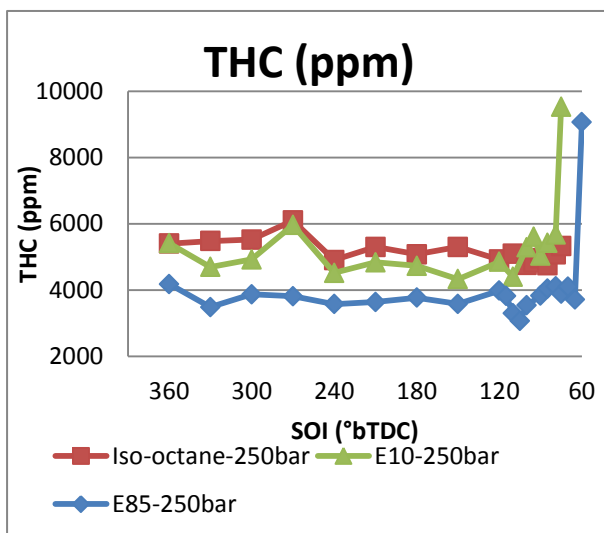
(a)

Figure D 5: Filter Smoke Number (FSN) during SOI sweeps using different fuels (250bar)

(b)

(c)

Figure D 4: Engine-out emissions a) NOx b) CO and c) THC during SOI sweeps using different fuels (250bar)